Markus Vilkki

Flyback transformer of an auxiliary power supply in photovoltaic inverters

School of Electrical Engineering

Thesis submitted for examination for the degree of Master of Science in Technology.

Espoo 24.11.2014

Thesis supervisor:

Prof. Jorma Kyyrä

Thesis advisor:

M.Sc. Simo Mattila

Aalto University
School of Electrical
Engineering

AALTO UNIVERSITY
SCHOOL OF ELECTRICAL ENGINEERING

ABSTRACT OF THE
MASTER'S THESIS

Author: Markus Vilkki

Title: Flyback transformer of an auxiliary power supply in photovoltaic inverters

Date: 24.11.2014 Language: English Number of pages: 10+97

Department of Electrical engineering and automation

Professorship: Power electronics Code: S-81

Supervisor: Prof. Jorma Kyyrä

Advisor: M.Sc. Simo Mattila

The aim of this thesis was to design flyback transformers for two flyback converters, which are part of an auxiliary power supply of a photovoltaic inverter. In the designs, cost efficiency and reliable operation were emphasized and the operation of the designed components was to be verified in a laboratory environment.

The cost efficiency in the designs was sought by using triple insulated wire only in the windings requiring reinforced insulation. In addition, Chinese suppliers were selected as the manufacturers of the chosen magnetic ferrite cores.

Six different prototypes were designed according to the initial preferences and by calculating parameters and selecting properties. The costs of the different designs were found to be dependent on the size of the component as the largest components were the most expensive. In addition, triple insulated wire of multiple strands was found to be the most expensive material.

The designed properties were found to correspond well with the measured values. In addition, the designed flyback transformers operated without any faults in the intended flyback converter applications. However, based on the measured switching frequencies of one flyback converter, the value of the designed mutual inductance should be somewhat decreased in order to be verified of the reliable operation.

The measured resistances of the windings showed that using multiple individually insulated strands in the wires reduces the increase of the alternating current resistance and therefore the amount of copper losses. Furthermore, this was also verified as the lower thermal rises of the components were multiple strands were used, if compared to the equivalent components using single conductors in the windings.

Based on the satisfying operation during the measurements, two designs were selected for additional testing in the actual photovoltaic inverter application.

Keywords: flyback transformer, design,
power supply, winding

AALTO-YLIOPISTO
SÄHKÖTEKNIIKAN KORKEAKOULU

DIPLOMITYÖN
TIIVISTELMÄ

Tekijä: Markus Vilkki

Työn nimi: Aurinkosähkövaihtosuuntaajan apujänniteteholähteen flyback-muuntaja

Päivämäärä: 24.11.2014 Kieli: Englanti Sivumäärä: 10+97

Sähkötekniikan laitos

Professuuri: Tehoelektroniikka Koodi: S-81

Valvoja: Prof. Jorma Kyyrä

Ohjaaja: M.Sc. Simo Mattila

Tämän työn tavoitteena oli suunnitella flyback-muuntajat kahdelle flyback-teholähteelle, jotka ovat osa aurinkosähkövaihtosuuntaajan apujännitetelähdettä. Suunnittelussa tuli erityisesti kiinnittää huomiota komponenttien kustannustehokkuuteen sekä toiminnan luotettavuuteen. Suunniteltavien komponenttien toiminnasta tuli myös varmistua laboratoriomittauksin.

Kustannustehokkuutta etsittiin mitoituksissa käyttämällä kolmoiseristettyä johdinta ainoastaan käämeissä, jotka vaativat turvaerotuksen muista piireistä sekä valitsemalla magneettisten ferriittisydänten valmistajiksi kiinalaisia vaihtoehtoja. Alkuarvojen, laskettujen parametrien sekä valittujen ominaisuuksien perusteella suunniteltiin kuusi erilaista mitoitusta. Suunniteltujen komponenttien koon havaittiin vaikuttavan kustannuksiin siten, että suurimmat komponentit olivat arvokkaimpia. Lisäksi, monisäikeinen kolmoiseristetty käämilanka osoittautui arvokkaimmaksi yksittäiseksi materiaaliksi komponenteissa.

Komponenttien suunniteltujen ominaisuuksien havaittiin vastaavan hyvin mitattuja arvoja. Suunnitellut komponentit myös toimivat vikaantumatta osana flyback-teholähteitä. Toisen flyback-teholähteen mitattujen kytkentätaajuuksien perusteella kuitenkin havaittiin, että mitoitusten keskinäisinduktanssin tulisi olla jonkinverran pienempi, jotta toiminnan luotettavuudesta pystyttäisiin varmistumaan käytännössä.

Mitatuista käämiresistansseista havaittiin useasta säikeestä koostuvan käämilangan pienentävän vaihtovirtaresistanssin kasvua sekä siten myös käämitysten kuparihäviöiden suuruutta. Tästä varmistuttiin mittaamalla alhaisempia lämpenemiä komponenteista, joissa käytettiin useasta säikeestä koostuvaa käämilankaa verrattuna vastaaviin yksittäisellä johtimella toteutettuihin komponentteihin.

Työn tulosten perusteella kaksi mitoitusta valittiin aurinkosähkövaihtosuuntaajassa tapahtuviin mahdollisiin jatkomittauksiin.

Avainsanat: flyback-muuntaja, mitoitus, teholähde, käämi

Preface

I want to thank my advisor, Simo Mattila, for the professional guidance during the thesis process. In addition, I would like to thank Professor Jorma Kyyrä for the supervision and the comments.

Special thanks to Joonas Puukko for initiating this process and making it possible. Furthermore, I am thankful for the advices I received from Lari Nousiainen and Jukka Päri regarding the thesis.

Finally, I want to thank my parents, Emma and other friends who have supported and motivated me during the past eight months and also during my studies in Aalto.

Otaniemi, 24.11.2014

Markus Vilkki

Contents

Definitions and abbreviations

Definitions

α_i	fraction of window allocated to the winding
ω	angular frequency, $2\pi f$
ρ_c	resistivity of copper
ρ_{Fe}	density of core losses
θ	phase angle of impedance in degrees
ΔB	peak to peak flux density
Δi_L	change in inductor current
μ	characteristic permeability of material
μ_i	initial permeability of material
μ_0	permeability of vacuum
μ_a	amplitude permeability of material
μ_r	relative permeability of material
Φ	flux
$\Re$	reluctance
$\Re_c$	reluctance of a core
$\Re_g$	reluctance of an air gap
A	total surface area of a component
A_c	cross-sectional area of a core
A_{wi}	copper area of the winding wire
B	flux density
B_r	remanence flux density
B_{sat}	saturation flux density
C	capacitance
c_{DS}	drain-source capacitance
D	duty ratio
d_c	diameter of coil former
d_{cp}	diameter of center pole
D_{max}	maximum duty cycle of the MOSFET
D_{res}	duty cycle of the resonance
d_{wi}	diameter of a conductor
$d_{wi,p}$	diameter of a strand
E	energy
E_{max}	maximum energy throughput of a core
F	fringing flux factor
f	frequency
f_{grid}	grid frequency
f_{sw}	switching frequency
$f_{sw,max}$	maximum switching frequency
$f_{sw,min}$	minimum switching frequency
f_{res}	resonance frequency
F_R	AC-to-DC resistance ratio
G	window width of a magnetic core

H	strength of a magnetic field
H_{sat}	strength of a magnetic field causing saturation in a core
$H_{g,sat}$	strength of magnetic field causing saturation in gapped cores
i_C	capacitor current
i	current
i_D	drain current
i_d	diode current
I_{DC}	DC value of current
i_L	inductor current
I_L	DC value of inductor current
I_O	DC value of output current
$i_{i,rms}$	rms value of a current in a winding
i_M	magnetizing current
i_P	current in primary winding
i_{ipk}	peak value of a current in a winding
i_{Ppk}	peak value of a current in a primary winding
i_r	current through range resistor
i_{rating}	maximum rated current of a MOSFET
i_S	current in a secondary winding
i_{Spk}	peak value of a current in a secondary winding
i_{tot}	sum of rms values of winding currents
i_x	current flowing through DUT
J	current density
L	inductance
l_c	mean length of a magnetic path in a core
l_e	mean length of a magnetic path
l_g	length of an air gap
L_l	leakage inductance
L_M	magnetizing inductance
L_{lP}	leakage inductance of a primary
L_{lS}	leakage inductance of a secondary
MLT	mean length per turn of all windings
MLT_i	mean length per turn of a winding
N	number of turns
N_{AUX}	turns ratio from primary to auxiliary winding
N_i	number of turns in a winding
N_P	number of turns in a primary winding
N_{PS}	turns ratio from primary to secondary
N_S	number of turns in a secondary winding
t	time interval
p_i	number of parallel strands
P_{Cu}	copper loss
P_{Cu0}	ohmic copper loss

$P_{Cu,ac}$	AC copper loss
P_{loss}	total losses of a component
P_V	power loss density
R_{0i}	ohmic resistance of a winding
$R_{DS,on}$	resistance of a MOSFET during on time
R_r	range resistor of the precision impedance analyzer
T_C	Curie temperature
t_{off}	off time of a MOSFET
t_{on}	on time of a MOSFET
t_{res}	resonance time in discontinuous mode
t_{rr}	reverse recovery time
T_{Cu}	temperature of windings
T_{Fe}	temperature of a core
T_S	switching period
v	voltage
V_{AUX}	voltage over an auxiliary winding
$V_{AC,rms}$	rms value of AC voltage
v_{CC}	operating voltage of control circuit
v_d	diode voltage
V_D	DC value of source voltage
v_{drop}	voltage drop due to the $R_{DS,on}$ and a resistance of a primary
v_{DS}	drain-source voltage
V_e	effective volume of a core
v_F	forward voltage drop of freewheeling diode
v_{FCC}	forward voltage drop of diode in auxiliary winding
v_{GS}	gate-source voltage
$v_{in,max}$	maximum input voltage
$v_{in,min}$	minimum value of input voltage
v_L	voltage over inductance
v_O	output voltage
V_O	DC value of output voltage
v_P	voltage over primary winding
v_r	reflected voltage
v_R	voltage over a range resistor
v_{rating}	maximum rated voltage stress of a MOSFET
V_{ref}	reference voltage
v_S	voltage over secondary winding
v_{spike}	voltage spike due to leakage inductance
v_x	voltage over DUT
W	width of a core
W_A	window area of a magnetic core
Z	height of a core
Z_x	impedance of a DUT
X	depth of a core
Y	thickness of a core

Abbreviations

AC	alternating current
BCM	boundary conduction mode
BDEW	Bundesverband der Energie- und Wasserwirtschaft, German association of energy and water industries
BJT	bipolar junction transistor
CCM	continuous conduction mode
DC	direct current
DCM	discontinuous conduction mode
DUT	device under test
DVC	decisive voltage class
EMI	electromagnetic interference
ETD	economical transformer design
FFM	frequency foldback mode
IEC	International Electrotechnical Commission
IGBT	insulated gate bipolar transistor
IO	input output
Mn-Zn	manganese-zinc
MOSFET	metal oxide semiconductor field effect transistor
MPP	maximum power point
n	negatively doped region
n^-	lightly doped negative region
p	positively doped region
PCB	printed circuit board
PCE	power conversion equipment
PV	photovoltaic
QR	quasi-resonant
rms	root-mean-square
TIW	triple insulated wire

1 Introduction

As photovoltaics is establishing position as a significant form of renewable energy generation, the pressure to improve the cost efficiency of PV (photovoltaic) inverters is growing. Nonetheless, cutting costs in wrong places, in order to improve cost efficiency, usually decreases the reliability of the products. Therefore, the designer has to ensure that the costs of components will not be cut such that the reliable operation of the products is harmed.

The auxiliary power supply of PV inverter provides power for several tasks in the inverter. Since the power electronic devices, used in switched-mode, became common, the auxiliary power supplies have been made using switched-mode converters. The advantages of switched-mode power supplies over the linear power supplies is higher efficiency and smaller size.

Flyback converter is a widely used converter topology in the auxiliary power supplies. The advantages of the topology are the small amount of involved components and that the flyback transformer provides both energy storage and galvanic separation between the input and output of the converter. For these reasons, flyback converter is an economical solution for power supplies requiring low power [1].

The flyback transformer is typically the most expensive component of the converter circuit. Because the component has significant impact on the operation and efficiency of the converter, the design of the flyback transformer is worth an effort.

The aim of this thesis is to design flyback transformers for two flyback converters, which are used in the auxiliary power supply of a three phase photovoltaic inverter. The focus of the designs will be cost efficiency and reliable operation in all operating points. The cost efficiency in the designed flyback transformers will be sought by using TIW (triple insulated wire) only in the windings requiring reinforced insulation to provide protective separation from other windings. In addition, Chinese suppliers will be chosen as the manufacturers of the ferrite cores used in the components. Finally, mutual and leakage inductances, resistances of windings and saturation behaviour of the components will be measured and the operation of the designs, along with thermal rise, will be verified.

In the second chapter of the thesis, the application of the auxiliary power supply is described. In addition, the chapter presents the theory of switched-mode power supplies and flyback transformer. The flyback transformers are designed in the third chapter according to the initial preferences of the converters and based on the theory presented in the second chapter. In the fourth chapter, the operation of the designs is verified in the measurements conducted in a laboratory environment. Finally, the fifth chapter summarizes the most important points of the thesis and conclusions are made based on the results.

2 Auxiliary power supply of a photovoltaic inverter

In this chapter, the theory of auxiliary power supplies of a three phase photovoltaic inverter application is presented. In the beginning, the typical functions and requirements of grid connected string inverters are introduced. Secondly, the operation of switched-mode converters is described. Furthermore, the description is focused on flyback topologies, which are widely used in auxiliary power supplies. Finally, the magnetic theory and the design of flyback transformer will be presented.

2.1 Grid connected photovoltaic inverters

Grid connected photovoltaic power plants feed the generated electric power to grid. Their input is connected to PV generators and output is connected to the public AC (alternating current) grid. The power levels of different applications may vary from less than one kW to several MW depending on the physical area of power plants. Moreover, power levels of new PV power plants are constantly groving at the moment. In this section, three phase string inverter applications are introduced. Furthermore, the main tasks, operation of auxiliary power supplies and the applicable standard for insulation requirements in photovoltaic inverters are presented.

2.1.1 Three-phase string inverter application

Power range of three-phase string inverters is at the moment from few kW to thirty kW. For example, inverter manufacturer SMA offers three-phase string inverters in a power range from five to twenty five kVA [2]. Their input voltage range is typically from few hundred to thousand volts and the range has to be chosen according to voltage of PV strings. Furthermore, multistring inverters are equipped with multiple string inputs to allow connection to multiple parallel PV strings.

Multistring inverters are usually intended to be used on top of buildings having PV generators mounted on the roof. Depending on the size of covered surface area, power of the PV power plant may require usage of several string inverters or a single central inverter. Central inverters can be used in many applications requiring high power [3, p. 20]. However, if insolation conditions will not be consistent among all PV strings, multiple PV string MPP(maximum power point) trackers or multiple inverters are used.

A configuration of a typical PV power plant consisting of four panel strings, multistring inverter and grid connection is shown in Figure 1. PV strings are connected to the inverter by double insulated DC (direct current) cables and small resistance connectors [3, p. 47]. DC cabling can be routed directly to string inputs of an inverter or otherwise through a junction box, if external DC switch or circuit breakers are used. AC cabling consists of three phase conductors in addition to the neutral and the protective earth conductors. AC cabling from inverter to grid is usually routed to AC distribution board of buildings.

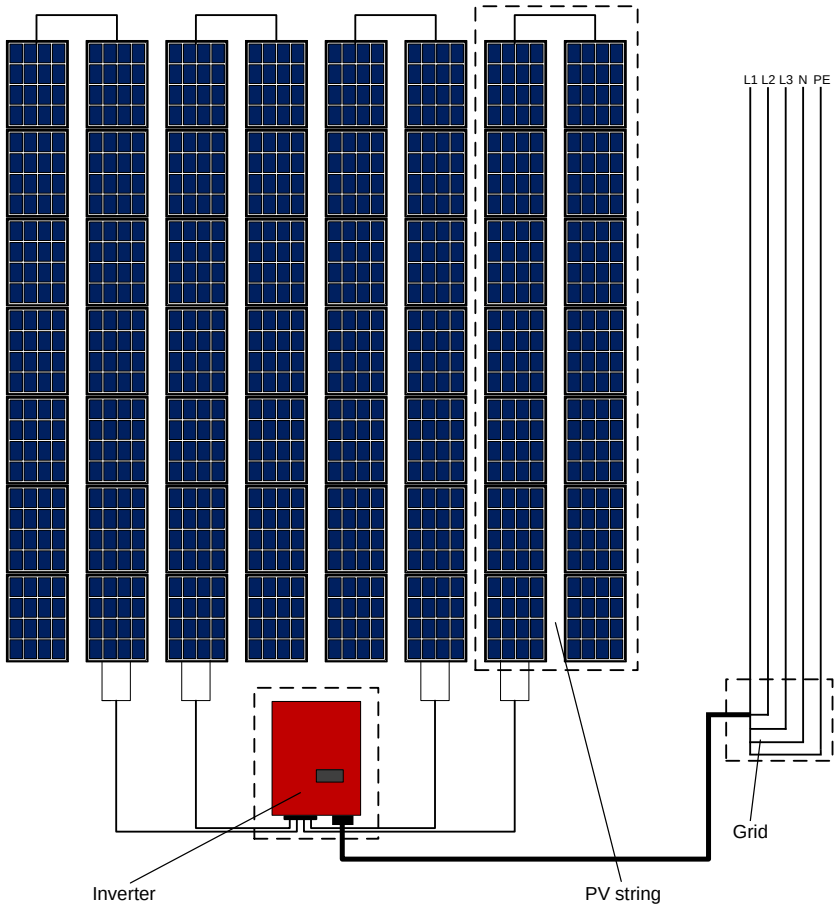

Figure 1: Typical three-phase PV power plant configuration.

2.1.2 Main functions

The main task of PV inverters is efficient power conversion from DC to grid-compatible AC. This can be realized using a power electronic inverter.

In PV inverters, the semiconductor switches are typically IGBTs (Insulated gate bipolar transistors) or MOSFETs (Metal oxide semiconductor field effect transistors) operated in the saturation region during on time. A switch turn on is realized by applying voltage to the gate of the transistor to make it conduct current from DC link of power converter circuit. Switching moments are timed such that sinusoidal three phase AC current starts flowing towards grid at grid frequency.

Because the output current of power converter contains high amount of harmonics, the current has to be filtered. Third order LCL-filter is commonly used in PV inverters to comply with the standards for injected harmonics [4, p. 31].

Inverters usually operate at efficiencies over 95 percent to maximise the yield of harvested energy. To be able to maximize the yield, inverters need to constantly track the MPP of PV generators. MPP of PV generators depend upon insolation conditions and ambient temperature of the solar panels. In addition to MPP tracking, inverters collect and store data about the power plant and energy production.

Some grid codes, such as BDEW (Bundesverband der Energie- und Wasser-

wirtschaft), determine that PV inverters are not allowed to disconnect from AC grid during grid disturbances [5]. Furthermore, they are subjected to operate at power factors also other than unity when connected to grid. In order to detect changing grid conditions, inverters monitor connection to grid constantly. Under longterm grid fault conditions inverter needs to disconnect the PV power plant from grid to maintain safety of service personnel.

2.1.3 Operation of auxiliary power supplies

Power supplies are generally used in devices to provide power for functionalities such as described in 2.1.2. Due to a number of critical functions in modern inverters, power supply has to work reliably in all insolation and weather conditions.

Power supply section of grid connected PV inverters may include only a single power supply. However, if some functionality is wanted to be maintained during long term grid fault and during night time, at least two separately powered power supplies are needed. The input of the first one will be connected to the DC link of the PV inverter and the input voltage range of the power supply will be the same as the DC link voltage range of the PV inverter.

The other one of the two power supplies is connected to AC grid through a rectifier bridge. The rectified grid voltage is filtered to get rid of unwanted ripple in input DC voltage. Desired low pass characteristics are achieved by adding a filter capacitor to the output of rectifier bridge. Figure 2 shows the typical voltage waveforms of full wave rectifier bridge circuit. The operation of the circuit is explained in detail in [6].

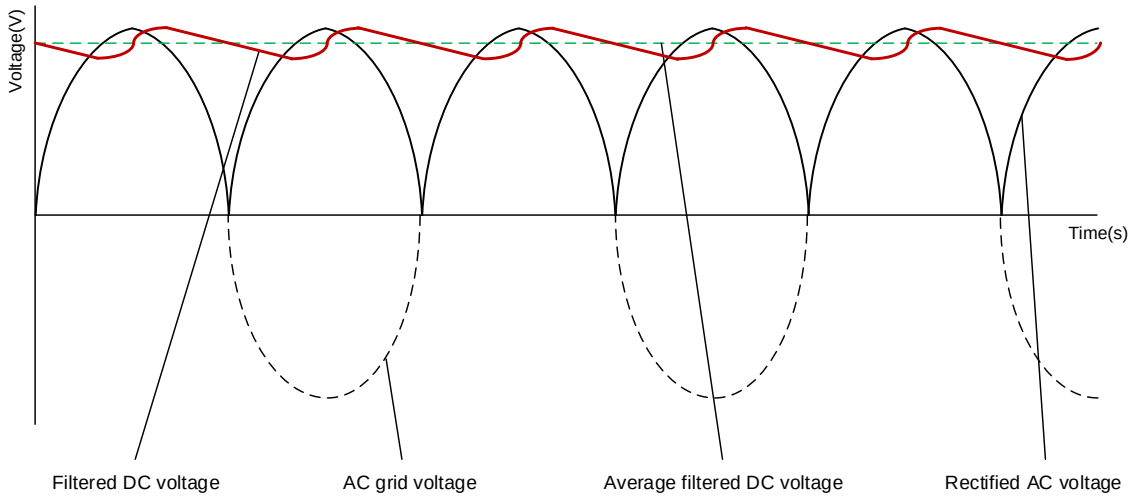

Figure 2: Voltage waveforms of full wave rectifier.

In Figure 2, the maximum value of the filtered DC voltage is calculated by

$$v_{in,max} = \sqrt{2} * V_{AC,rms} \tag{1}$$

where $V_{AC,rms}$ is the rms(root mean square) value of AC grid voltage. From Figure 2 and Equation (1) we can see that the maximum value of filtered DC voltage is equal to peak value of AC grid voltage if the forward voltage drop of diodes is neglected. In Figure 2, peak-to-peak ripple in the filtered DC voltage waveform is the voltage difference between minimum and maximum values. Size of the filter capacitor is selected to meet desired value of voltage ripple.

Typical loads requiring auxiliary power are gate power supplies, grid relays, cooling fans, user panel, IO (input output) modules and smaller converters providing power to measurement circuits and processor. Furthermore, power supplies have multiple outputs for different tasks. For safety reasons, one separate output is required for functionalities where user has access. These functionalities include for example user panel, outer fans and IO outputs.

In auxiliary power supplies of PV inverters, output voltages are lower than input voltages. Moreover, input voltages of power supplies have typically wide varying range but the output voltages are to be regulated to a certain level and are not allowed to vary. In order to regulate the output voltages efficiently, feedback controlled switched-mode converters are used [7, p. 3-5].

2.1.4 Insulation requirements

Requirements for needed insulation in PV inverters are addressed in safety standard IEC (International Electrotechnical Commission) 62109-1 [8]. In the standard, three different DVCs (decisive voltage class) are specified according to different working voltage levels. Working voltage is the highest designed voltage occuring when the PCE (power conversion equipment) is operated under worst case combination of highest and lowest rated input and output voltages and normal operating conditions. The required insulation level for each circuit is determined by DVCs from Figure A1 in Appendix A.

The different insulation levels are functional, basic and reinforced insulation. Functional insulation is the insulation needed only to guarantee normal operation of a device. In addition to functional insulation, basic insulation provides single level of protection against electric shock under fault-free conditions. Reinforced insulation is single insulation system applied to live parts providing equal level of insulation as double insulation. Furthermore, double insulation comprises both basic insulation and a supplementary insulation, that provides an additional level of insulation againts electric shock if basic insulation should fail. However, double and supplementary insulations describe how an insulation level is established and they are not considered as insulation levels.

In PV inverters, unaccessible circuits require only functional insulation. However, accessible live parts require protective separation or equivalent insulation. Protective separation can be realized for example with reinforced insulation.

The required level of insulation can be realized by using solid insulation or by clearance and creepage distances. Clearance distance means the shortest distance between two conductive parts. Similarly, creepage distance means the shortest distance along the surface of insulating material between two conductive parts. More-

over in order to determine creepage distances, the pollution degree of the designed insulator has to be known.

The tables for designing clearance and creepage distances are shown in Figures A3 and A4 in Appendix A. In Figure A4, the rms value of the working voltage is used to determine applicable creepage distances.

When realizing clearances or solid insulation, the impulse withstand voltage and the temporary overvoltage for grid connected circuits have to be found out from the table in Figure A2 in Appendix A. The impulse withstand voltage ratings are determined according to applicable system voltages. System voltage for grid connected circuits is the rms voltage between phase and artificial neutral point. Furthermore, the system voltage for PV circuits is the maximum rated PV open circuit voltage and they belong in general to overvoltage category ll.

Clearances and solid insulation for circuits connected to grid are designed according to impulse withstand voltage, temporary overvoltage or working voltage, whichever gives the most severe requirements. For PV circuits, clearances and solid insulation are determined by working voltage or impulse withstand voltage, whichever gives the most severe requirements.

The typical three phase string inverter application and the main tasks of PV inverters were described in this chapter. In addition, the basic operation of auxiliary power supplies and requirements for insulations in PV inverters were presented. In the following chapter, the main components and the operation of switched mode converters is analyzed.

2.2 Switched-mode power supplies

Power electronics is widely used in power supplies due to the high efficiency that can theoretically be close to 100 percent. High efficiency in power electronic converters is achieved by using ideally lossless components such as power semiconductor devices in switched mode and inductors and capacitors. Further, high efficiency is desirable if the size of the power supply is wanted to be kept small. This is because smaller components usually have less cooling surface area compared to a larger component and the temperature of the smaller mass rises faster. Due to the small amount of involved losses, low temperature rise of a component leads to high power density and small overall size. Furthermore, smaller size means smaller manufacturing costs due to lesser need of materials compared to a bulkier component having lower efficiency.

In this section, the operation of common power electronic converters and semiconductor switches is described. In addition, the steady state voltage transfer functions are derived for a buck-boost converter topology, which is followed by studying the operation of two flyback converter topologies and their control in quasi-resonant mode.

2.2.1 Semiconductor switches

The most widely used semiconductors in switched mode power supplies are silicon made fast-recovery diodes and MOSFETs [6, p. 8]. MOSFETs operated in the

saturation region have usually been the most suitable choice for high frequency applications rated for voltages less than 500 V [7, p. 81]. The rated voltages of MOSFETs have been constantly growing and today devices rated for 1500 V can be found from many manufacturers.

The electrical symbol and typical current-voltage characteristics of a diode are shown in Figure 3.

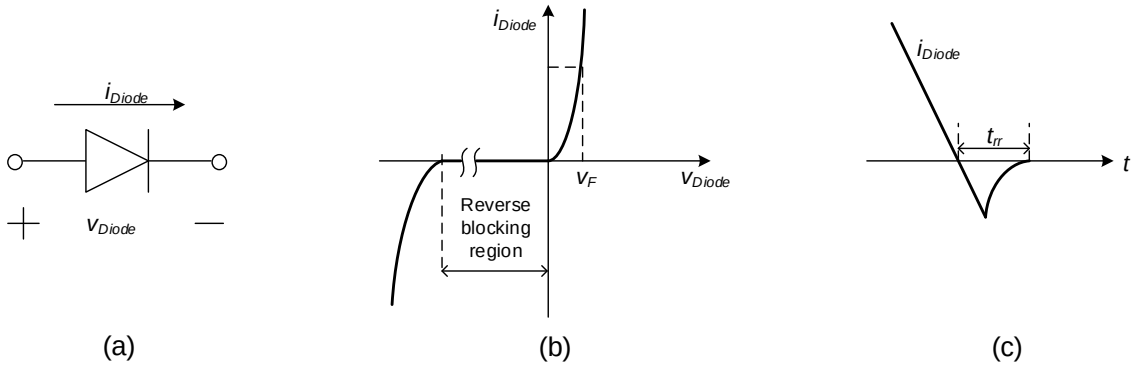

Figure 3: (a) Electrical symbol, (b) current-voltage characteristics and (c) reverse recovery time of a diode.

Figure 3b presents typical characteristics of p-n(positive-negative) junction diode current i_d as a function of voltage v_d. Figure 3b shows that diode conducts current only when forward biased. During conduction, the forward voltage drop v_F is usually less than one Volt. The value of v_F depends on rated blocking voltage and rated current of the component. Moreover when diode is reverse biased, only a negligible small leakage current passes through it. Furthermore, diodes are rated for certain maximum reverse blocking voltages until breakdown happens.

Minority carrier devices such as p-n junction diodes and BJTs(Bipolar junction transistor) typically exhibit reverse recovery characteristics seen in Figure 3c. In Figure 3c, the current i_d starts to decrease rapidly in the beginning of turn off transient. The current decreases below zero to remove stored minority charge from the p-n junction [7, p. 76]. When the minority charge is completely removed, the diode can block the reverse voltage and the current i_d has recovered back to zero within time t_{rr}. A short reverse recovery time is the reason why fast-recovery diodes are used in high frequency applications such as switched mode converters.

MOSFETs are majority carrier devices exhibiting higher on-state resistance but shorter turn off time compared to minority carrier devices. The electrical symbol of n-channel MOSFET and the typical current-voltage characteristics are presented in Figure 4.

MOSFETs are turned on by applying voltage v_{GS} on the gate of a MOSFET. In order to turn on, the applied voltage have to be higher than the threshold voltage v_{th} of the MOSFET. Figure 4b shows typical current-voltage characteristics with different applied v_{GS}. When the voltage v_{GS} is increased the drain current i_D increases

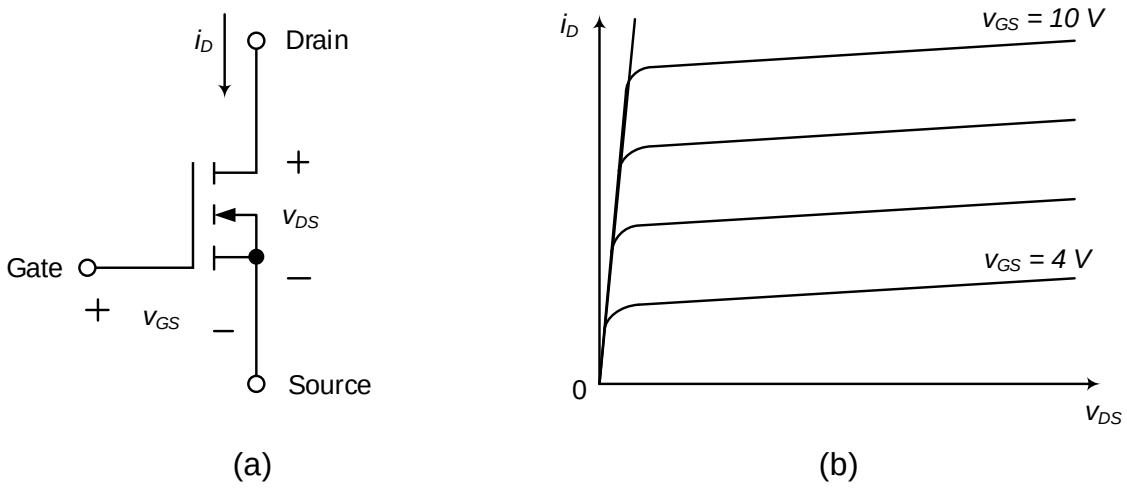

Figure 4: (a) Electrical symbol and (b) current-voltage characteristics of a MOSFET.

rapidly in the saturation region of a MOSFET. A complete MOSFET chip consists of many parallel cells. The operation of the device can be studied from Figure 5, where the structure of one MOSFET cell is shown.

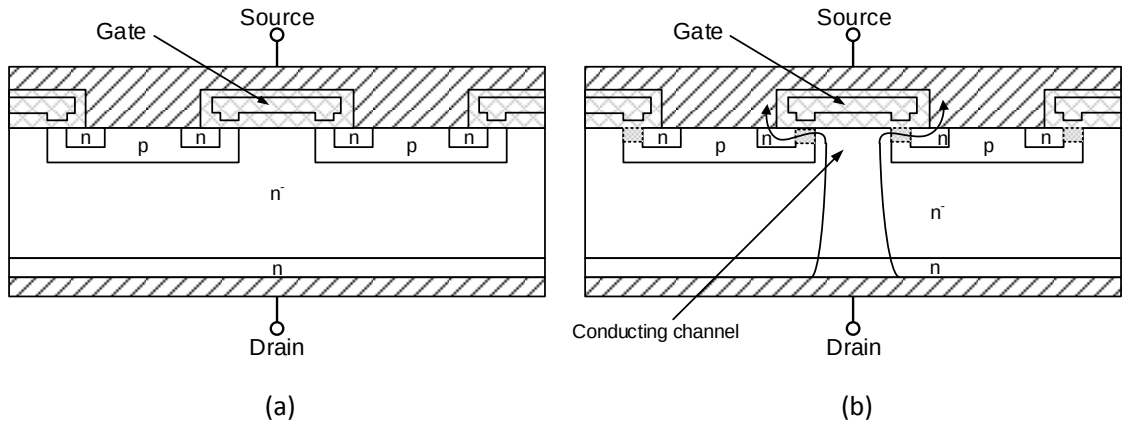

Figure 5: (a) Cross section of a power MOSFET cell and (b) conducting channel in on-state.

Typical MOSFET shown in Figure 5a has metallized drain and source pins, while gate is made of polysilicon. Figures 5a and 5b show the positively and negatively doped regions inside the device. The region marked by n^- is lightly doped and has high resistance when the device is in off-state. In the off-state, both p-n and p-n^- junctions of the device are reverse biased and the current does not flow. When the voltage v_{GS} is applied to the gate, a channel begins to form to positively doped region

underneath the gate. When the threshold voltage is exceeded, the resistivity of the device has dropped and the MOSFET conducts current i_D through the conducting channel shown in Figure 5b.

The power lost in turn on transient is significant in MOSFETs when v_{DS} is above 100 V. This is due to drain-source capacitance c_{DS} in which the energy is stored during the switch turn off. The capacitance is shorted every time the switch is turned on and the stored energy in the capacitance is lost. Following equation has been derived to approximate the lost energy

$$W_{Cds} = \frac{2}{3} c_{DS}(v_{DS}) v_{DS}^2 \tag{2}$$

where c_{DS} is a function of drain-source voltage v_{DS}. Moreover, the square-law dependency of W_{Cds} from v_{DS} can be noted from Equation (2) [7, p. 98-99].

Semiconductor switches are often considered as ideal components when converter circuits are analysed. This idealization means that the state of the switch is either on or off. Furthermore, transient phenomena, forward voltage drop during on state and leakage current during off state are neglected.

2.2.2 Operating principle

A circuit to chop input DC voltage to a lower output voltage can be utilized by a single ideal switch. The resulting circuit and resulting output voltage waveform is shown in Figure 6.

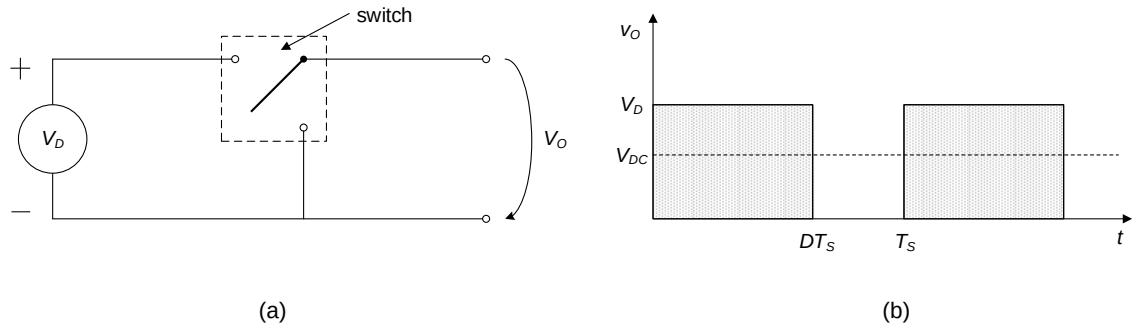

Figure 6: (a) A chopper circuit to decrease DC voltage and (b) the resulting output voltage waveform.

The switch in Figure 6a can have two different positions. It can connect the output v_O to the positive terminal of the DC input source V_D or alternatively it can short circuit the load. The resulting steady state output voltage waveform is shown in Figure 6b The value of output voltage v_O is V_D during the time the switch is connected to the positive terminal. This time is called the switch conduction time or on time. Likewise, the time the switch short circuits the load is called the off time and during that time the output voltage is zero. Furthermore, the switching period T_S is known to be inversely dependent on switching frequency $T_S = \frac{1}{f_S}$.

By using the circuit shown in Figure 6a, the resulting DC value of the output voltage has decreased to a level depending on the switch duty ratio D. The DC component of the output voltage V_O can be calculated by integrating the time dependent value of output voltage $v_O(t)$ over one switching period T_S [6, p. 66]

$$V_O = \frac{1}{T_S}\int_0^{T_S} v_O = \frac{1}{T_S}\left(\int_0^{t_{on}} V_D \cdot dt + \int_{t_{on}}^{T_S} 0 \cdot dt\right) = \frac{t_{on}}{T_S}V_D = DV_D \tag{3}$$

where t_{ON} is the on time of the switch, D is the duty ratio and V_D is the input source voltage. Although the DC voltage can be decreased using the circuit shown in Figure 6a, the resulting output voltage contains a high amount of harmonics which are multiples of the switching frequency. The DC component, the fundamental switching frequency and the harmonics, produce the distorted output voltage waveform shown in Figure 6b.

In order to be used in practical applications, the output has to be filtered to get rid of distorted voltage waveform of Figure 6b The desired characteristics are realized by using LC filter in the output of the converter.

In a practical step-down buck converter, the switch shown in Figure 6a is realized by using a semiconductor switch, such as MOSFET, in series to the input voltage source. In addition to the MOSFET, a freewheeling diode is needed to provide path for the inductive current present in the true converter circuit during off time of the switch. The circuit of a buck converter is shown in Figure 7.

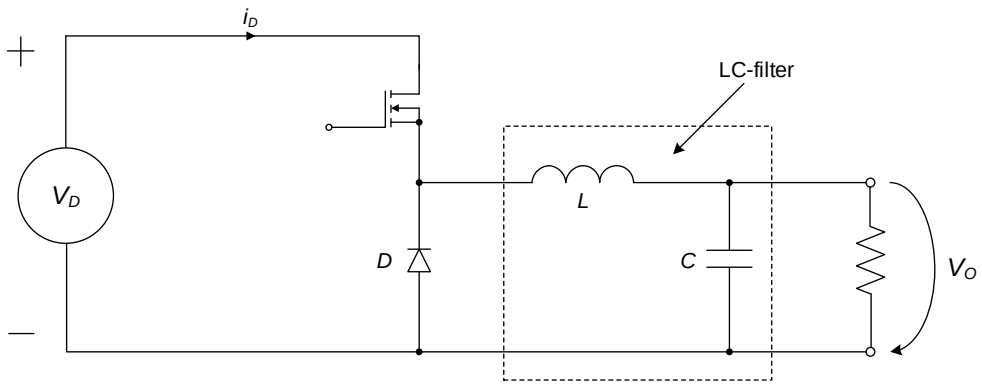

Figure 7: Step-down buck converter circuit.

The LC filter in Figure 7 consists of inductance L in series and capacitance C in parallel to the load connected to the output of the converter. The corner frequency of the LC filter is chosen to be lower than the switching frequency to provide desired low-pass characteristics [6, p. 66].

In order to analyze the operation of the buck converter in steady state, the operation of the circuit with idealized components is shown in Figure 8 and Figure 9.

During the switch on time, the switch is considered as short circuit as shown in Figure 8a. The supply voltage V_D appears over the diode and the voltage v_L over the

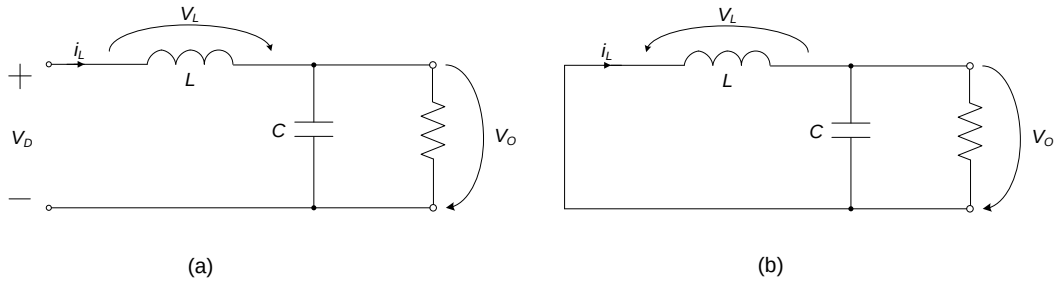

Figure 8: Buck converter:(a) switch on (b) switch off.

inductance becomes $V_D - V_O$. The inductor current i_L can't change instantaneously and its rate of change follows the well known definition

$$\frac{di_L}{dt} = \frac{v_L}{L} \tag{4}$$

where L is the value of inductance [9, p. 14], [7, p. 17]. Equation (4) can be modified to following form to present a change in inductor current di_L during a time interval Δt

$$di_L = \frac{v_L \cdot dt}{L} \tag{5}$$

When the switch turns off, the current of the inductor forces the voltage over the inductor to reverse polarity. The value of v_L is now equal to $-V_O$ and the rectifying diode is forward biased. Therefore, according to Figure 8b, the inductor current i_L flows to the output load. The resulting inductor voltage v_L and current i_L waveforms are shown in Figure 9. In Figure 9, the waveform of the inductor voltage v_L is positive during t_{on} and the inductor current grows according to the Equation (4). During t_{off}, the polarity of v_L is negative and the inductor current decreases. The DC level of the inductor current I_L is the same as the output current I_O of the converter.

The ripple current of the inductor , shown in Figure 9, flows through the capacitor of the LC filter. This ripple current charges and discharges the capacitance according to a definition of capacitors rate of voltage change [10, p. 179]

$$\frac{du_C}{dt} = \frac{i_C}{C} \tag{6}$$

where i_C is the capacitor current. Equation (6) shows that the value of output voltage ripple depends on the value of capacitance.

Operation of buck converter is limited to only step-down applications. However, if the output voltage is needed to be higher than input voltage, a step up boost converter can be used. The arrangement of the circuit elements differs slightly from buck converter. If compared to the buck converter circuit shown earlier in Figure 7, the inductance L has been moved to the input side of the circuit. In addition, the positions of MOSFET switch and the diode have been moved. The boost converter and equivalent switching circuits are shown in Figure 10.

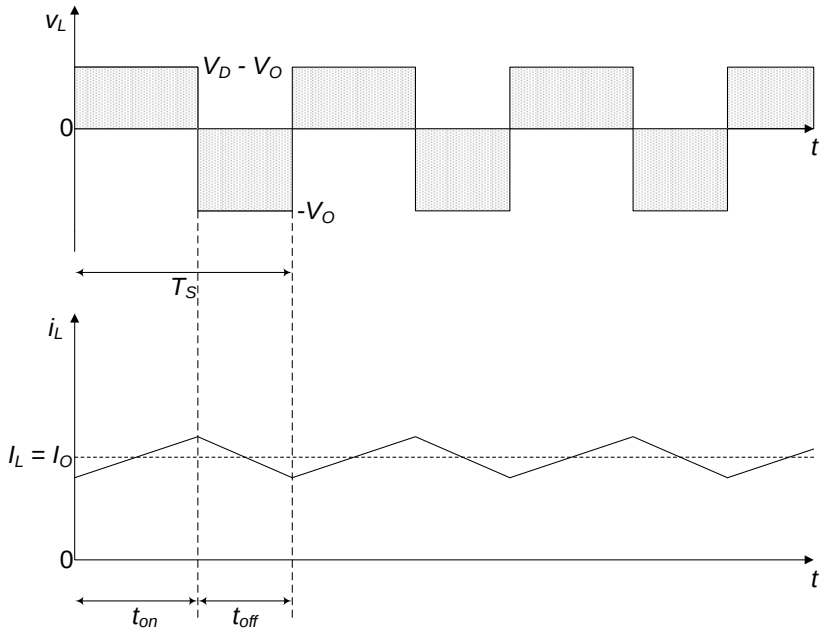

Figure 9: Steady state inductor voltage and current waveforms of buck converter.

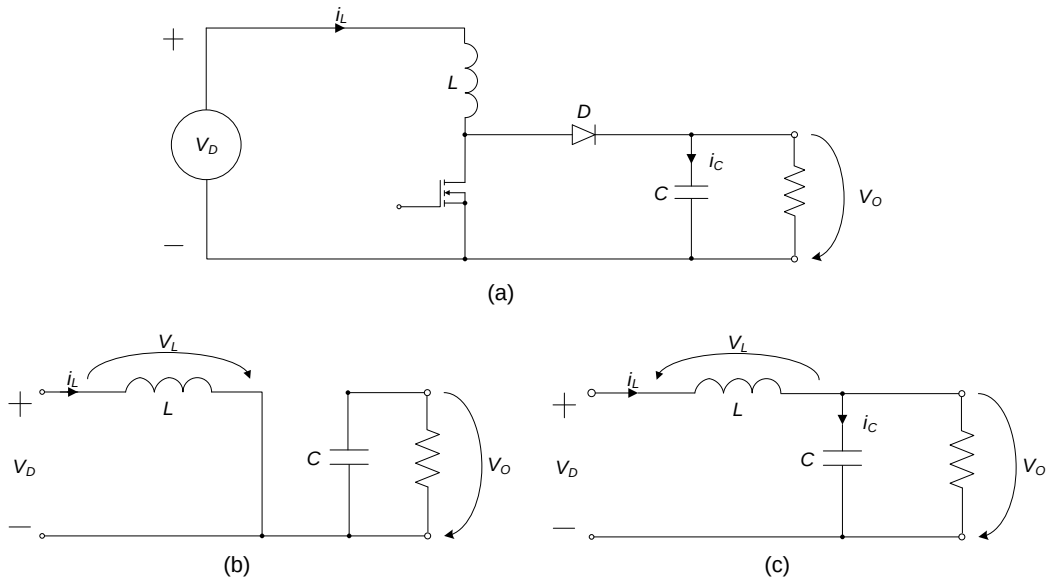

Figure 10: (a) Step-up boost converter and the equivalent circuits during (b) switch on and (c) switch off.

During the switch on-time, shown in Figure 10b, the MOSFET switch connects the inductance L to the negative terminal of V_D. A negative voltage is applied to the anode of the diode and it becomes reverse biased. The inductor current increases according to equation (4) and only the capacitor C supplies energy to output. The equivalent circuit during switch off-time is shown in Figure 10c. The diode becomes

forward biased as the voltage on the anode turns positive. Current starts flowing from the inductor to the capacitor, replenishing the drained charge of the capacitor. In addition to inductor, energy is supplied to the capacitor by the input source during the switch off-time [9, p. 32].

2.2.3 Steady state operation of buck-boost topology

A buck-boost converter can be realized by combining buck and boost converters into a single converter. The advantage of buck-boost converter against either buck or boost topologies is that the output voltage can be lower or higher than the input voltage. The steady state output voltage transfer function is the same as the product of transfer functions of the two separate converters [6, p. 81]. Moreover, the output voltage polarity of buck-boost topology is reverse. The electrical circuit of buck-boost converter and the operation is presented in Figure 11.

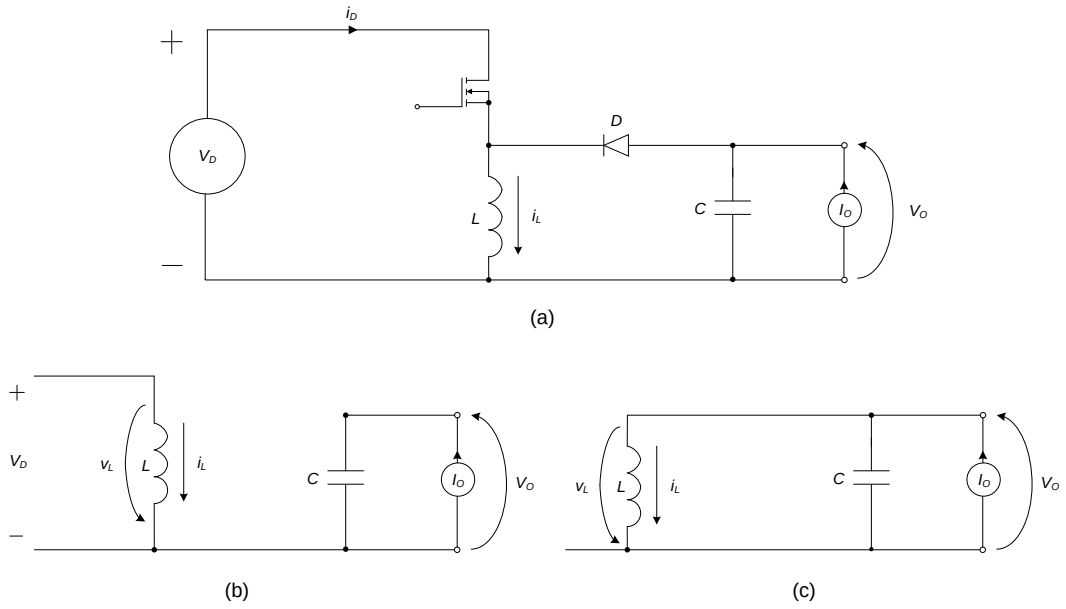

Figure 11: (a) Electrical circuit of buck-boost converter and the equivalent circuits during (b) switch on and (c) switch off.

Figure 11a show the differences to the two other converter circuits presented in Section 2.2.2. The most notable difference is the position of the inductor between the MOSFET and the negative input terminal. In addition, the diode has been turned around to conduct current to the opposite direction. The MOSFET stays at the same position as in the buck converter seen in Figure 7.

When the switch is on, the inductor voltage v_L is the input voltage V_D as can be seen from Figure 11b. Conversely, Figure 11c shows that the polarity of v_L has reversed equalling to $-V_O$ during the off period. The diode in Figure 11a has become forward biased releasing the inductor current to flow to the load.

Ćuk [11] and Mohan et al.[6, p. 82-84] have presented the steady state operation of buck-boost converter in different operation modes. In the CCM(continuous con-

duction mode), the inductor current never reaches zero remaining continuous at all times. In BCM(boundary conduction mode), the inductor current is at the mode boundary. This means that the current reaches zero right at the switch off- and on-time boundary. The inductor current becomes discontinuous in DCM (discontinuous conduction mode). This means that the current remains zero for a fraction Δt of switching period. Figure 12 shows the inductor current waveforms in different conduction modes.

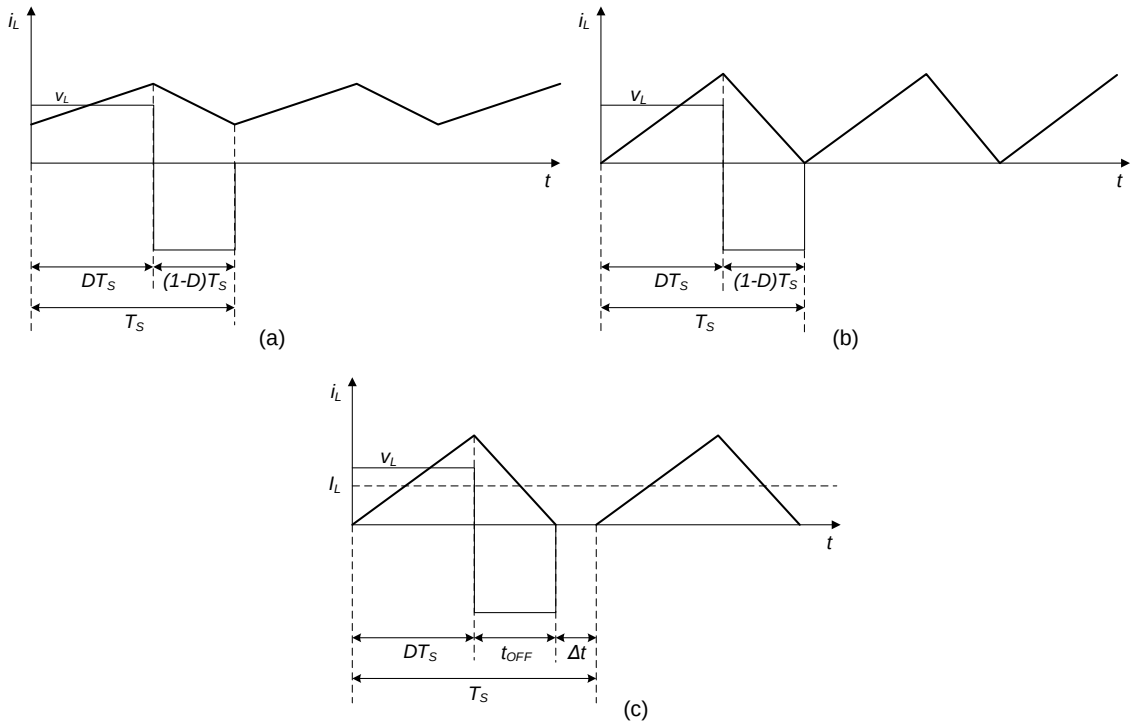

Figure 12: Inductor current waveforms: (a) CCM (b) BCM (c) DCM.

Figure 12a shows that when a converter is operated in CCM, the inductor energy transfer is incomplete and the current waveform consists of a peak-to-peak ripple on top of a DC component. The output voltage V_O in CCM can be derived as a function of duty ratio D by equating the integral of inductor voltage v_L to zero over one switching period T_S:

$$V_D DT_S + (-V_O)(1-D)T_S = 0 \tag{7}$$

$$V_O T_S - V_O DT_S = V_D DT_s$$

$$\frac{V_O(1-D)}{D} = V_D$$

$$V_O = V_D \frac{D}{1-D} \tag{8}$$

In Figure 12b and Figure 12c, all the energy stored in the inductor is transferred during one switching cycle. This means that the current is zero and the inductor is completely reset. The critical conduction mode, shown in Figure 12b, determines the limit of operating in CCM and DCM. If the switch on-time is further decreased from BCM, the current becomes discontinuous and the operation mode changes to DCM. To be noted from Figure 12c, the switching period T_S in DCM consists of three time intervals instead of two in the two other conduction modes. The resonance time t_{res} is added to t_{on} and t_{off} to establish the full period.

The output voltage in DCM can be derived by first calculating the DC level of inductor current in the current waveform of i_L in Figure 12c using Equation (5)

$$I_L = \frac{V_D D T_S}{2L} \tag{9}$$

where DT_S is the on-time of the switch. Moreover, the DC value of input current I_D can be calculated by

$$I_D = D I_L \tag{10}$$

Inserting Equation (9) to (10) yields

$$I_D = \frac{V_D D^2 T_S}{2L} \tag{11}$$

Using DC values, a relation can be found for input and output powers of the converter

$$\eta P_{in} = P_{out} \tag{12}$$

which can be presented also in the following form

$$\eta V_D I_D = V_O I_O \tag{13}$$

Inserting Equation (11) to (13), the output voltage V_O in DCM is obtained

$$V_O = \eta \frac{V_D^2 D^2 T_S}{2L I_O} = \eta \frac{V_D^2 t_{on}^2 f_{sw}}{2L I_O} \tag{14}$$

where on time is calculated by $t_{on} = DT_S = \frac{D}{f_{sw}}$.

If efficiency of the converter, input voltage, output power and switching frequency are known, the needed inductance can be calculated by modifying Equation (14) to the following form

$$L = \frac{(V_D - v_{drop})^2 t_{on}^2 f_{sw}}{2(V_O + v_F) I_O} \tag{15}$$

where v_{drop} is the voltage drop due to the resistance of the MOSFET $R_{DS,on}$ and the winding R.

By comparing Figure 12a and Figure 12c, we can note that the ripple component of the two current waveforms is higher in DCM if both waveforms have the same DC component. Therefore according to Equation (5), the inductance value required in DCM is smaller, which usually means a physically smaller inductor. On the other

hand, higher current ripple means higher transistor peak currents and a higher output capacitor current ripple [10, p. 123].

2.2.4 Single switch flyback converter

As the output voltage of buck-boost converter can be lower or higher than the input voltage, the same applies to flyback converter. Flyback converter is based on buck-boost topology but they differ from the magnetic circuit, which in flyback provides galvanic isolation and turns ratio $N_{PS} = \frac{N_P}{N_S}$ between primary and secondary winding. The magnetic circuit of flyback converter is often called flyback transformer. However, unlike a typical transformer, current in flyback transformer does not flow in primary and secondary windings at the same time and the transformer behaves like a coupled inductor. Rightly, the transformer is to be considered as an inductor when analyzing the behaviour of the flyback circuit [9, p. 117-120].

Typical flyback circuit resembles the buck-boost circuit of Figure 11a but the inductor is replaced by a coupled inductor. In addition, the ends of secondary winding have been turned around and the diode is typically drawn to the positive end of the winding. The basic electrical circuit of flyback converter and the equivalent circuits during t_{on} and t_{off} are shown in Figure 13. Moreover, leakage elements or equivalent resistances of an actual converter are not included in Figure 13.

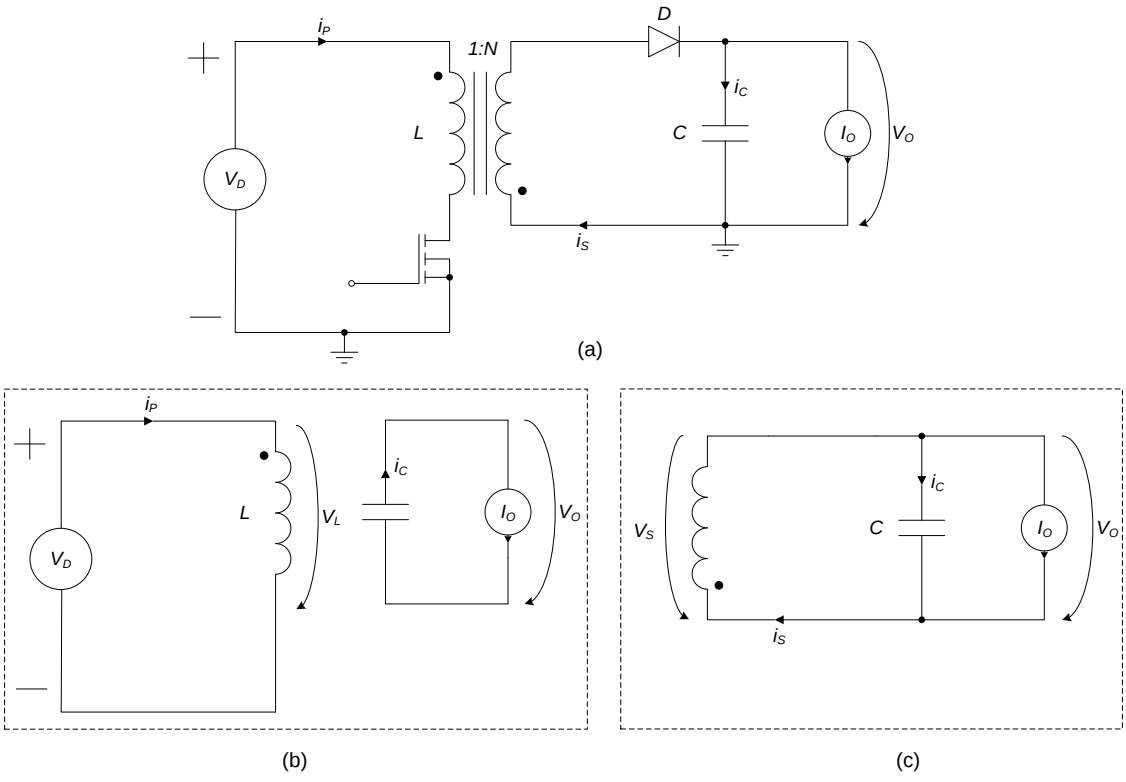

Figure 13: Flyback converter: (a) Electrical circuit and the equivalent circuits during (b) switch on and (c) switch off.

In Figure 13a, the primary and secondary currents, i_P and i_S, enter the coupled

inductor from the ends of windings marked by black dots. In addition, the placement of the MOSFET, below the inductor, enables a more practical implementation of feedback and control circuitry than in buck-boost topology.

During the MOSFET on-time in Figure 13b, the input voltage V_D is applied over the primary winding of the coupled inductor. The current i_P rises linearly to the peak value i_{Ppk} according to Equation (5). During on-time, the freewheeling diode in the secondary remains reverse biased blocking the flow of the secondary current i_S. Furthermore, the output current I_O is supplied entirely by the capacitor C and the charge of the capacitor decreases.

During off-time in Figure 13c, the voltage v_S trying to resist a change of the magnetic flux is induced over the secondary winding. In consequence, the freewheeling diode becomes forward biased and the current i_S begins to flow to the output of the converter. The current in the coupled inductor decreases from the peak value i_{Spk}

$$i_{Spk} = N_{PS}^2 \cdot \frac{V_O \cdot t_{off}}{L} \tag{16}$$

where N_{PS} is the turns ratio, V_O is the desired output voltage, t_{off} is the off-time and L is the value of required inductance [1]. Furthermore, the decreasing inductor current replenishes the decreased charge of the output capacitor.

When the MOSFET is turned off, the voltage stress v_{DS} over the MOSFET becomes to

$$v_{DS} = V_D + v_r + v_{spike} \tag{17}$$

where V_r is the voltage reflected from the secondary winding and the v_{spike} is a voltage spike due to leakage inductance of the flyback transformer. Moreover, the reflected voltage v_r in Equation (17) can be calculated as

$$v_r = N_{PS}(V_O + v_F) \tag{18}$$

where v_F is the forward voltage drop of the diode. During the turn off transient, the voltage spike v_{spike} is also reflected to the secondary. Figure 14 presents the typical current and voltage waveforms of a flyback converter in DCM.

Two resonances can be seen from the typical waveforms of v_{DS} and v_S in Figure 14. The first resonance, having higher frequency, occurs between the leakage inductance L_l of the coupled inductor and the parasitic capasitance c_{DS} of the MOSFET. The peak value of this resonance v_{spike} has to be taken into account when calculating the maximum voltage stress of the MOSFET during t_{off} with Equation (17). A Typically used value of the peak has been is $v_{spike} = 0.3 \cdot V_D$ [9, p. 130]. The effect of the resonance, caused by the leakage inductance, is decreased by using dissipative voltage snubbers [12].

The second resonance, occuring when the inductor current has decreased to zero, forms between the inductance L_P of primary winding and the parasitic capacitance c_{DS} of the MOSFET. The resonance time equals the discontinuous time Δt between t_{OFF} and the next turn on shown in Figure 14.

The frequencies of the resonances can be calculated by

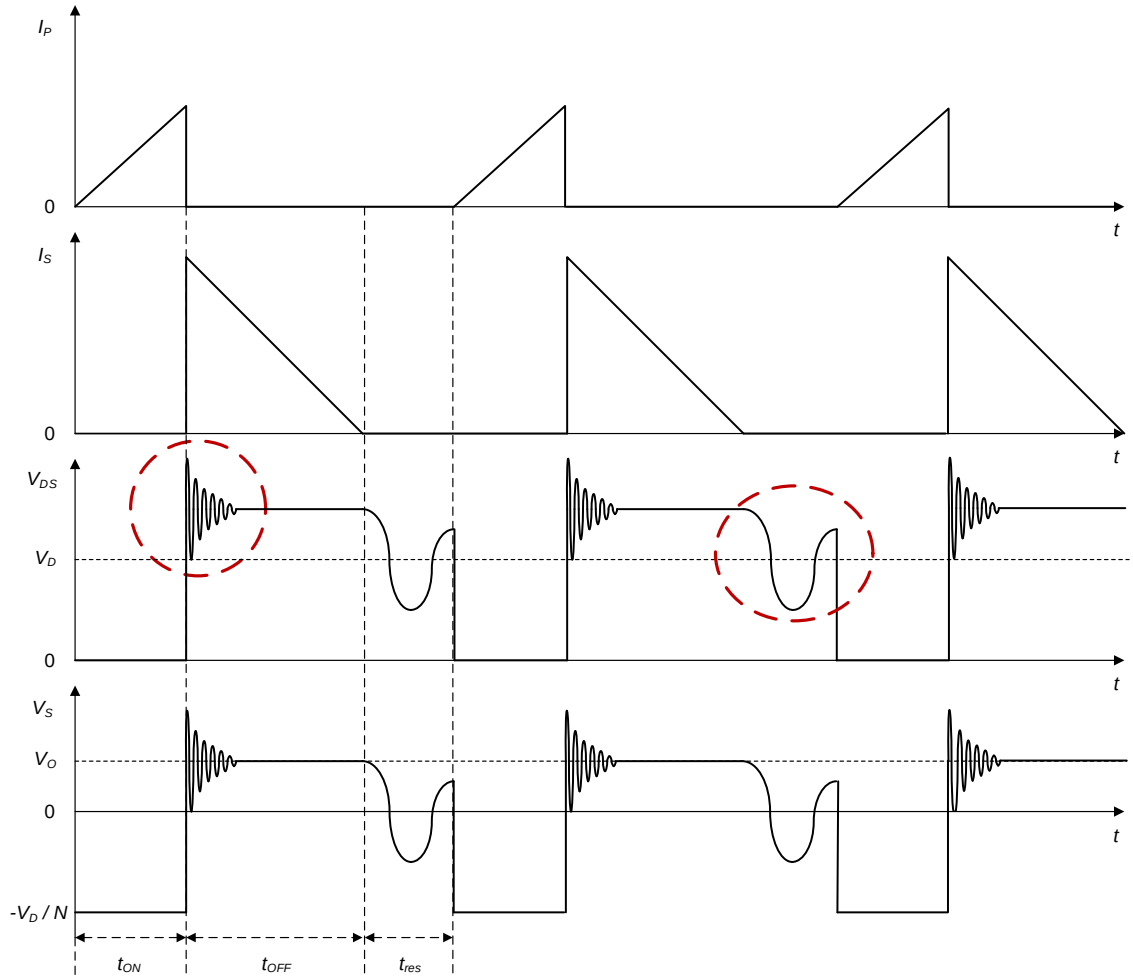

Figure 14: Waveforms of a flyback converter operated in DCM. The dashed, red circles highlight the two resonances in the waveform of v_{DS}.

$$f_{res} = \frac{1}{2\pi\sqrt{L_P \cdot c_{DS}}} \tag{19}$$

where L is the inductance of primary winding forming the resonance and the c_{DS} is the parasitic capasitance between drain and source of the MOSFET [1].

A common problem with flyback converters having wide input voltage ranges is that the duty ratio in DCM approaches zero as the input voltage approaches the upper limit. Consequently, the MOSFET may not turn on compeletely and reach the saturation region, which increases the losses of the converter and decreases the reliability of operation. [13]

2.2.5 Double ended flyback converter

If the voltage stress during off-time of the transistor becomes a problem, a double transistor flyback circuit, shown in Figure 15, could be used instead of the topology

presented in 2.2.4.

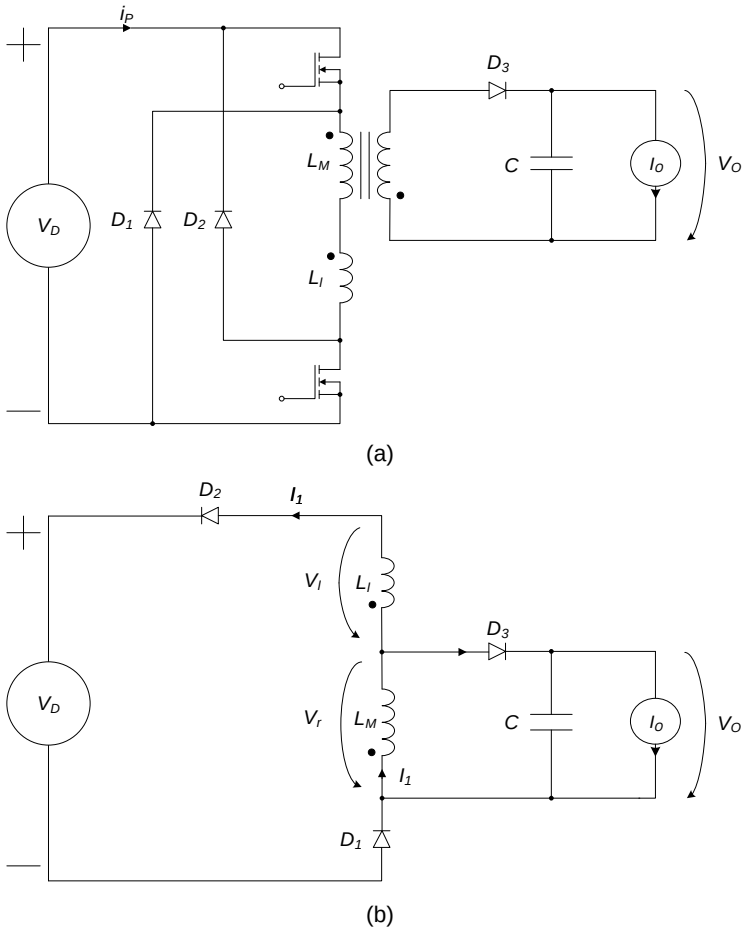

Figure 15: Double ended flyback converter: (a) electrical circuit and (b) equivalent circuit during MOSFET turn off transient.

The main advantage of using the circuit of Figure 15a is that the voltage stress of the MOSFET is limited to the input voltage V_D during off-time. This restriction is established by clamping the negative terminal of V_D through the diode D_1 to the dot end of the coupled inductor. The other end of the inductor is clamped to the positive terminal V_D through the diode D_2 [10, p. 19].

The inductance of the coupled inductor in Figure 15 is divided to the magnetizing part L_M and the parasitic leakage part L_l. In the double ended flyback circuit, the energy stored in the leakage inductance during on-time is delivered back to the input source during the turn off transient.

Energy stored in an inductor can be calculated by

$$E = \frac{1}{2} L I^2 \tag{20}$$

where I denotes the peak value of inductor current. From figure 15b we can see that the current I_1 flows through L_l as well as through L_M during the turn off

transient. Moreover, the voltage over L_M is the reflected secondary voltage v_r and if the voltage stress over the MOSFET is limited to V_D, this leaves the rest of the input voltage $V_D - v_r$ over the L_l. In order to maximize the energy transfer from L_M to the output, the time the current I_1 flows through L_l should be minimized.

According to Equation (4), the decay time of the inductor current depends on the applied voltage. Thus setting a lower primary to secondary turns ratio N_{PS} leaves higher protortion of the input voltage over the leakage inductance which decreases the time needed for the current I_1 to reset to zero in L_l [9, p. 157-160]. Alternatively, choosing a higher turns ratio slows down the resetting.

The disadvantage of the double ended flyback converter compared to the single switch topology is the addition of two clamping diodes D_1, D_2 and the second MOSFET. Moreover, choosing the double ended over the single ended topology does not give advantage over the problem with MOSFET resulting from wide input voltage ranges.

2.2.6 Quasi-resonant control of flyback converters

The output voltage of flyback converters is regulated by closing a feedback loop from the output to the control circuit. In the control circuit, the value of output voltage is compared to the voltage reference and the gate control signal of the MOSFET is changed according to the difference. The gate control signal turns the MOSFET on and off as described in 2.2.1.

In order for the transformer to provide galvanic isolation between primary and secondaries, the feedback loop has to be isolated from the output. Furthermore, the regulation from the output is typically realized by using an opto-isolator between the controller and error from the voltage reference V_{ref}.

In flybacks operated in DCM, turn on of the MOSFET may occur at any time during the resonance between the inductance of primary winding and the parasitic drain-source capacitance of the MOSFET. The lost energy, during switching, can be approximated by Equation (2) as described in 2.2.1. From Equation (2) we can note that the lost energy is dependent on the voltage v_{DS} by square law at the event of turn on. In order to minimize the switching losses, the turn on should occur at the valley of the resonance. Figure 16 presents a typical feedback loop in flyback converters.

The valley of the resonance is used for timing the switching in QR (quasi-resonant) controllers. The QR controller initiates the next turn on of the MOSFET based on the slope of the voltage of the auxiliary winding seen in Figure 16 [14, p. 5]. In addition to the knowledge of the converter state, the winding provides operating voltage v_{CC} to the control circuit. The waveform of the voltage in the auxiliary winding equals to reflected voltage v_r but is scaled down by a turns ratio N_{AUX} according to

$$N_{AUX} = \frac{N_P}{N} = \frac{v_r}{v_{CC} + v_{FCC}} \tag{21}$$

where N is the number of turns in the auxiliary winding, v_{FCC} is the forward voltage

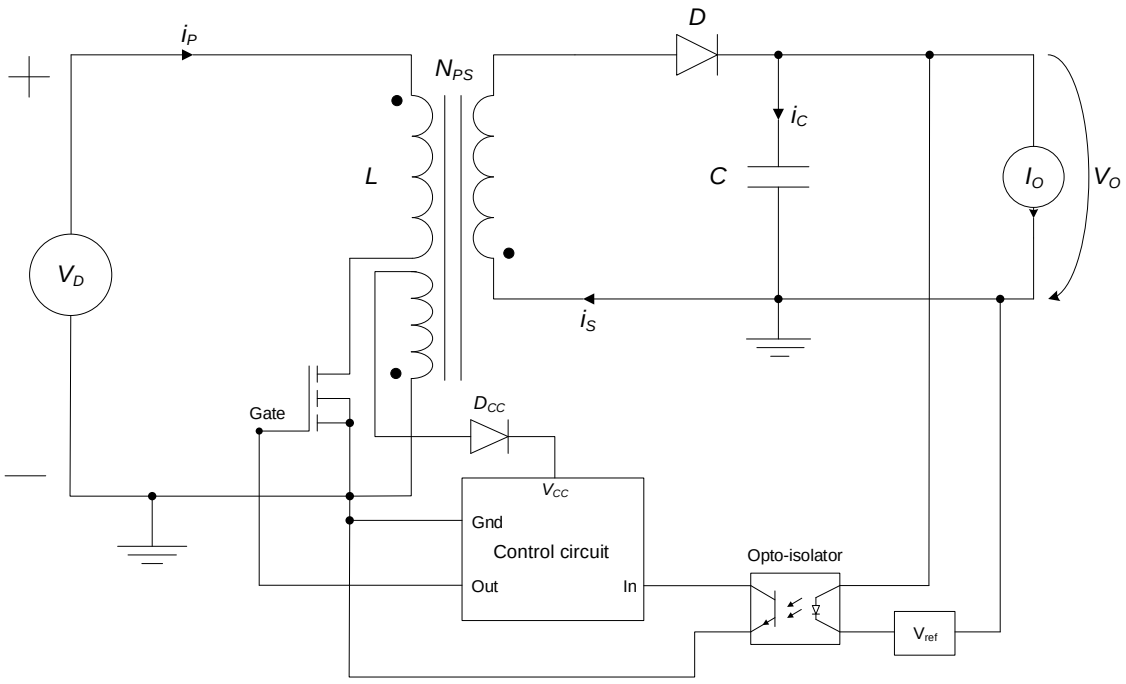

Figure 16: A typical control loop of a flyback converter.

drop of the diode D_{CC}.

QR controllers modulate the switching frequency as a function of input voltage and load current. In addition to switching frequency, some controllers will also modulate the primary peak current. Because the QR operation requires zero crossing or slope detection from the waveform of v_{CC} to initiate the switching, the controller forces converters to operate in DCM. Figure 17 shows the primary winding and the MOSFET drain-source voltage waveforms in traditional fixed frequency and QR controlled flyback converters. [15]

The differences in the waveforms of v_{DS} can be noted from Figure 17. The traditional hard switching controller changes the duty ratio in order to achieve desired output voltage. At the switch turn on, the voltage v_{DS} can be any value of the resonance depending on the discontinuous time Δt. Instead, for example the UCC28600 QR controller from Texas Instruments modulates switching frequency and peak current of primary by keeping the duty ratio unchanged in QR region. Figure 18 presents the operation of UCC28600 in which the switching frequency f_{sw} and peak current i_{Ppk} are modulated as a function of required output power.

The QR region in Figure 18 is the highest on-time the converter can achieve with a given input voltage. In order to keep the duty ratio unchanged, the switching frequency has to be between the minimum frequency $f_{sw,min}$ and maximum frequency $f_{sw,max}$ clamps of the controller. The $f_{sw,max}$ is reached if the input voltage increases or the load current decreases. As a result, the controller begins to operate in DCM keeping the switching frequency fixed. [15, p. 11].

As the load current has decreased to approximately 30 percent of the maximum

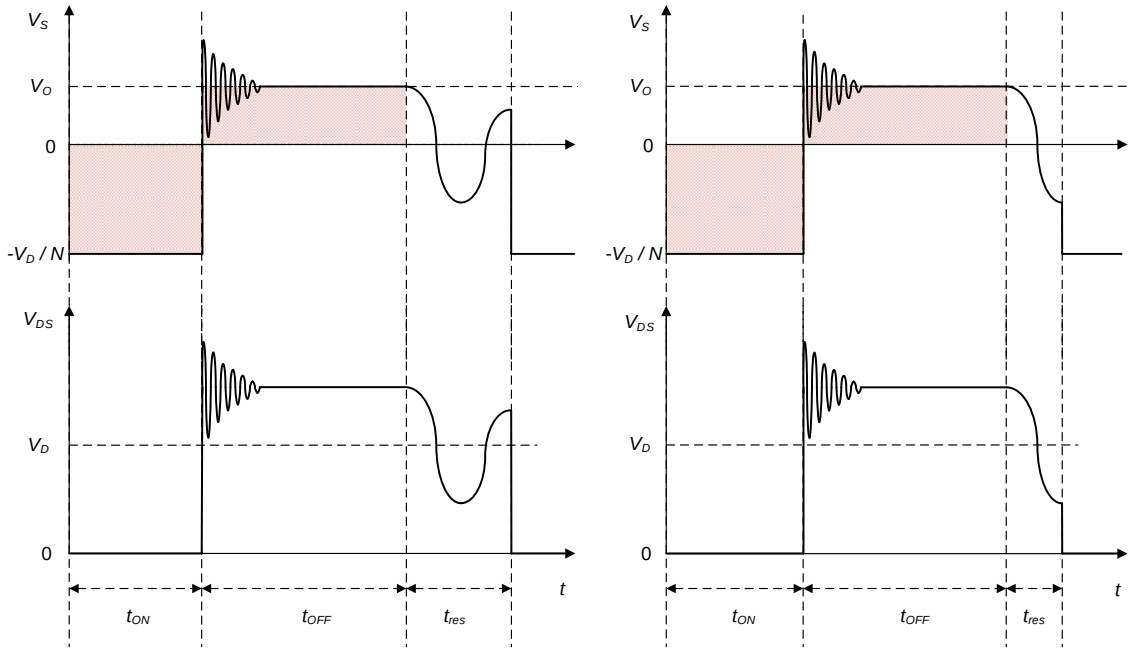

Figure 17: Secondary winding and drain-source voltage waveforms of a flyback converter controlled in DCM. Traditional hard switching on the left and QR on the right.

value, the controller begins to operate in FFM (frequency foldback mode). Output voltage regulation in FFM is achieved by modulating the switching frequency between the f_{max} and f_{min} clamps as the peak value of primary current is kept constant. If the load current is approximately below 10 percent of the maximum, the controller operates in green mode. In green mode, bursts of 40 kHz pulses are applied to the gate of the MOSFET and the average switching frequency becomes less than f_{min} as can be seen from Figure 18. [15, p. 11, 13.]

Converters timing the turn on of the switch to the valley of the resonance are said to be soft switching. Apart from lower losses, another important advantage of soft switching is lower conducted and radiated EMI (electromagnetic interference) compared to the typical switching.

The highest on-time in QR is calculated from the energy balance of the converter. The voltage of the secondary winding has the same three time periods during one switching cycle as the converter operated in DCM. The switching period T_S can be equated

$$T_S = t_{on} + t_{off} + t_{res} \tag{22}$$

where t_{res} is half of the resonance period and can be calculated by $t_{res} = \frac{1}{2f_{res}}$.

To maintain energy balance in steady state, the integral of the applied inductor voltage must be zero over one switching period. This means that the volt-second products marked by coloured areas in Figure 17 must be equal [7, p. 20-21]. Equating the primary side volt-second products equal, as with the buck-boost converter in

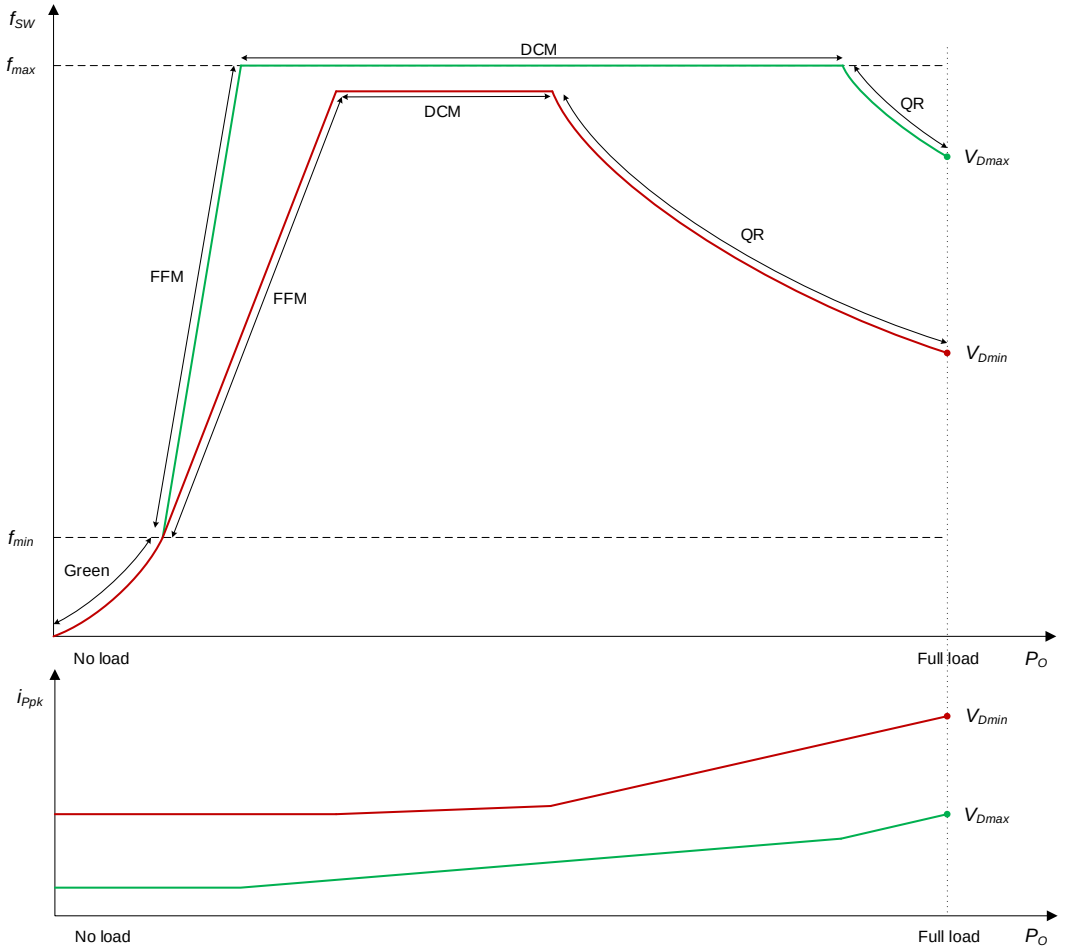

Figure 18: Switching frequency and peak primary current of a converter using UCC28600 QR controller. Different operating modes of the controller, QR, DCM, FFM and green, as function of load current and switching frequency with two input voltages. [1, p. 9].

Equation 7, the off-time t_{off} can be calculated

$$V_D t_{on} = v_r t_{off} = N_{PS}(V_O + v_F) t_{off} \tag{23}$$

$$t_{off} = \frac{V_D t_{on}}{N_{PS}(V_O + v_F)} \tag{24}$$

Inserting Equation (24) to Equation (22), the on-time t_{on} of QR controlled flyback converter can be solved

$$t_{on} = \frac{N_{PS}(V_O + v_F)(T_S - t_{res})}{(V_D - v_{drop}) + N_{PS}(V_O + v_F)} \tag{25}$$

If the turns ratio N_{PS} is wanted to be calculated according to the maximum duty cycle of the MOSFET D_{max} and the duty cycle of the resonance D_{res}, Equation 25

can be modified to the following form, which includes the voltage drop v_{drop} due to the resistance of the MOSFET during on time

$$\begin{aligned} D_{max} &= \frac{N_{PS}(V_O + v_F)(1 - D_{res})}{(V_D - v_{drop}) + N_{PS}(V_O + v_F)} \\ D_{max}(V_D - v_{drop}) + N_{PS}(V_O + v_F)) &= N_{PS}(V_O + v_F)(1 - D_{res}) \\ D_{max}(V_D - v_{drop}) &= N_{PS}(1 - D_{res} - D_{max})(V_O + v_F) \end{aligned}$$

which leads to the turns ratio of QR controlled flyback converter

$$N_{PS} = \frac{D_{max}(V_D - v_{drop})}{(1 - D_{res} - D_{max})(V_O + v_F)} = \frac{D_{max}}{1 - D_{max} - D_{res}} \frac{V_D - v_{drop}}{V_O + v_F} \tag{26}$$

This section described the operation of switched mode converters and the related power electronic devices. In addition, the quasi-resonant control topology was presented. In the following section, the magnetic circuit of the flyback converter will be studied.

2.3 Flyback transformer

The important tasks of a flyback transformer are to provide energy storage and coupling with galvanic isolation to a flyback converter. A typical flyback transformer has single primary, one or more secondaries and one auxiliary winding. The auxiliary winding is used for the needs of control circuit, as shown in 2.2.6. A single flyback converter is often used for powering loads with differing needs by means of different voltages or requirements for protection. Consequently, multiple secondaries may be needed with differing primary to secondary turns ratios.

This section presents the needed theory, construction and parameters to design flyback transformers. Furthermore, the manufacturing process of flyback transformers is described.

2.3.1 Basic theory of magnetics

Maxwell equations sum up the experimental laws of electromagnetics. The laws are useful when designing magnetic components in power electronic converters. Ampere's law defines the magnetic field intensity vector $\vec{H}$ in a current carrying conductor. According to Ampere's law, current in a conductor produces a magnetic field around the conductor. Figure 19a demonstrates Ampere's law in a coil with four turns. The direction of the magnetic field in a coil can be found with the right-hand rule. The vector of the magnetic field intensity points to the direction of the thumb, if the current in the coil flows to the direction pointed by other fingers. Moreover, the law states that if $\vec{H}$ is integrated around a closed loop, the result equals the total current passing through the loop. The resulting MMF (magnetomotive force) of the coil can be written as

$$\oint_l \vec{H} \cdot \mathrm{d}l = \oint \vec{J} \cdot \mathrm{d}S = Ni \tag{27}$$

where $\vec{H}$ is the magnetic field intensity, $\vec{J}$ is the current density vector, $\mathrm{d}S$ is the area of $\vec{J}$, N is the number of turns and i is the current in the coil. [16, p. 2.]

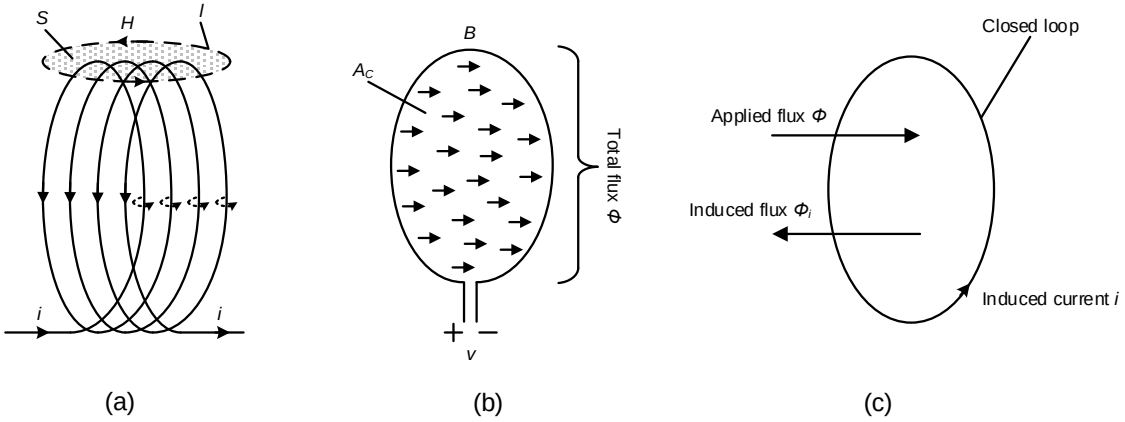

Figure 19: Demonstrations of Maxwell equations: (a) Ampere's law, (b) Faraday's law and (c) Lenz's law.

The magnetic field intensity produces magnetic flux density B in a material

$$B = \mu_0 \mu_r H = \mu H \tag{28}$$

where μ_0 is the permeability in vacuum, μ_r is the relative permeability of the material, μ is a special characteristic permeability of the material and the H is the magnetic field intensity. The value of μ_0 is constant equal to 4π*10^{-7} H/m. [16, p. 2-3.]

A total magnetic flux Φ can be found by integrating the magnetic flux density over a surface S. If the B is uniform and perpendicular to the surface S, the integral can be written in the following form

$$\Phi = \int_S \vec{B} \cdot \mathrm{d}S = BA_c \tag{29}$$

where $\vec{B}$ is the vector of the flux density, B is the magnitude of uniform flux density and $\mathrm{d}S$ is the perpendicular surface equal to the area A_c. [16, p. 1-3.]

According to Faraday's law, if a total flux which varies in time passes through a loop, a voltage is induced to the loop. The loop in Figure 19b represents a winding in which the voltage v is induced by the total flux Φ. The induced voltage v is given by the time derivative of the total flux

$$v = \frac{\mathrm{d}\Phi}{\mathrm{d}t} \tag{30}$$

If the flux is uniformly spread over the internal area A_c of the winding, inserting Equation (29) to Equation (30) yields

$$v = \frac{\mathrm{d}\Phi}{\mathrm{d}t} = A_c \frac{\mathrm{d}B}{\mathrm{d}t} \tag{31}$$

where A_c is the internal area and B is the uniform flux density. [7, p. 496.]

According to Lenz's law, a flux applied to a closed loop induces a current i to the loop as shown in Figure 19c. As a result, this current induces a flux Φ_i to oppose the changes in the applied flux Φ. [7, p. 492-493.]

Analogous to Kirchoff's law for electrical quantities, the Gauss's law states that the flux Φ going in to a surface must equal the flux passing through the surface in a closed magnetic path. This relation applies to all closed magnetic circuits and it can be modeled the same as Kirchoff's law for current in different nodes. The Gauss's law is mathematically given by

$$\oint_S \vec{B} \cdot \mathrm{d}S = 0 \tag{32}$$

where B is the flux density and the $\mathrm{d}S$ is the surface the flux passes through. Equation (32) states that the net flux through a surface must be zero. [7, p. 499.]

2.3.2 Magnetic core

In Figure 20a, a coil with an air core emits the magnetic field out to surroundings. However, if the coil is spooled on a magnetic core with the permeability $\mu_r \gg 1$, a path of low magnetic resistance is provided for the flux and the magnetic field stays almost entirely inside the core. Furthermore, the magnetic path length l_e can be accurately determinated which could otherwise be difficult. [17, p. 6-7.] Figure 20b presents a winding spooled around the magnetic core.

Because the current i in Figure 20 is related to the magnitude of the magnetic field H by Ampere's law, the MMF of the coil in Figure 20b is

$$F_m = H l_e = N i \tag{33}$$

where F_m denotes the MMF, H is the magnitude of the magnetic field, l_e is the mean length of the magnetic path, N is the number of turns in the coil and the i is the current flowing in the coil. Consequently, the magnitude of the field H can be written as

$$H = \frac{Ni}{l_e} \tag{34}$$

and insertion to Equation (28) yields the flux density in the core

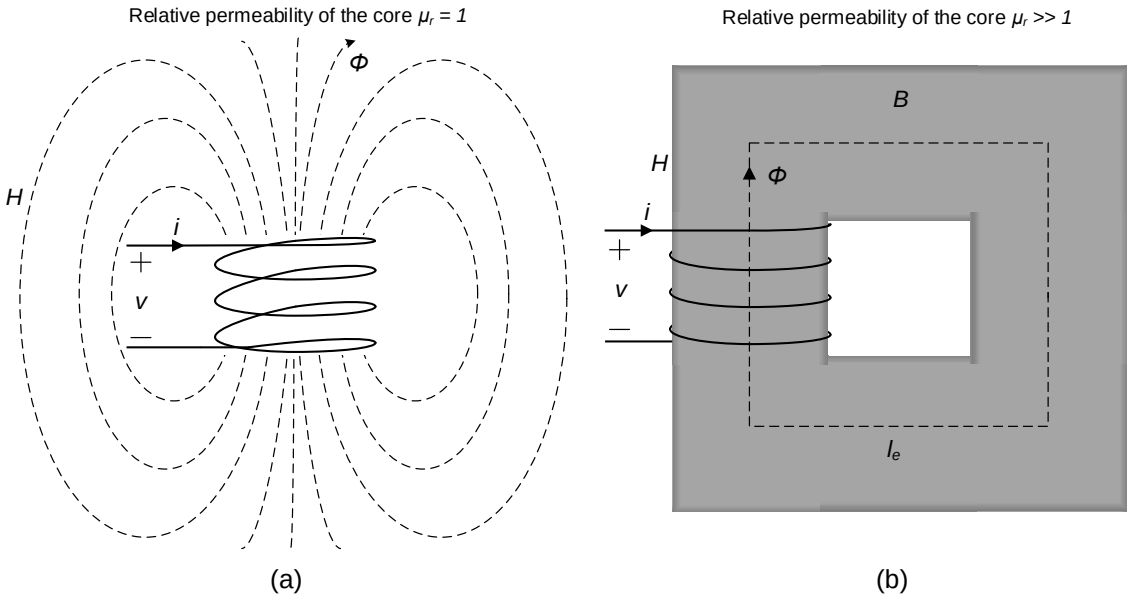

Figure 20: (a) A coil with an air core and (b) a coil spooled around a magnetic core.

$$B = \mu \frac{Ni}{l_e} \tag{35}$$

where μ is the characteristic permeability of the core.

B-H loop presents flux density B as a function of magnetic field strength H of core materials. Typical B-H characteristics of different cores are shown in Figure 21.

In Figure 21a, the slope of the air core is throughout linearly proportional to μ_0 and the B-H loop is a straight line crossing the axles of B and H at the origin. Consequently, the magnetizing path is the same as the demagnetizing path and the core has demagnetized completely when the magnetic field is zero. On the other hand, a typical B-H loop of a magnetic core is as shown in Figure 21b. From the loop, a number of characteristics can be observed. The first one is that the slope is not linear throughout as the magnetic core saturates after the magnetic field strength H exceeds H_{sat} or becomes lower than $-H_{sat}$.

As the core saturates, the strength of magnetic field H increases but the permeability of the core decreases rapidly and the operation of the core begins to resemble the operation of the air core. The reason for the decrease of permeability is the fact that the flux density B in the core cannot increase any further as it has reached the saturation point specific to the material. The effect of saturation is not permanent as the core recovers from saturation if the magnetic field decreases to a value below H_{sat}. In Figure 21b, the direction of the magnetization process is marked by arrows and the initial magnetization path, marked by the dashed line, starts from zero.

The second characteristic results from hysteresis in magnetic materials. At the point of the B-H loop where the magnetic field has decreased to zero a remanence flux is still present in the core and the corresponding flux density is denoted by B_r. The flux is completely reset to zero by a negative magnetic field denoted by coercive

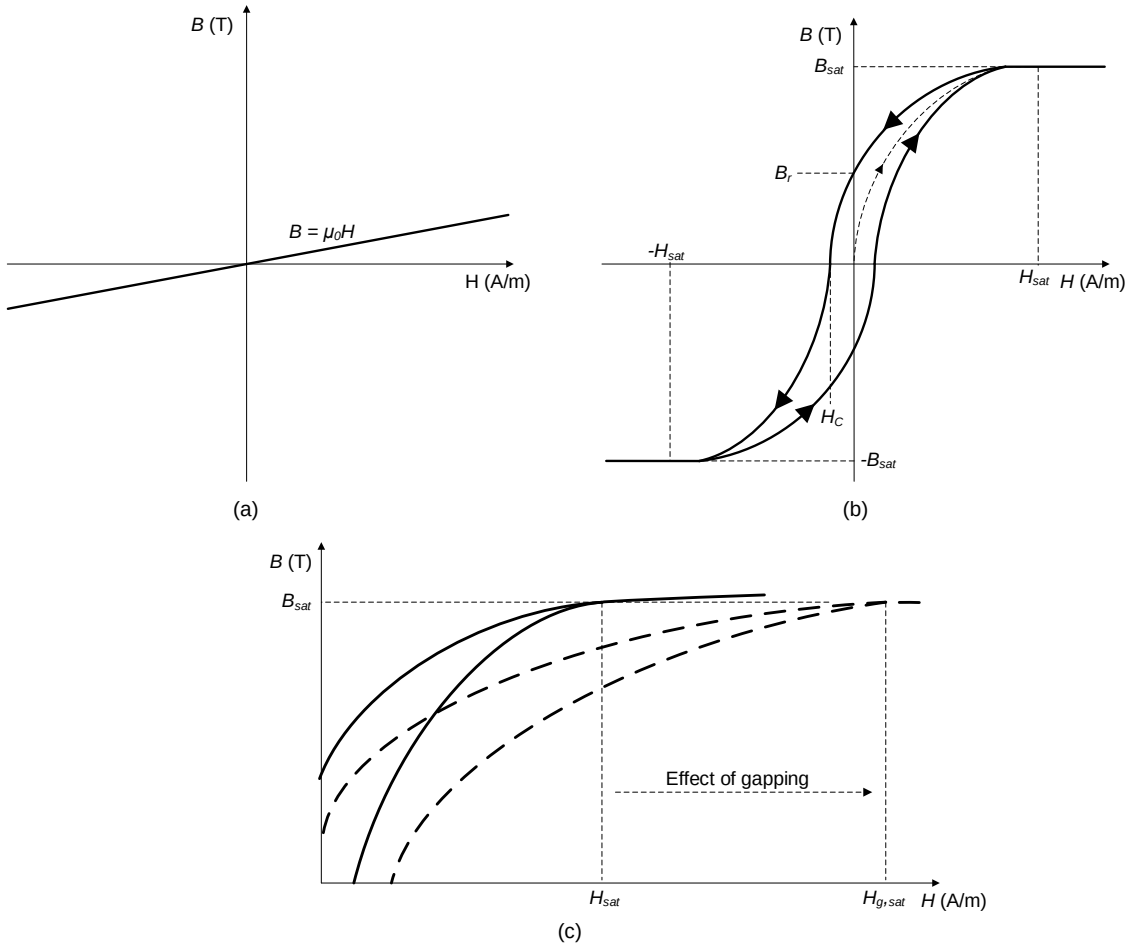

Figure 21: B-H characteristics: (a) air core, (b) a core with $\mu_r \gg 1$ and (c) effect of gapping a magnetic core.

field strength H_C. [17, p. 10.]

The third characteristic is the slope of the linear section of the B-H loop. Transformers and inductors are usually designed to operate in this area and they are not allowed to saturate under normal operating conditions. The slope of the curve depends on the characteristic permeability of the core according to Equation (28).

Air gaps are used in inductors to provide energy storage and to increase the maximum allowed magnetic field strength H_{sat}. The effect of using an air gap in a magnetic core is shown in Figure 21c. The air gap allows the core to be operated with higher field strengths if compared to an ungapped core by moving the saturation field strength H_{sat} to $H_{g,sat}$. Accordingly, gapping the core decreases the permeability of the core and therefore affects the ability of the core to resist flux. This can be noted by analyzing the analogies between electric and magnetic circuits.

Voltage source, current and resistance with electric circuits are analogous to MMF, flux and reluctance with magnetic circuits [7, p. 498]. Nevertheless, should be remembered that resistance is dissipative whereas reluctance is a lossless prop-

erty. The equation for MMF, comprising reluctance $\Re$ and flux Φ, can be found by substituting B from Equation (29) into Equation (28) and further substituting the resulting H from Equation (28) into Equation (33)

$$F_m = \frac{l_e}{\mu A_c}\Phi \tag{36}$$

where the reluctance $\Re$ is

$$\Re = \frac{l_e}{\mu A_c} \tag{37}$$

where l_e is the length of the magnetic path, μ is the permeability of the core and the A_c is the cross-sectional area of the core. By comparing the two latest equations, we can note that the MMF is

$$F_m = \Re\Phi \tag{38}$$

where $\Re$ is the reluctance and Φ is the flux.

Equation (37) shows that reluctance depends on the characteristic permeability μ. Cores with air gaps include two different permeabilities, which are the permeability of the magnetic material and the permeability of the air. Since the same flux passes through the magnetic core and the air gap, the reluctance of the core is comprised from the reluctance of the magnetic core $\Re_c$ and the reluctance of the air gap $\Re_g$. The resulting MMF of gapped cores can be written as

$$F_m = Ni = (\Re_c + \Re_g)\Phi = (\frac{l_c}{\mu A_c} + \frac{l_g}{\mu_o A_c})\Phi \tag{39}$$

where l_c is the length of the magnetic path in the core, l_g is the length of the air gap and the A_c is the cross sectional area of the leg the winding is spooled on. Since the relative permeability of a magnetic core is $\mu_r \gg 1$, the reluctance of the core is significantly smaller than the reluctance of air gap. Figure 22 shows a coil spooled around two different gapped core shapes.

A typical inductor can be made using a C core shown in Figure 22a. However, the generated EMI and noise may produce a problem as the flux fringes out of the core because of the air gap in the opposite leg. This can be decreased by locating the winding on top of the gap, which forces all the flux to pass through the coil. An example of such inductor is shown in Figure 22b. The shown ETD (economical transformer design) cores are widely used in coupled inductors, in addition to other E-shapes, because they have wide window areas around the center pole. The wide window areas are necessary to minimize the number of layers in coupled inductors having multiple windings. [18, p. 3, 5.] The full flux Φ_1 in the center pole divides between other legs of the core according to the cross sectional areas of the legs. The mean lengths of magnetic paths as well as the dimensions of cores are reported by manufacturers of cores in their datasheets.

As described in 2.2.4 flyback transformers are coupled inductors having one primary and at least one secondary winding. Typically all windings are located on top of each other on the same leg of the core. This produces best coupling between the

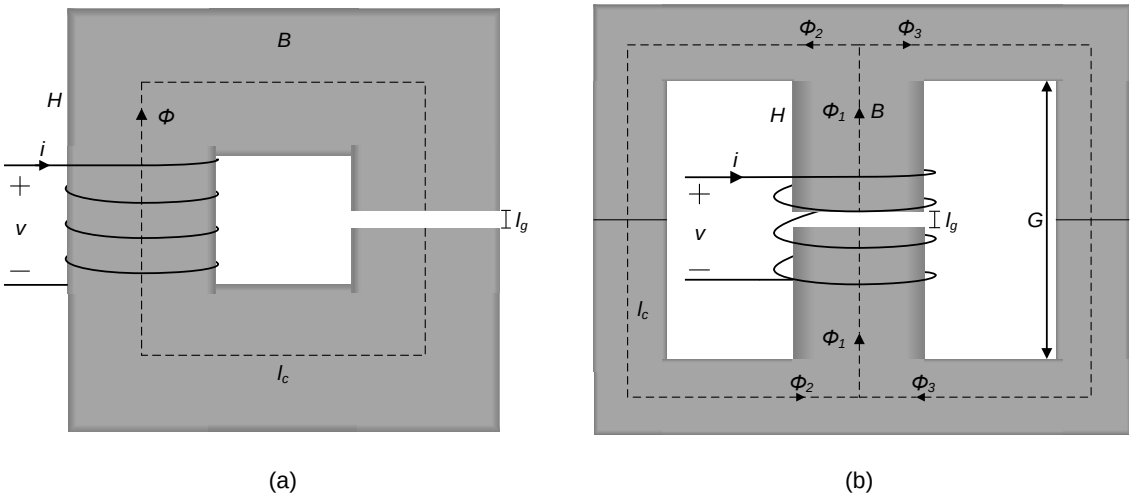

Figure 22: (a) Gapped C core and (b) gapped ETD core with the width of the window G.

different windings. Figure 23 shows a coupled inductor with a primary and a single secondary winding spooled around the center pole of an ETD core.

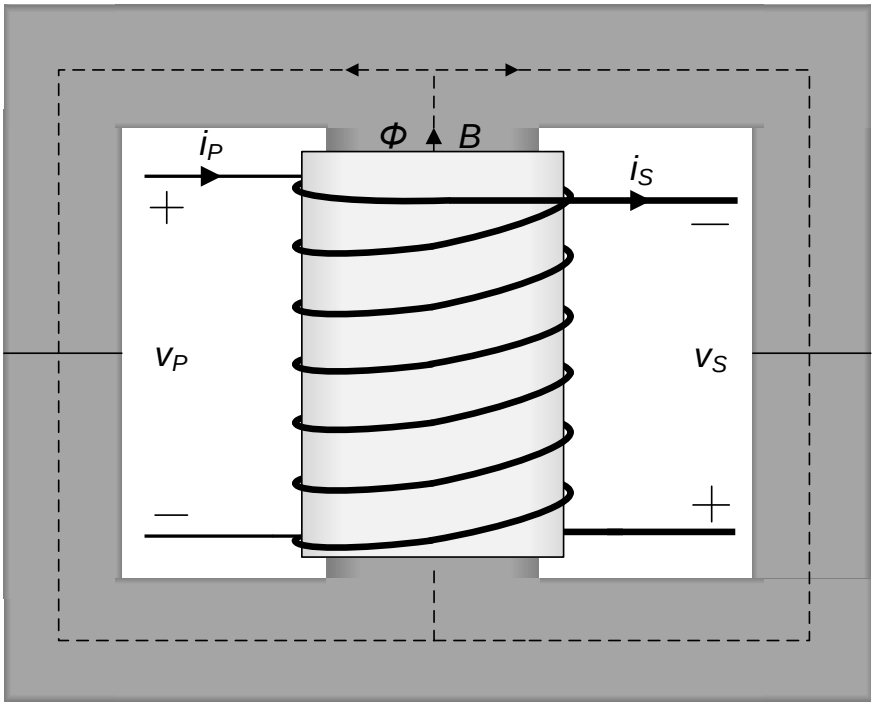

Figure 23: A coupled inductor using ETD core.

During on time, the current i_P in Figure 23 flows through the primary winding and the energy is stored in the air gap in the center pole. When the switch is turned off, the current i_S starts flowing through the secondary diode and the energy stored in the inductor is released to the output of the converter as described in 2.2.3.

Voltages and currents in the different windings can be solved by Faraday's law. Since the same flux links all windings located on the center pole of the core, voltages over windings can be stated as a voltage over one loop multiplied by the number of turns in the winding. Therefore the voltages in Figure 23 can be written as

$$\begin{aligned} v_P &= N_P \frac{\mathrm{d}\Phi}{\mathrm{d}t} \\ v_S &= N_S \frac{\mathrm{d}\Phi}{\mathrm{d}t} \end{aligned} \tag{40}$$

and if the flux is eliminated, the voltage ratio, identical to a transformer, is achieved

$$v_P = \frac{N_P}{N_S} v_S = N_{PS} v_S \tag{41}$$

where v_P is the voltage over primary, N_P is the number of turns in primary, v_S is the voltage over secondary, N_S is the number of turns in secondary and N_{PS} is the turns ratio from primary to secondary. Furthermore, currents in different windings are ideally inversely proportional to the turns ratio between primary and the secondary N_{PS}

$$i_P = \frac{1}{N_{PS}} i_S \tag{42}$$

where i_P is the current in primary and i_S is the current in secondary. [7, p. 502.]

2.3.3 Inductance

Voltage over a winding, such as the primary in Figure 23, can also be expressed by means of flux density. Since the same flux passes through all loops and voltage over one loop can be found by Equation (30), the voltage over the winding can be expressed as

$$v = N A_C \frac{\mathrm{d}B}{\mathrm{d}t} \tag{43}$$

where N is the number of turns in the winding, A_C is the cross-sectional area of the core and $\frac{\mathrm{d}B}{\mathrm{d}t}$ is the rate of change in the flux density. By inserting Equation (35) to Equation (43), the voltage over the winding becomes

$$v = \frac{\mu N^2 A_C}{l_e} \frac{\mathrm{d}i}{\mathrm{d}t} \tag{44}$$

which is of the form

$$v = \frac{N^2}{\Re} \frac{\mathrm{d}i}{\mathrm{d}t} \tag{45}$$

and since the reluctance of the core is comprised from both reluctance of the core and the reluctance of the air gap, Equation (45) can be written as

$$v = \frac{N^2}{\Re_c + \Re_g} \frac{\mathrm{d}i}{\mathrm{d}t} \tag{46}$$

where $\Re_c$ is the reluctance of the core, the $\Re_g$ is the reluctance of the air gap and $\frac{\mathrm{d}i}{\mathrm{d}t}$ is the slope of the winding current. By comparing Equation (46) to Equation (4), we can note that the inductance L of an inductor can be expressed as

$$L = \frac{N^2}{\Re_c + \Re_g} = \frac{\mu_0 A_C N^2 * 10^{-2}}{\frac{l_c}{\mu_r} + l_g} \tag{47}$$

where N is the number of turns in the winding, μ_r is the relative permeability of the core, l_c is the mean length of magnetic path in the core in cm, μ_0 is the permeability of air and l_g is the length of the air gap in cm. Equation (47) shows that increasing the length of the air gap decreases the value of inductance. On the other hand, the air gap balances the operation of the inductor as the value of inductance is not merely dependent on the permeability of the core which varies along temperature [7, p. 500].

By decreasing the inductance, the change of the current increases, which can be noted from Equation (46). Therefore, because Equation (20) states that the stored energy is dependent from the current by square law and directly from inductance, the energy stored in the inductor increases as the length of the air gap increases. Accordingly, this means that the energy of the inductor is mainly stored in the air gap. In addition, the air gap balances the operation of the inductor as the value of inductance is not merely dependent on the permeability of the core which for example varies along temperature [7, p. 500].

Some of the flux in practical transformers and coupled inductors does not link all windings. This incomplete coupling between windings leads to the practical model of the flyback transformer, where the inductance of the inductor is divided into mutual and leakage parts. The model of the flyback transformer with one secondary winding is shown in Figure 24.

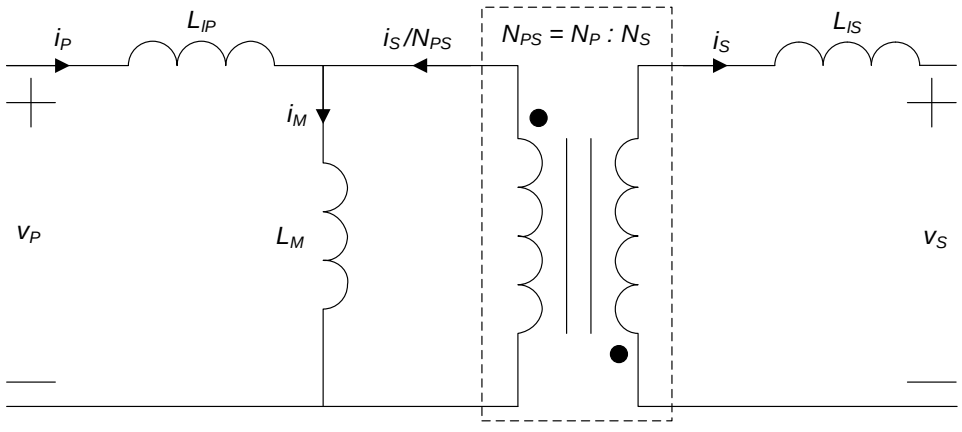

Figure 24: Model of a flyback transformer with two windings. [16, p. 26]

In Figure 24, leakage inductances L_{lP} and L_{lS} are in series to the relating windings. Furthermore, the magnetizing inductance L_M is in parallel to the primary winding and the magnetizing current i_M, flowing through L_M, is the sum of primary current i_P and secondary current i_S. During t_{off} the i_P is zero and the current in the secondary winding i_S can be calculated by

$$i_S = N_{PS} i_M = \frac{N_P}{N_S} i_M \tag{48}$$

where i_M is the current flowing through the magnetizing inductance, N_{PS} is the primary to sescondary turns ratio, N_P is the number of turns in primary winding and N_S is the number of turns in secondary winding. Therefore, the i_M of coupled inductors with n number of secondaries, can be expressed as

$$i_M = i_P + \sum_{i=1}^{n} \frac{i_{Si}}{N_{Pi}} \tag{49}$$

where N_{Pi} is the turns ratio from primary to the equivalent secondary. Moreover, self inductance L_S is the sum of the leakage L_l and the magnetizing inductances L_M related to the winding. [16, p. 25-26.]

In flyback converters, leakage inductance has the negative effects described 2.2.4 and 2.2.5. In addition, leakage inductance has effect on cross regulation between different outputs. Cross regulation means the coupling of the voltages between multiple outputs. Typically one output of a coupled inductor is regulated and the voltages of other windings vary depending on the coupling between the secondaries. As a consequence, the coupling between different outputs should by minimized in order to reduce the cross regulation. Conversely, the leakage inductance relating to the primary should be minimized to achieve best coupling between the primary and the secondaries. [20] The leakage inductance caused by bowing of the windings can be minimized by using a core with a round center pole. This ensures the most compact design of the windings. [17, p. 138.]

Due to the presence of an air gap in inductors, the flux in the air gap fringes outside the air gap. The fringing effect near an air gap is shown in Figure 25. In Figure 25 the winding is spooled on top of a coil former. Fringing flux induces eddy currents to the windings near the gap which causes localized heating of the component. [17, p. 23-24.] The effect of fringing flux to the copper losses has been studied and the fringing flux will increase the current density in the wires because of the induced eddy currents [21].

The fringing flux reduces the effective length of the air gap decreasing the reluctance of the inductor. According to Equation (47) the inductance of the inductor increases as the reluctance decreases. The effect of fringing flux to the inductance can be approximated by fringing flux factor F

$$F = \left(1 + \frac{l_g}{\sqrt{A_C}} \ln \frac{2G}{l_g}\right) \tag{50}$$

where l_g is the length of the air gap, A_C is the cross sectional area of the core and G

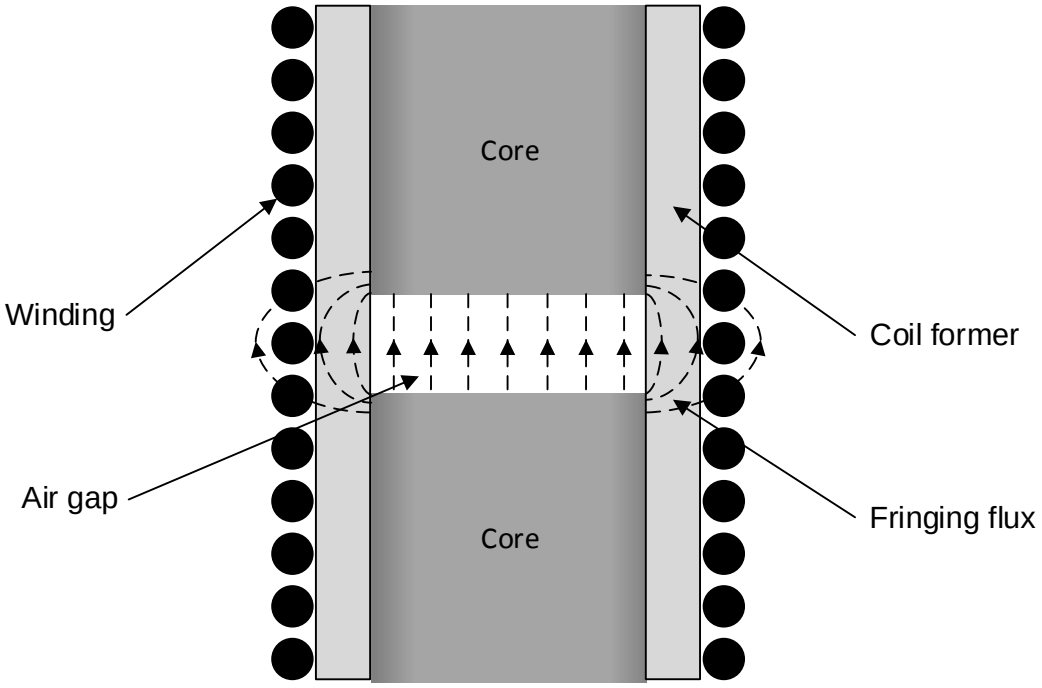

Figure 25: Fringing flux near an air gap. [17, p. 26]

is the width of the window. [17, p. 25.] The correct value of magnetizing inductance L_M, taking into account the fringing, can be calculated by

$$L_M = FL \tag{51}$$

2.3.4 Core size and material

The needed size and shape of the core can be approximated if the output power of the flyback converter is known. Manufacturers of cores have typically tables and graphs for selecting the initial size and shape. For a given power output, the suitable cores from Ferroxcube are presented in Table 1.

Listings, such as Table 1, give an initial idea of usable sizes of different cores. In addition, manufacturers typically have graphs for selecting a core and an air gap for a given stored energy. After the required energy has been calculated, the size of the core can be selected from the graph provided by manufacturers. An example graph for ETD shapes is shown in Figure 26. In Figure 26 the maximum stored energy is plotted as function of air gap length for different sizes of ETD cores. Moreover, the required amount of energy, over one switching period, is determined by Equation (20).

In the literature, several methods have been proposed for approximating the required size of the core for transformers [7], [16], [17], [18]. The method for coupled inductors produces a parameter K_g for selecting the required size of a ferrite core. The parameter is given by the geometry of the core

Table 1: Power throughput for different types of cores at 100 kHz switching frequency. [19, p. 29]

POWER RANGE (W)	**CORE TYPE**
< 5	RM4; P11/7; T14; EF13; U10
5 to 10	RM5; P14/8
10 to 20	RM6; E20; P18/11; T23; U15; EFD15
20 to 50	RM8; P22/13; U20; RM10; ETD29; E25; T26/10; EFD20
50 to 100	ETD29; ETD34; EC35; EC41; RM12; P30/19; T26/20; EFD25
100 to 200	ETD34; ETD39; ETD44; EC41; EC52; RM14; P36/22; E30; T58; U25; U30; E42; EFD30
200 to 500	ETD44; ETD 49; E55; EC52; E42; P42/29; U67
> 500	E65; EC70; U93; U100; P66/56; PM87; PM114; T140

$$K_g \geq \frac{A_C^2 W_A}{(MLT)} \tag{52}$$

where A_C is the cross-sectional area of the core, W_A is the area of the window and MLT is the mean length of a turn. On the other hand, the size of the core can be stated to be a function of design specifications

$$K_g \geq \frac{\rho_c L_M^2 i_{tot}^2 i_{M,max}^2}{B_{max}^2 P_{Cu0} K_u} 10^{10} \tag{53}$$

where ρ_c is the effective resistivity of copper, L_M is the desired magnetizing inductance, i_{tot} is the sum of rms currents in all windings referred to primary, $i_{M,max}$ is the peak value of magnetizing current, B_{max} is the maximum allowed flux density in the core, P_{Cu0} is the value of allowed ohmic copper losses and K_u is the filling factor of the window. The resistivity of copper is 1.724*10^{-8} Ω-cm at the temperature of 25°C and 2.3*10^{-8} Ω-cm at 100°C. [7, p. 550-553.] The allowed copper losses P_{Cu} are approximated according to the allowable thermal rise of the component.

The filling factor K_u means the percentual area of the window occupied by copper. The rest of the window has to be reserved for coil former, safety margins, wrapper insulation, layer insulation, wire insulation and the fill factor of the wire. The value of K_u is usually less than 0.3 depending on the chosen wire type. [17, p. 132, 142.]

The rms values of winding currents can be calculated similarly as the rms values of triangular waveforms

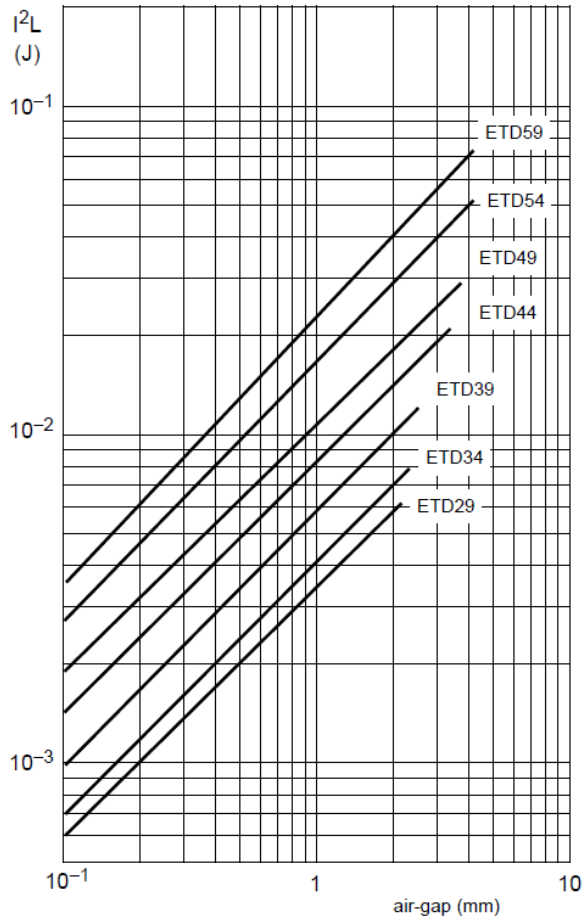

Figure 26: Ferroxcube: I^2L graph for selecting size from ETD cores. [19, p. 35]

$$i_{i,rms} = i_{ipk}\sqrt{\frac{D}{3}} \tag{54}$$

where i_{ipk} is the peak value of the current in the winding and D is the duty ratio leading to the peak value. The sum of rms currents i_{tot} is calculated with respect to primary winding

$$i_{tot} = i_{P,rms} + \frac{N_2}{N_P} i_{S1,rms} \ldots + \frac{N_n}{N_P} i_{n,rms} \tag{55}$$

where $i_{P,rms}$, $i_{S1,rms}$ and $i_{n,rms}$ are the rms values of currents in the primary, the first secondary and the secondary number n. In addition, the currents in Equation (55) are multiplied by the equivalent turns ratios from each winding to primary. [7, p. 557-558.]

When the parameter K_g has been calculated with Equation (53), the size of the core can be selected from Table 2. In Table 2 the d_{cp} is the diameter of the center pole. The parameter K_g of the selected size in Table 2 should be greater than the value calculated by Equation (53). This helps fitting the windings, producing the

copper losses P_{Cu}, to the window of the core and that a practical air gap can be realized to avoid premature saturation.

Table 2: Geometrical constants of different of ETD cores. [7, p. 866.], [19, p. 541,545,551,554.]

Core type	K_g (cm^5)	A_C (cm^2)	W_A (cm^2)	d_{cp} (cm)	G (cm)	l_c (cm)
ETD29	0.0978	0.76	0.903	0.98	2.2	7.20
ETD34	0.193	0.97	1.23	1.11	2.36	7.86
ETD39	0.397	1.25	1.74	1.28	2.84	9.22
ETD44	0.846	1.74	2.13	1.52	3.22	10.3

Mn-Zn (Manganese-Zinc) ferrite is a widely used material in the cores of flyback transformers. Due to the low power loss density with typical flux densities and switching frequencies around 100 kHz, many Mn-Zn materials are suitable for power transformer applications including flyback transformers [19, p. 19]. Other important parameters of magnetic materials are for example the BH characteristics, the amplitude permeability μ_a and Curie temperature T_C. The saturation flux density B_{sat} of the material can be checked from the BH loop or the amplitude permeability curve provided by the manufacturers. The curie temperature expresses the temperature at which the magnetic properties of the core will cease to exist. Hence, the curie temperature of the material should never be reached during normal operation.

A cross-reference listing of Mn-Zn materials presenting complementary materials between manufacturers is shown in Figure 27. From the listing in Figure 27, the correspondence of different materials can be noticed between the manufacturers. Ferroxcube states that materials 3C30 and 3C34 are suitable for line output transformers and flyback converters operated with switching frequencies up to 200 kHz and 300 kHz respectively. In addition, materials 3C90 and 3C94 are suitable for general industrial use with the same corresponding switching frequency ranges. [19, p. 29.] The listing in Figure 27 shows that for example Asian manufacturers TDG and DMEGC have equivalent materials to 3C30, 3C34, 3C90 and 3C94 from the European Ferroxcube.

Listings, such as Figure 27, should not be trusted exclusively. Instead, the operation and parameters of the materials are to be verified from the datasheets provided by the manufacturers of the materials and by verifying the operation of the components. The datasheets of Mn-Zn ferrite material 3C30 from Ferroxcube and the equivalent materials from DMEGC and TDG can be found out from Appendix B.

In addition to ferrites, powdered materials are sometimes used in flyback transformers operated with high DC flux density. The advantage of the powdered cores against typical ferrites is that the air gap is distributed evenly into the core instead of discrete air gaps. As a result, the external field near the air gap will be diminished. The disadvantage limiting the usage of powdered cores is the higher power loss if compared to ferrites. [18, p. 5.]

mainland China	东磁（DMEGC）	DMR30	DMR40	DMR44	DMR47	DMR24	DMR28	DMR90	DMR95
	TDG	TP3	TP4	TP4A	TP4D	TP4E/TPB15		TP4E/TPB15	TP4W/TPW33
	FENGHUA	PG252	PG232	PG242				PG182A	PG312
Japan	TDK	PC30/PC32	PC40	PC44	PC47			PC90	PC95
	NICERA	NC-1M	NC-2H	2H-M4/2H-M5		BM30/BM40		BM27/BM29	3H
	FDK(FUJI)	6H10	6H10/6H20	6H40/6H41					6H60
	HITACHI		ML24D	ML25D		MB28D		MB19D	ML30D/ML32D
	NEC-TOKIN		BH2	BH1		BH3	BH7		
	JFE	MB1	MB3	MB4		MB1H			MBT1
	TOMITA	2E6	2G8	2E8		2N6			
Europe	FERROXCUBE		3C30&3C34&3C90	3C94		3C92		3C96	3C95
	EPCOS	N41	N67, N72	N87, N97		N92			N95

Figure 27: Cross-reference list of Mn-Zn ferrite materials. [22]

2.3.5 Winding turns and wires

The minimum number of turns in a primary winding can be determined by modifying Equation (43) to the following form

$$N_P = \frac{v_D t_{on}}{B_{max} A_C} \tag{56}$$

where t_{on} is on-time of the MOSFET, v_D is the input voltage applied to the primary, B_{max} is the maximum allowed flux density swing of the core material and A_C is the cross-sectional area of the selected core. From Equation (56) we can note that choosing a higher number of turns than calculated leads to a lower flux density. Alternatively if the number of turns is chosen to be less than calculated, the maximum flux density will be exceeded. In addition, the chosen value should be integer.

In order to realize the desired turns ratio N_{PS}, the number of turns in the secondaries is calculated by

$$N_S = \frac{N_P}{N_{PS}} \tag{57}$$

where N_S is chosen to be an integer.

To minimize the copper losses P_{Cu} the area of the window W_A should be allocated to each winding according to their rms currents. Therefore, a fraction of the window is calculated according to

$$\alpha_i = \frac{N_i i_{i,rms}}{N_P i_{tot}} \tag{58}$$

where α_i is the fraction allocated to the winding, N_i is the number of turns in the winding, $i_{i,rms}$ is the rms value of the current in the winding and i_{tot} is the sum of rms currents of all windings. [7, p. 547-548.]

The copper area of each winding wire A_{wi} can then be calculated by

$$A_{wi} \leq \frac{\alpha_i K_u W_A}{N_i} \tag{59}$$

where K_u is the filling factor of the window, W_a is the area of the window and N_i is the number of turns in the winding.

The diameter of the round wire d_{wi} can be calculated from the wire area by approximating the area of the conductor with the area of circle

$$d_{wi} = 2\sqrt{\frac{A_{wi}}{\pi}} \tag{60}$$

If multiple parallel conductors are used, the diameter of conductors can be found by equating the area A_{wi} and the area of parallel strands $A_{wi,p}$ equal

$$\begin{aligned} A_{wi} &= A_{wi,p} \\ p_i \pi \left(\frac{d_{wi,p}}{2}\right)^2 &= \pi \left(\frac{d_{wi}}{2}\right)^2 \end{aligned} \tag{61}$$

and solving the diameter

$$d_{wi,p} = \frac{d_{wi}}{\sqrt{p_i}} \tag{62}$$

where $d_{wi,p}$ is the diameter of a single strand of p_i parallel conductors.

Litz wire consists of multiple parallel and individually insulated strands twisted together. If Litz wire is used, the diameter of a single strand should be smaller than calculated by Equation (62) because the fill factor of multiple, individually insulated and twisted, strands is worse than that of the single conductor [16, p. 146].

The current density in the windings can be calculated by

$$J = \frac{i_{i,rms}}{A_{wi}} \tag{63}$$

where $i_{i,rms}$ is the rms value of the winding current and A_{wi} is the copper area of the winding. A typical value of the maximum current density is 5 A/mm^2 in the copper wire used in the magnetics of power electronics [26].

2.3.6 Losses and thermal rise

Losses are produced both in the core and in the windings of the flyback transformer. The core loss P_{Fe} of ferrites can be divided into two importants parts, hysteresis loss and eddy current loss. Hysteresis loss of the ferrite core depends on the peak flux swing of the B-H loop. The energy lost during one cycle is the volume of the core multiplied by the area of the B-H loop. The hysteresis power loss is obtained if the lost energy during one switching cycle is multiplied by the switching frequency. [7, p. 506.] Alternatively, losses are generated by fast changing magnetic fields in

semiconducting ferrite cores. The magnetic fields induce eddy currents to the core which produces losses in the resistance of the core material. Furthermore, eddy current losses are dependent from frequency by second power. [25]

Core losses are approximated from the graphs in the datasheets presenting the core loss density as a function of peak ac flux density. The core loss density graph of the ferrite material 3C30 from Ferroxcube is presented in the bottom right of Figure B1 in Appendix B. From the graph, the core loss density of the ferrite material can be examined with the given operating frequencies. Thereafter, the density is multiplied by the effective volume V_e of the selected core to obtain the core loss P_{Fe}.

Copper losses of windings P_{Cu} is the sum of ohmic and AC losses. Ohmic losses are determined according to

$$P_{Cu0} = \sum_{i}^{n} R_{0i} i_{i,rms}^2 \tag{64}$$

where R_{0i} is the ohmic resistance of the wire and $i_{i,rms}$ is the rms value of the current in the winding. The ohmic resistance R_{0i} of the winding can be calculated by

$$R_{0i} = \rho_c \frac{4(MLT_i)N}{p_i * \pi d_{wi,p}^2} \tag{65}$$

where ρ_c is the effective resistivity of copper, MLT_i is the mean length per turn, N is the number of turns in the winding, p_i is the number of strands and $d_{wi,p}$ is the diameter of one strand. [16, p. 42.]

The part of AC losses in flyback transformers is significant because of the typical switching frequencies in the range of 40kHz to several MHz. The triangluar winding current is the sum of harmonics of the switching frequency. Therefore, the AC loss is defined by

$$P_{Cu,ac} = F_R P_{Cu0} \tag{66}$$

where F_R is the ac-to-dc resistance ratio which takes into account the harmonics in the current. F_R includes the skin effect and the proximity effects of adjacent layers and the fringing flux. [26]

Skin effect means that rapidly changing current in a conductor induces a flux that induces eddy currents to the conductor opposing the main current in the center of the conductor. Conversely, the induced eddy currents increase the current density in the outer surface of the conductor. This leads to a penetration depth where the current flows in a conductor. The penetration depth in a copper conductor can be expressed as

$$\delta = \sqrt{\frac{2\rho_c}{\omega\mu}} = \sqrt{\frac{\rho_c}{\pi f \mu_0}} \tag{67}$$

where ρ_c is the resistivity of copper, ω is the angular frequency, f is the frequency of the current and μ is the permeability of the material which is roughly the same as the permeability of vacuum μ_0 [27].

The proximity of the air gap has significant effect to the resistance of the windings closest to the air gap. The effects of the induced eddy currents depend on the magnetomotive force, operating frequency, length of the air gap and the distance between the gapped leg and the layer of the winding. [21] Windings in inductors experience an increased power loss caused by the proximity effect of adjacent layers. In the proximity effect, layers of windings induce flux to the spaces between the adjacent layers. This opposing flux increases the AC resistance of windings by inducing eddy currents to the surfaces of the conductors in the adjacent layers. [7, p. 510–511.]

The effects of eddy currents in conductors can be reduced by using multiple parallel conductors or bunched wires, such as Litz wire, instead of a single conductor [28]. The diameters of strands are calculated for example according to the penetration depth at a certain frequency. In addition, the number of parallel strands is defined from Equation (62) to match the equivalent area and diameter of the single conductor specified by Equation (59) and Equation (60).

Losses contribute to the efficiency and the temperature rise of the component. Typically the amount of allowed losses is determined according to the allowed temperature rise. The maximum thermal rise and fluctuations in the operating temperature are known to affect the life cycle of the component. Accordingly, the higher the temperature rise and fluctuations, the shorter the life cylce. The operating temperature of the component is the sum of ambient temperature and the temperature rise of the component [16, p. 253].

The three heat transfer mechanisms are conduction, convection and radiation. All mechanisms are dependent on the material and the surface area of the component. If the allowed temperature rise ΔT and the total surface of the component are known, the power losses in the component can be approximated with an empirical equation

$$P_{loss} = (\Delta T)^{1.1} A \tag{68}$$

where ΔT is the difference between the hot spot and the ambient temperatures and A is the total surface of the component. Equation (68) yields an accuracy of around ten percent and it can be used to predict the dependence of the different core sizes from the allowed losses. Alternatively, methods separating the effects of the heat transfer mechanisms and using the lumped thermal resistances of the structure should be used with applications requiring better accuracy. [16, p. 256-276.]

2.3.7 Structure

The arrangement of the windings to the window of the core has an effect on the resistance, the leakage inductance and the produced EMI of the flyback transformer. The ohmic resistance is dependent on the length of the winding according to Equation (65). Winding with the highest voltage should be located closest to the core and be connected to the drain pin of the MOSFET. This minimizes the ohmic resistance of the winding and enables a shielding effect of other windings decreasing the radiated EMI. [29]

On the other hand, the amount of AC losses resulting from fringing flux near the air gap is significant in flyback transformers. In order to reduce the effect of fringing flux on the windings closest to the gap, the windings should not be located directly on top of the core. The higher the length of the air gap, the higher distance should be kept to the gap. Nevertheless, typically windings are spooled on coil formers providing greater than 0.5 mm distance to the gap depending on the size of the coil former. This distance does not minimize the effect of fringing flux to the AC resistance but is usually the practical choice if multiple windings are needed to be fitted to the window of the core. [21]

The winding order has an affect to the leakage inductances and therefore, to the coupling between windings. If the primary should be closest to the core, as described above, the secondary winding, conducting the highest current, should be on top of the primary. This maximizes the energy transfer between windings as the leakage inductance is proportional to the distance between the windings. If the primary consists of multiple layers, interleaving the secondaries between the layers of the primary decreases the leakage inductance approximately by half. Moreover, the total leakage inductance of the component should be minimized because leakage energy between any of primary to secondary combinations has an effect on the efficiency of the converter. [21]

Different layers should be spread to the entire allowed width to maintain the good coupling. Therefore, coil formers with separate sections next to each other should be avoided with flyback transformers. [30] A method for spreading a layer with only a couple of turns is to use parallel wires having equal wire area to the original single wire. An interleaved transformer design and the usage of parallel wires is presented in Figure 28.

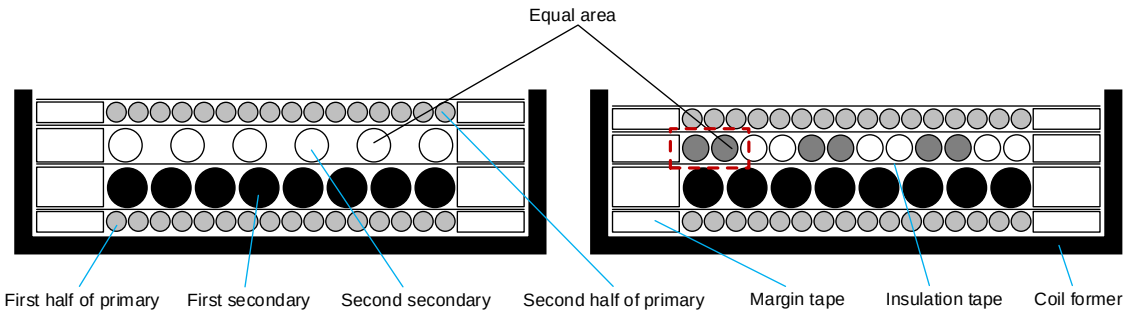

Figure 28: Cross sections of a coil former with interleaved primary and two secondaries. Second secondary winding using single wire on the left and using two parallel wires on the right.

Figure 28 presents a construction with margins where the required creepage distance is produced by margin tape barriers in the sides of coil former. Different layers and the outer half of the primary are insulated by tape. The construction on the right in Figure 28 uses two parallel wires next to each other in the second secondary. Wire areas of all windings are equal in both constructions. As can be noted from

Figure 28, using parallel wires leads to a more compact design of the windings and thus, the leakage inductance of the transformer is reduced.

2.3.8 Manufacturing process

In order to design effectively manufacturable flyback transformers, the designer should be aware of the typical manufacturing process of the component. Following information is based on the description of a contract manufacturer of magnetic components.

Magnetic components are manufactured according to the specifications of a customer. The contract manufacturers may have preferences for the suppliers of different parts. Due to higher volumes, the parts from the preferred suppliers are usually cheaper or their lead times are shorter than those from other suppliers.

Windings are typically constructed using coil formers. In the winding operation, the coil former is attached to the rotating shaft of a spooling machine. The machine rotates the coil former as the specified winding wire is guided to the coil former. The correct number of turns is ensured by entering the specified number of turns to the spooling machine. Furthermore, the specified number of insulation tape layers between winding layers are ensured by the corresponding number of rotations. Depending on the component, layers comprised of approximately six turns or less are done as handwork. In addition, margin tapes, fixing the wires to pins of coil formers and other special constructions are made by hand. The winding construction begins from the bare coil former and ends to the outermost winding and wrapper insulation layer.

After the winding operation, the pins of coil formers are dipped into the solder pot for a very short period of time to prevent melting of the coil former. After the soldering, the core halves are attached upon the spooled coil former and fixed together by glueing or by using mounting clips. If varnishing is specified, the component will be dipped to lacquer. Varnishing of magnetic components is usually done to further enhance the insulation, to enhance conduction of heat from windings to core, to reduce noise generated by the component or to protect the component from the possible pollution of the environment. Finally, the specified electrical and insulation tests are conducted on the complete component to verify the specified functioning.

This chapter has presented the magnetic theory, the most important parameters and the notable issues to design flyback transformers. In the following chapter, flyback transformers are designed for two different flyback converters according to the theory presented in the previous chapters.

3 Design of flyback transformer

In this chapter, flyback transformers are designed for one DC-to-DC and one AC-to-DC flyback converter. The iterative design process is based on the theory presented in the previous chapters.

The design process begins with determining the initial values and preferences of the designs. This is followed by determining the parameters of the components such as turns ratios, inductances, numbers of turns and allowed thermal rise. Then, materials and the structure of the designs are decided based on the determined parameters and the preferences. The design process ends with analyzing the costs of the different designs. All calculations are presented in Appendix C excluding straightforward parameters, which are determined directly in the text.

3.1 Initial values and design preferences

The initial values are determined from the specification of the auxiliary power supply. Moreover, the auxiliary power supply has two independent flyback converters. The double ended topology presented in 2.2.5 is used in the DC-to-DC converter and the designs of this converter will be marked as DCDC from now on. The single switch topology presented in 2.2.4 is used in the AC-to-DC converter and the designs of this converter will be marked as ACDC. The input and output voltages and the power demands of the two converters are listed in Table 3.

Table 3: Voltages and power demands of the converters.

Converter	V_D (V)	V_{O1} (V)	V_{O2} (V)	I_{O1} (A)	I_{O2} (A)	P_O (W)
DCDC	240–1100	24 ± 5%	24 ± 10%	1.8	1.2	72
ACDC	390–806	24 ± 5%	24 ± 10%	0.41	0.45	21

In Table 3 the input voltage V_D of the AC-to-DC converter is assumed to be completely smoothened by the input filter capacitor and the power demand of the load P_O is simply the sum of the both output powers. Fruthermore, the output voltage V_{O1} is regulated in both converters and has tighter tolerance than V_{O2}. Moreover, the output V_O2 is considered as user potential, which means that user has access to this potential.

The used controller circuit is the QR type UCC28600 from Texas instruments. The operation of the circuit is described in 2.2.6 and the relating specifications needed in designing the flyback transformer are summarized in Table 4.

Table 4: Specifications of UCC28600 controller circuitry to design flyback transformers.

f_{sw} (kHz)	v_{CC} (V)	v_{FCC} (V)	v_{AUX} (V)
40–130	15.3–21	0.8	16.1–21.8

In Table 4, the v_{FCC} is the forward voltage drop of the used diode and it is added to v_{CC} to obtain the voltage in the auxiliary winding v_{AUX}.

The maximum voltage stress over the secondary diodes is 300 V for the DC-to-DC converter and 600 V for the AC-to-DC converter and the maximum DC currents are correspondingly 15 A and 3 A. Furthermore, the forward voltge drop v_F of both diodes is 1 V.

Specifications of the MOSFET, used in the converters, are presented in Table 5.

Table 5: Specifications of the used MOSFET. [31]

v_{rating} (V)	i_{rating} (A)	$R_{DS,on}$ (Ω)	c_{DS} (pF)
1500 V	2.5	6	100

In Table 5, the resistance during on time is $R_{DS,on}$, the v_{rating} is the maximum rated voltage stress and the i_{rating} is the maximum rated current of the MOSFET.

Some properties of the converters are fixed, including the pin orders of the flyback transformers on the PCB (printed circuit board). This delimits the usage of possible cores, as suitable coil formers are not available for all shapes. Furthermore, the minimization of leakage inductance is desirable because of the already existing voltage snubbers. For these reasons, ETD cores are chosen to be used in the designs.

The values of toughest operating point, minimum input voltage and the maximum load current, are used to calculate the parameters. Moreover, the maximum ambient temperature of the auxiliary power supply is 65 °C in the final application and 100°C will be used as the operating temperature when calculating the temperature dependent parameters.

The focus of the designs will be reliable operation in all operating points and cost effectivity. Clearances and creepages are determined according to the safety standard as described in 2.1.4 and the thermal rise of the component is limited below the maximum temperatures of used materials. Moreover, the cost effectivity is taken into account by using TIW only in windings requiring reinforced insulation, by selecting chinese suppliers for cores and avoiding complex structures to minimize the time used for manufacturing. Choosing the suppliers for wires and coil formers is left for the contract manufacturer because they usually have preferences for the local least expensive suppliers.

3.2 Turns ratio and inductance

The turns ratio N_{PS} of the ACDC design is chosen according to the maximum voltage stress of the MOSFET by Equation (17) and by using a value of $v_{spike} = 0.3 * V_D$. A safety margin of 30 % of the V_D has to be left to the maximum rated voltage of the MOSFET because the actual value of the voltage spike v_{spike} is not known [9, p. 130]. Contrary to ACDC designs, in the double ended DCDC design, the turns ratio will be decided according to the maximum achievable duty cycle of a QR controlled flyback as described in 2.2.6. This is because the input voltage range is as wide as 240-1100 V. Due to the wide range, the duty cycle D_{max} is needed to be as high as possible, to maximize the on time with the maximum input voltage, to make sure the MOSFET will turn on completely.

The maximum duty cycle of the MOSFET D_{max} is $1 - D_{off}$, where D_{off} is 0.5 in BCM. In the QR mode, the D_{res} is initially 0.04, which should be additionally subtracted from the maximum duty cycle as described in 2.2.6. Therefore, D_{max} is chosen to be 0.44. The D_{max} is chosen 0.01 lower than theoretical maximum to ensure that the converter does not enter to the continuous region. The value of D_{res} is achieved by assuming that t_{res} is initially 500 ns [1].

In addition, 45 kHz will be used as the initial value of switching frequency in the calculations of DCDC designs. This frequency is chosen according to the existing converter design, in which for example EMI filters are optimized on the ground of this operating point. Conversely, the switching frequency of the ACDC design will be 100kHz.

The voltage drop due to the resistance of the primary R_P and $R_{DS,on}$ is unknown in the beginning, because the rms value of the primary current is unknown. Therefore, the calculation of the inductance L will be iterated twice by first neglecting the v_{drop} and calculating the inductance and the peak current of primary winding. Then, the rms value of the current is calculated from the peak value using Equation (54) and an approximation of the voltage drop is attained by $v_{drop} = (R_{DS,on} + R) i_{p,rms}$ [7, p. 807-808]. The calculated value approaches the actual v_{drop} as the number of iterations increase. In addition, the resistance of the primary winding R is approximated to be 1 Ω in the calculation.

The initially calculated values are presented in Table 6.

Table 6: Calculated N_{PS}, L, D_{max}, i_{Ppk}, $i_{P,rms}$ and v_{drop}.

Design	N_{PS}	L (mH)	D_{max}	i_{Ppk} (A)	$i_{P,rms}$ (A)	v_{drop} (V)
DCDC	7.86	1.49	0.43	1.50	0.57	7
ACDC	8.42	2.79	0.29	0.38	0.12	0.84

Because the approximated v_{drop} of the ACDC design, shown in Table 6, is only less than 1 V, it is neglected in the calculations.

3.3 Core size and flux density

The material and the size of the core are initially selected from Table 1. Table 1 presents the suggested sizes and shapes of cores for the switching frequency of 100 kHz. However, the parameters for DCDC design in Table 6 were calculated with 45 kHz as the operating frequency which should be noticed when selecting the size of the core. The lower operating frequency means that higher energy is stored to the air gap during one switching cycle. From Table 6, ETD34 is chosen for DC-to-DC converter and ETD29 is chosen for AC-to-DC converter according to the output power demands of the converters.

The stored energy per one switching cycle and the maximum stored energy of the selected cores are shown in Table 7. In Table 7, the maximum throughput of the cores E_{max} is determined from Figure 26 with maximum lengths of air gaps set to 10 percent of d_{cp} in Table 2. The energies E in Table 7 have been calculated in Appendix C for both converters and they appear to be less than the maximum energies E_{max}

of the cores. To be noted from Table 7, the ETD29 seems to be marginally suitable for the DCDC design because the energy of DCDC design $E = 3.36$ mJ is less than $E_{max} = 3.4$ mJ.

Table 7: Initially calculated energy per one switching cycle, the maximum energy throughput of the selected cores and the used maximum lengths of air gaps.

Design	E (mJ)	E_{max} (mJ)	l_g (mm)
DCDC34	3.36	4.2	1.11
ACDC29	0.53	3.4	0.98

As a result, an alternative size of the DCDC will be designed using the size ETD29 and the different designs will be marked as DCDC29, DCDC34 and ACDC29 according to the size of the selected core.

Equivalent materials to 3C30, Mn-Zn ferrite from Ferroxcube, were chosen to be used in both designs because the material is intended for flyback transformers operated with frequencies less than 200 kHz as described in 2.3.4. The Chinese manufacturers DMEGC and TDG provide materials with properties close to 3C30 and they are chosen as the two suppliers of the cores. The properties of the materials, typically needed in design process, are collected to Table 8 from Figure B1, Figure B2 and Figure B3.

Table 8: Collected properties of materials 3C30, DMR40 and TP4.

Material	T_C (C)	μ_i	B_{sat} (mT)	P_V (mW/cm^3)
3C30	>220	2100 ±20%	440	440
DMR40	>215	2300 ±20%	400	410
TP4	>220	2300 ±25%	390	410

In Table 8, the μi is the initial permeability, which is the permeability of the core with a low field strength and the value is typically reported by manufacturers in the datasheets.

If the properties of Table 8 are compared to each other, the similarities between the different materials can be noticed. The value of B_{sat} in Table 8 is the reported value in 100 °C and the power loss density P_V is the value with 200 mT peak ac flux density and 100 kHz operating frequency. Moreover, the peak ac flux density in DCM is half of the peak to peak flux density swing ΔB [18].

The value of the ΔB should be chosen less than B_{sat} to avoid saturating the core with the minimum input voltage. For ferrites, such as the materials selected, a typically used value for ΔB is 0.25-0.30 T [18]. The desired value of the flux density swing ΔB is initially selected to be 0.25 T. The lower operating flux density leads to lower core losses as can be seen from the graph on the left in Figure B1.

3.4 Numbers of turns, air gap and peak current

In order to achieve the flux density swing of 0.25 T, the minimum number of turns will be calculated with Equation (56). The correct length of air gap l_g is chosen by

iterating Equation (51) with different air gap lengths l_g until the calculated L_M is close to the desired value of inductance in Table 6.

The minimum number of turns for the DCDC34 is 91.6. Hence, the selected number of turns is 92. Moreover, the minimum calculated number of turns for DCDC29 is 116.2 but the chosen number of turns will be the same 92 to maintain simple comparison between the different sizes. This results in an increased flux density swing to approximately 0.32 T but because the chosen value of inductance is less than that calculated initially, the peak value of flux swing will be closer to 0.28 T. Furthermore, the increased flux density increases the core losses but is not high enough to saturate the core.

The number of turns in the secondaries of the DCDC34 and DCDC29 is determined according to Equation (57). If the chosen number of turns in primary $N_P = 92$ is divided by the turns ratio $N_{PS} = 7.86$, the number of turns in the secondaries is $N_S = \frac{N_P}{N_{PS}} \approx 11.7$. Therefore, the turns in the secondaries is selected to be 12, which results in the turns ratio $N_{PS} = \frac{92}{12} \approx 7.67$.

The minimum allowed air gap length is chosen to be 0.3 mm due to practical tolerances in the grinding of the gaps and the minimum calculated number of turns for the ACDC design is 57.1 turns. However, 57 turns with the 0.3 mm air gap length produces only an inductance value of 1.1 mH with the selected core. Therefore, a higher number of turns has to be chosen. 88 turns with the same air gap length, 0.3 mm, produces the value of inductance 2.65 mH which is close enough to the desired 2.79 mH.

The number of turns in the secondaries of the ACDC29 is determined equally as the turns for DCDC designs. If the chosen number turns in primary $N_P = 88$ is divided by the turns ratio $N_{PS} = 8.42$, the number of turns in the secondaries is $N_S = \frac{N_P}{N_{PS}} \approx 10.45$. Therefore, the turns in the secondaries is selected to be 11, which results in the turns ratio $N_{PS} = \frac{88}{11} = 8$. If the number of turns were chosen to be 10 instead of 11, the turns ratio would have become larger than 8.42 and the reflected voltage would have grown from the selected value, narrowing the safety margin to the maximum rated voltage of the MOSFET.

The number of turns in the auxiliary winding is calculated with Equation (21). The voltage of the auxiliary winding is designed to be approximately in the middle of the specified operating voltage range $v_{AUX} \approx 19$ V. The selected turns ratios produce lower voltage than 19 V to take into account the effect of cross regulation, which increases the voltages in the lightly loaded windings if compared to the more heavily loaded regulated output.

The calculated and selected properties of the designs are presented in Table 9.

Table 9: Properties of the different designs calculated according to the desired values.

Design	N_P	N_S	N	l_g (mm)	v_{AUX} (V)	L_M (mH)	t_{on} (μs)	i_{Ppk} (A)
DCDC34	92	12	9	1	18.8	1.39	8.88	1.49
DCDC29	92	12	9	0.8	18.8	1.35	8.51	1.49
ACDC29	88	11	8	0.3	18.2	2.65	2.84	0.42

3.5 Allowed thermal rise and losses

The thermal rise of the designs is proportional to the area of the cooling surface as described in 2.3.6. The size of the surface area can be calculated from the dimensions of the cores shown in Figure 29. The different dimensions of the two cores, shown in Figure 29, are presented in Table 10.

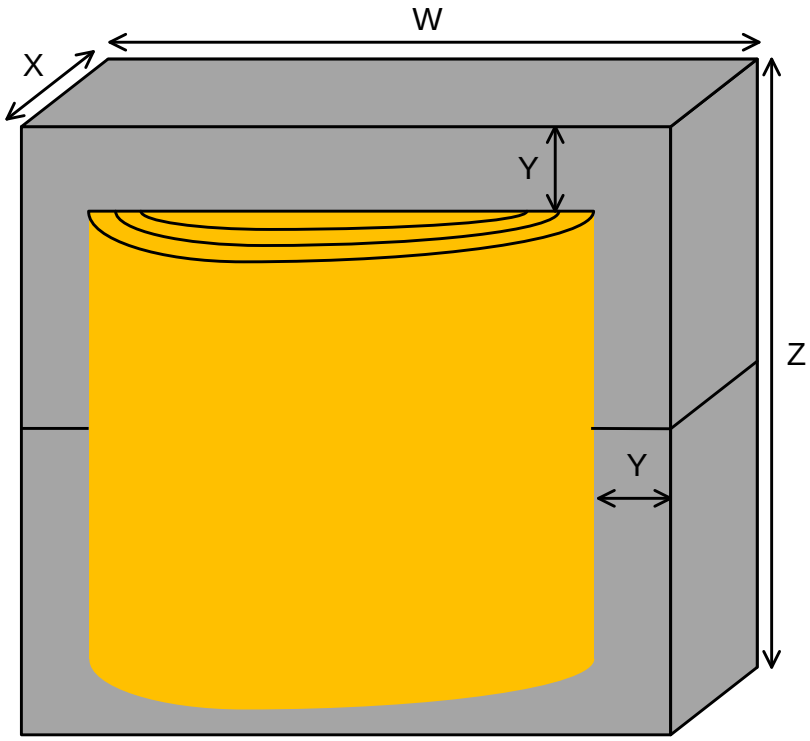

Figure 29: Dimensions of a flyback transformer.

Table 10: Dimensions of Figure 29. [19, p. 541,545]

ETD core	W (mm)	Z (mm)	X (mm)	Y (mm)
34	35	34.6	11.1	5.5
29	30.6	31.6	9.8	5

The areas and allowed losses of both sizes are calculated assuming the maximum temperature rise ΔT of 50°C. This should result in the maximum temperature of 115°C if the ambient is 65°C. Moreover, the window of the core is assumed to be full when calculating the area of the surface. Equation (68) is used in the determination of the allowed losses in Appendix C and the calculated areas and losses are presented in Table 11.
As can be noticed from Table 11, the allowed losses are higher for the larger design because of the larger cooling surface. On the other hand, if the losses are equal, the temperature rise of the larger design is lower.

Table 11: The calculated areas and the allowed losses of the designs.

ETD core	A (cm^2)	P_{loss} (mW)
34	44.6	3298
29	35.0	2588

The allowed copper losses P_{Cu} can be calculated by subtracting core losses from the allowed total losses. The densities of the core losses are determined according to the used switching frequency from Figure B2 and Figure B3 in Appendix B and according to the peak value of the flux swing $\frac{\Delta B}{2}$. In addition, the loss densities are typically reported for certain temperatures and the used graph should be closest to the operating temperature of the design. The chosen graph used in the designs is for 100°C and the values of ΔB are calculated in Appendix C.

Figure 30 shows the graph of Figure B3 in which the densities of core losses have been marked for different designs.

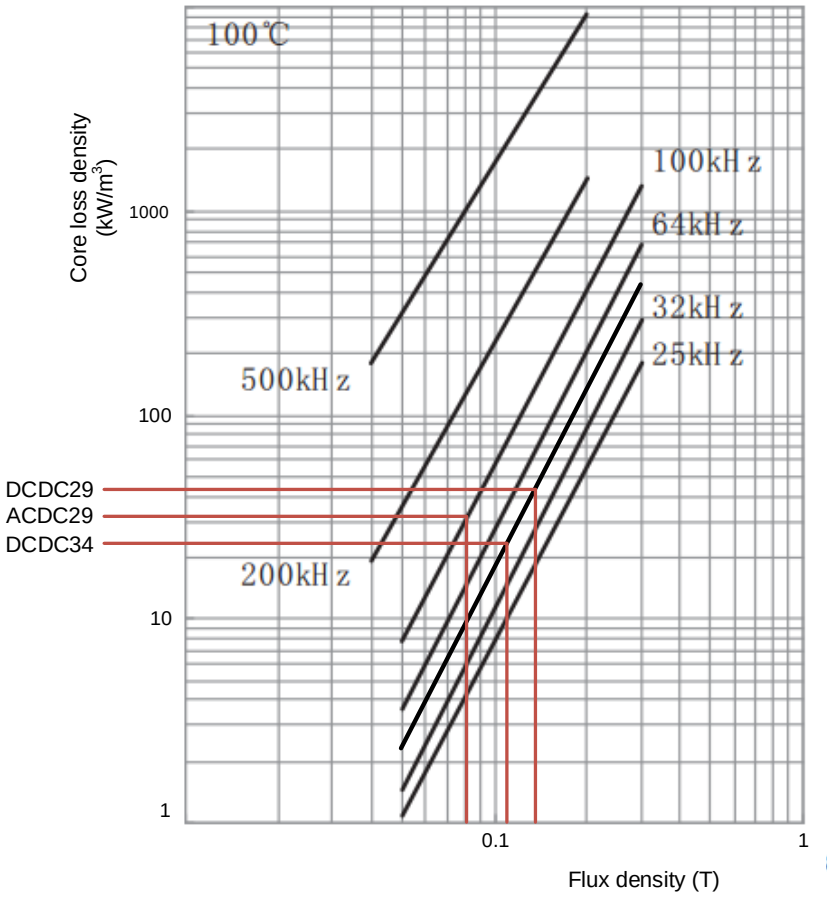

Figure 30: Densities of core losses in the designs using TP4 material from TDG [24].

The unit of the loss density in Figure 30 is kW/m^3 which equals mW/cm^3. Furthermore, the loss density line, between the lines of 32 kHz and 64 kHz, is interpolated

to the graph to facilitate the determination of the values.

The effective volume of the core V_e is calculated by multiplying the effective length of the core l_c by the cross sectional area of the core A_C, which are checked from Table 2. The value of core loss is calculated by multiplying the effective volume of the core by the density of the core loss and the determined values of core and copper losses of the designs are presented in Table 12.

Table 12: Densities of core losses, effective volumes of the cores and core and copper loss.

Design	ρ_{Fe} (mW/cm^3)	V_e (cm^3)	P_{Fe} (W)	P_{Cu} (W)
DCDC34	24	7.63	0.18	3.1
DCDC29	43	5.53	0.24	2.3
ACDC29	32	5.53	0.18	2.4

As can be seen from Table 12, the core losses are lower than 10% of the copper losses in all designs. Therefore, if the temperature rise of the designs will be 50°C, the copper losses is the major cause of the temperature rise.

3.6 Creepage margins and arrangement of windings

Clearance and creepage distances between different windings are needed according to the safety standard as described in 2.1.4. Reinforced insulation is required only in the second output where user can access. Hence, TIW is used in this winding to establish protective separation from other circuits. This means that creepage margins are needed in the ends of coil former to provide functional insulation between the other windings.

The impulse withstand voltage in Figure A2, for designing the clearances of functional insulation, is defined according to the maximum voltage of the dc-to-dc converter and using the overvoltage category 2. The same interpolated impulse withstand voltage, 4771 V, applies for both converters because they are considered to belong into same circuit and this impulse withstand voltage defines more severe requirements for clearance than the temporary overvoltage of the mains circuit or the highest working voltage. The required clearance distance, according to the 4771 V impulse withstand voltage, is approximately 4 mm.

The creepage distance is determined according to the maximum working voltages of the converters. 1100 V is used for both converters as well as the pollution degree of the printed wiring boards, which is 2. The interpolated creepage distance is approximately 5.5 mm. As a result, 3 mm wide tape margins are fitted to both ends of coil formers. These margins ensure that the needed creepage distances is established between all windings. In addition, the required creepages and clearances have to be taken into account when selecting the coil formers and numbers of pins.

The structure of the windings has the effects to the resistance and the leakage inductance of the windings described in 2.3.7 and 2.3.3. In addition, the windings should be able to be spooled by machines to ensure the effortless construction of the windings.

The primary is therefore divided into four layers each consisting of 23 turns per layer. After the first layer is spooled, a single layer of insulation tape is wrapped on top of it to provide insulation. Then, the second layer of the primary is spooled backwards to the same side where the first layer began. The secondaries are located between the two double layers of the primary.

The structure of the DCDC designs is presented in Figure 31. The ACDC design uses the same construction but has different numbers of turns.

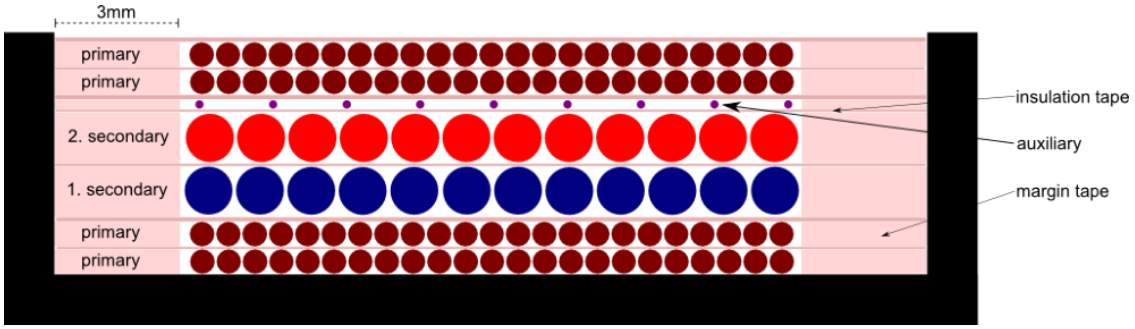

Figure 31: Structure of the DCDC34 and the DCDC29.

The number of insulation tape layers is different between the layers in Figure 31. Two layers of tape is used between the primary and the first secondary, between the auxiliary winding and the primary and on the top of the outermost layer of the primary to provide additional insulation. In addition, the auxiliary winding is spread to the entire width of other windings to increase coupling to the secondaries. Teflon tubing is used in the ends of wires to provide insulation when routing the ends of the windings to the pins of the coil former.

The tape margins add complexity to the structure, but it is the price paid for deciding not to use TIW in all windings. In addition, the margins narrow the available width of the coil former, which may increase the overall thickness of the windings or the ohmic resistance, if the diameters of wires have to be decreased.

3.7 Diameters of wires and ohmic losses

In order to determine the diameters of winding wires, the rms values of currents have to be calculated. The peak values of primary currents have already been presented in Table 9 and the rms values are calculated using Equation (54). Moreover, the peak values of the currents in the secondaries are calculated with Equation (16).

The calculated rms value of the current in the secondaries is further divided between the two separate outputs, according to the relations of the DC values of maximum load currents. The calculated rms values of different designs are shown in Table 13.

In Table 13, the currents $i_{S1,rms}$ and $i_{S2,rms}$ are the rms values of currents in the secondaries and the i_{tot} is the sum of the rms currents with respect to the primary.

Table 13: Calculated rms values of the currents in the windings.

Design	$i_{P,rms}$ (A)	$i_{S,rms}$ (A)	$i_{S1,rms}$ (A)	$i_{S2,rms}$ (A)	i_{tot} (A)
DCDC34	0.57	4.7	2.8	1.9	1.2
DCDC29	0.57	4.6	2.8	1.8	1.2
ACDC29	0.13	1.44	0.69	0.75	0.31

The factor α_i, calculated by Equation (58), depicts the percentual fraction of the window area allocated for the winding carrying current $i_{i,rms}$. The cross sectional areas of each winding wire is then determined according to Equation (59). Moreover, the fillling factor of the window K_u is approximated to be 0.33 for the wires consisting only from one strand. This is higher than the typical values for K_u described in 2.3.4 because the area occupied by the coil formers is already subtracted from the window areas of the cores in Table 2, which are used in the calculations.

The calculated cross sectional areas and maximum diameters of winding wires are presented in Table 14.

Table 14: Cross sectional areas and maximum diameters of wires.

Design	A_{wP} (mm^2)	A_{wS1} (mm^2)	A_{wS2} (mm^2)	d_{wP} (mm)	d_{wS1} (mm)	d_{wS2} (mm)
DCDC34	0.22	1	0.68	0.53	1.13	0.93
DCDC29	0.15	0.74	0.49	0.44	0.97	0.79
ACDC29	0.14	0.76	0.81	0.42	0.98	1.0

Two different wire types are chosen for each design. The first type is a wire made of a single conductor and the second type is a wire consisting of multiple strands to reduce the AC resistance due to high frequency components in the current. Moreover, the diameter of the strands of these Litz type wires is chosen according to the skin depth at 160 kHz, which is calculated using Equation (67). Furthermore, the skin depth at this frequency is selected due to the power losses at the second harmonic of the switching frequency in the intended most common operating point of the dc-to-dc converter [26]. The designs using Litz wire will be marked by adding subscript m to the name of the design.

The diameters of wires are chosen according to the maximum values in Table 14 and by calculating the equivalent number of strands with Equation (62). Nevertheless, the filling factor of Litz type wires is lower than that of a single conductor. This is taken into account by selecting smaller number of strands than calculated. The selected diameters of wires and numbers of strands are presented in Table 15. The final numbers and the diameters of strands in Table 15 were chosen after iterating different diameters by drawing the window area using correct dimensions of coil formers, margin barriers, insulation layers, wire insulation and diameters of wires. The drawing of the DCDC34$_m$, with the chosen winding wires, is presented in Figure 31. In addition, the availability of Litz type TIW for the second secondaries delimited the maximum diameter of one strand to 0.3 mm. For this reason, the maximum diameter of strands of all Litz type wires was chosen to be 0.3 mm.

Table 15: Chosen diameters of conductors and numbers of strands.

Design	$d_{wP,p}$ (mm)	p_P	$d_{wS1,p}$ (mm)	p_{S1}	$d_{wS2,p}$ (mm)	p_{S2}
DCDC34	0.55	1	1	1	0.9	1
DCDC34_m	0.25	3	0.3	8	0.3	7
DCDC29	0.4	1	0.9	1	0.7	1
DCDC29_m	0.2	3	0.28	7	0.23	7
ACDC29	0.4	1	0.8	1	0.9	1
ACDC29_m	0.2	3	0.28	6	0.27	7

The calculated skin depth at 160 kHz is 0.19 mm and the maximum diameter based on this value would be 0.38 mm. As a result, the selected maximum diameter of strands, in the Litz type wires, corresponds to the skin depth at 258 kHz.

The ohmic losses of windings are calculated according to Equation (64) and the ohmic resistance is determined by Equation (65). In order to determine the resistances, the mean lengths per turn have to be calculated. Furthermore, to calculate the mean lengths per one turn, the radius of the coils are determined according to the distances of different windings in Figure C1. The calculated ohmic resistances and current densities of windings and the ohmic losses of different designs are presented in Table 16.

Table 16: Calculated ohmic resistances of the windings, current densities in the windings and the ohmic copper losses of the designs.

Design	R_{0P} (Ω)	R_{0S1} (Ω)	R_{0S1} (Ω)	J_P (A/cm^2)	J_{S1} (A/cm^2)	J_{S2} (A/cm^2)	P_{Cu0} (W)
DCDC34	0.53	0.019	0.027	240	357	299	0.42
DCDC34_m	0.86	0.027	0.035	387	495	384	0.62
DCDC29	0.89	0.021	0.040	454	440	468	0.58
DCDC29_m	1.19	0.031	0.052	605	650	619	0.80
ACDC29	0.85	0.024	0.022	103	137	118	0.04
ACDC29_m	1.13	0.033	0.035	138	187	187	0.05

As can be seen from Table 16 the values of ohmic copper losses are a minor fraction from the allowed total copper losses of Table 12. This means that AC losses is the major part of the copper losses or on the other hand, the temperature of the component will not rise 50°C. Moreover, the current densities and the calculated ohmic losses of both ACDC designs are low compared to the DCDC designs and the current density in the DCDC29_m design exceeds the typical maximum of 500 A/cm^2 according to 2.3.5.

3.8 Costs

The designed flyback transformers were ordered from a contract manufacturer. The components were manufactured according to the specifications which are based on

the calculated and selected properties of the designs. The relative costs of the designs are shown in Table 17.

Table 17: Costs of complete designs. The cost of the most expensive design equals 100 %.

DCDC34 (%)	$DCDC34_m$ (%)	DCDC29 (%)	$DCDC29_m$ (%)	ACDC29 (%)	$ACDC29_m$ (%)
85	100	62	77	69	79

The largest designs are the most expensive, as can be seen from Table 17. This is due to the higher amount of used materials if compared to the smaller designs. In addition, designs in which Litz wire is used, are more expensive than the otherwise similar designs in which the windings are made from single conductors.

In order to find out what are the most expensive materials in the designs, the costs are broken down to show the portions of the different materials. The relations of different costs to the costs of the complete components are presented in Table 18.

Table 18: Costs of different materials in relation to the cost of the complete component.

Design	Core (%)	Coil former (%)	Wire P (%)	Wire S1 (%)	TIW S2 (%)	Labor (%)	Other costs (%)
DCDC34	22.5	9.7	10.8	4.7	13.2	29.5	9.6
$DCDC34_m$	19.0	8.2	8.7	3.6	32.4	19.9	8.2
DCDC29	15.6	10.7	6.7	4.5	10.3	40.1	12.1
$DCDC29_m$	12.5	8.6	4.8	3.4	28.7	32.2	9.8
ACDC29	14.0	9.7	6.0	3.0	13.0	43.3	11
$ACDC29_m$	12.2	8.4	4.6	2.4	33.7	29.3	9.4

In Table 18, the other costs include the costs of insulation tape, margin tape, epoxy, wire of auxiliary winding, teflon tubing and tin used for soldering. Furthermore, the standardized diameters of enamelled wire, shown in Table 15, are used in the primary and in the secondary S1.

Table 18 shows that the proportion of the Litz type TIW, used in the second secondaries, is approximately 30 % of the complete component, although it was only used in one secondary winding of 11 or 12 turns depending on the design. Moreover, the single conductor TIW seems to be approximately 60 to 70 % cheaper than the Litz type TIW. On the other hand, the usage of Litz type wires has an effect on the manufacturing time of the component if the diameter of the used wire is close to 1 mm or over. This is because single conductors of such diameter are beginning to be stiff, which affects the time used for manufacturing the component and therefore, the costs of labor. If all windings would have been completely made of TIW, the costs of labor and other costs would have decreased but the costs of windings would have increased more. Contrary to TIW, the cost of Litz type enamelled wire was not higher than the cost of the enamelled wire consisting of the single conductor.

In addition to TIW, an important part affecting the overall cost of the component is the size of the core. The ETD34 core, made of TP4 material by TDG, was twice as expensive as the ETD29 used in the smaller designs.

For a comparison to costs in Table 18, the costs of $DCDC34_m$ is calculated using Litz type TIW in all windings. The cost of the primary is calculated using the TIW of $DCDC29_m$ design and scaling the cost with the relation of the mean lengths per turns to the $DCDC34_m$ and finally multiplying by the turns ratio 7.67. Furthermore, the same TIW, as in the second secondary of $DCDC34_m$, is used in both secondaries but the costs are scaled by the relations of the mean length per turns. In addition, the labor costs are assumed to decrease by a third and other costs by 10% because the margin tapes are no longer needed for creepages in the construction.

The calculations are shown in Appendix C and the costs of the materials and the complete design are presented in Table 19.

Table 19: Costs of the different materials and the complete design, in relation to the cost of the $DCDC34_m$ design in Table 17, if TIW is used in all windings of $DCDC34_m$.

Core (%)	Coil former (%)	Wire P (%)	Wire S (%)	Labor (%)	Other costs (%)	Complete (%)
19.0	8.2	183	60.7	13.3	7.4	292

As can be seen from Table 19, the costs of windings increase significantly and the cost of the complete component increases to 292 % of the cost in Table 17. On the other hand, the calculation does not take into account the possible reductions in the prices of TIW which may result from the increased amount used in the components.

The advantage of using TIW is that a smaller size of the core could possibly be chosen because the creepage margins are no longer needed. However, the thickness of the windings can become a problem with multiple secondaries.

The design process of the flyback transformers was presented in this chapter. The process began by determining the initial values and was followed by calculating the properties and selecting the materials of the components. The process ended to breaking down the costs of the materials. The suitability of the designs for the intended applications will be verified in the next chapter.

4 Verifications of flyback transformers

In this chapter, the operation of the designed flyback transformers is verified by measurements. The magnetizing and leakage inductances of primary and resistances of all windings are measured as function of frequency. Furthermore, the currents saturating the cores of the designs and maximum voltage stress of the secondary diodes are found out. In addition, the operation of the designs is tested in the intended application with typical minimum and maximum loads. Finally, the thermal rise of the designs will be verified with the maximum load currents.

The methods and the equipment of the different tests are introduced before presenting the results. The results are compared to the theory and calculated values, presented in the previous chapters.

4.1 Measurement of inductances

The magnetizing and leakage inductances between primary and secondaries were determined with Agilent 4294A precision impedance analyser, which measures the complex impedance of the DUT (device under test) as function of the selected frequency range. Figure 32 shows the measured impedance, from the primary, of a sample of DCDC29 design.

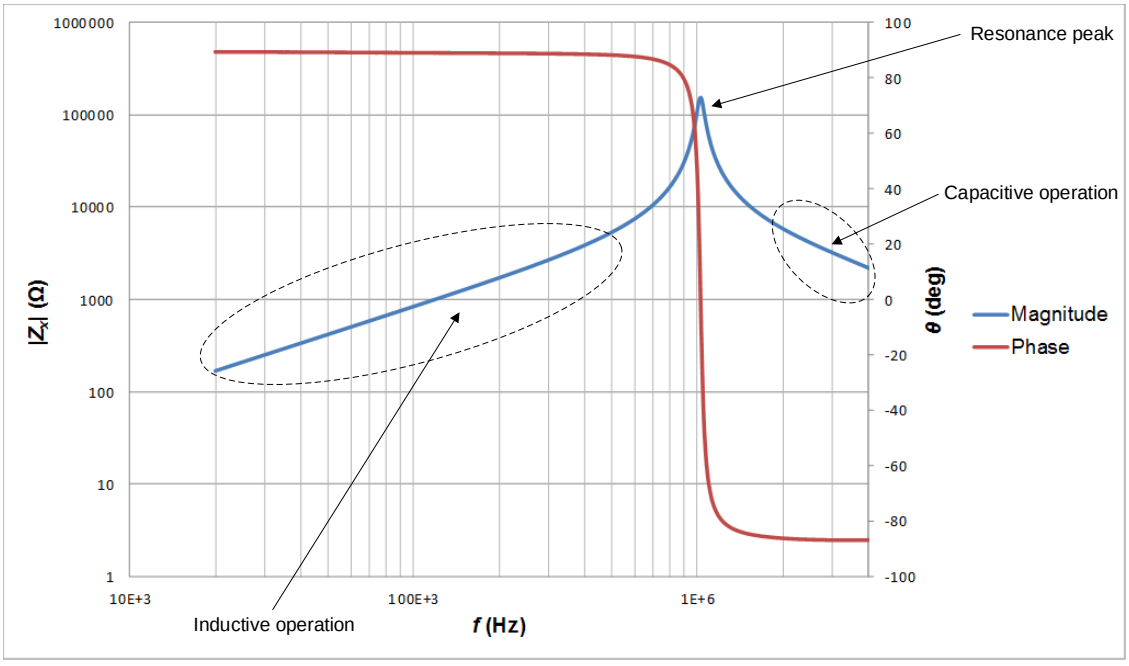

Figure 32: Impedance curve of a DCDC29 design.

Three different characteristic regions can be noted from the magnitude curve of Figure 32. The first one is the region of inductive operation. This region is the linearly increasing part of the curve at frequencies lower than the resonance peak. The second one is the resonance in which the inductance and the capacitance of the

inductor are in series resonance. The third is the region of capacitive operation where the magnitude of the impedance decreases linearly. In addition to the magnitude curve, the phase curve shows the shift of the operation from inductive to capacitive at the frequency of the resonance. [32]

The value of inductances are calculated from the measured impedance according to

$$L = \sin(\theta)\frac{|Z_x|}{2\pi f} \tag{69}$$

where θ is the phase angle of the impedance in degrees, $|Z_x|$ is the magnitude of the impedance and f is the frequency. The frequency range of the calculated inductance is selected to be in the linearly increasing region of the magnitude curve.

The 4294A precision impedance analyzer uses auto-balancing bridge method to measure impedance. In the method, the DUT is connected between the high and low terminals and the potential of the low terminal is maintained at zero volts. The potential of the high terminal is measured directly by a vector volt meter while the current flowing through the DUT is determined by measuring the voltage with a vector volt meter over a range resistor R_r. Consecuently, the complex impedance is calculated by

$$Z_x = \frac{v_x}{v_x} = R_r\frac{v_x}{v_R} \tag{70}$$

where v_x is the voltage over the DUT, i_x is the current through the DUT, R_r is the value of the range resistor and the v_R is the voltage over the range resistor. [32]

The value of the range resistor determines the measuring range and therefore, the accuracy of the measurement. The value of the resistor is known and it is changed automatically based on the impedance of the DUT. Figure 33 presents the configuration of the measurement method.

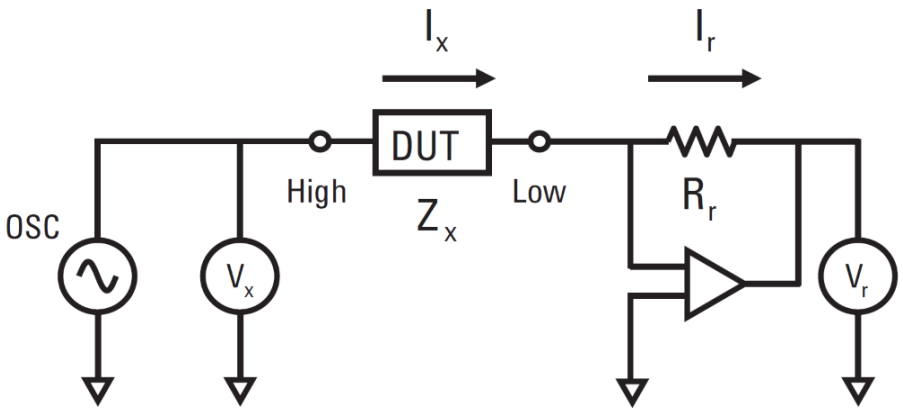

Figure 33: Impedance measurement using auto-balancing bridge method. [32]

In Figure 33, the oscillator generates a signal leading to the currents i_x through the DUT and i_r through the range resistor R_r. Because the potential of the low terminal is zero volts, the two currents are equal. [32]

The inductance of the components is measured by connecting one end of the primary to the high and the other end to the low terminal of Agilent 16047E test fixture, which is attached to the precision impedance analyzer. Coupling from primary to the test fixture was ensured by soldering approximately 7 cm long copper strips to the pins of primaries and attaching the strips to the high and low terminals by the screw clamps of the fixture. Figure 34 presents the coupling of the components to the test fixture.

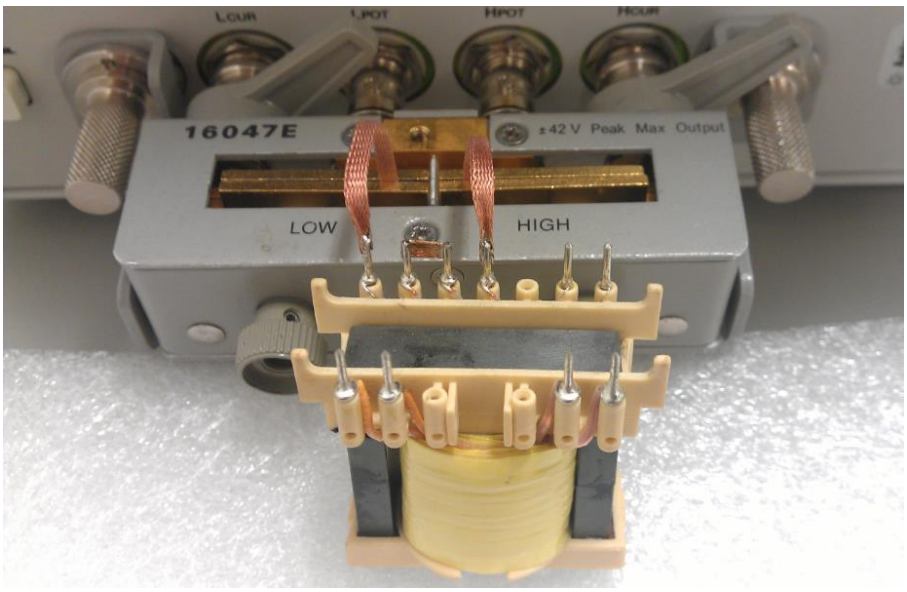

Figure 34: DCDC34 attached to the test fixture by copper strips.

When measuring the magnetizing inductance, all secondaries, including auxiliary windings, were left open. Contrary to magnetizing inductance, leakage inductances were measured from the primary by short circuiting all the secondaries. [33]

The precision impedance analyzer was turned on approximately 30 minutes before conducting the measurements in a typical room temperature. In addition, the analyzer was always calibrated before conducting the measurements by measuring the impedance of open circuit and then by short circuiting the high and low terminals with a gold plated piece of metal. The measured impedance of the piece is shown in Figure 35. Figure 35 shows that noise limits the accuracy of the analyzer to approximately 1 mΩ.

Curves presenting typical magnetizing inductances are shown in Figure 36. The inductances of DCDC29 in the curves of Figure 36 are calculated with Equation (71) from the measured impedances. Furthermore, the accuracy of the precision impedance analyzer is at least ± 0.1 % of the measured values in a frequency range from 10 kHz to 300 kHz and with a 0.5 V rms signal of the oscillator [34].

The curves in Figure 36 are flat from the 10 kHz to approximately 100 kHz until the inductance begins to increase. The increase is a consequence of the series resonance occuring at a higher frequency.

The curves of other designs are not presented because the trends are close to that

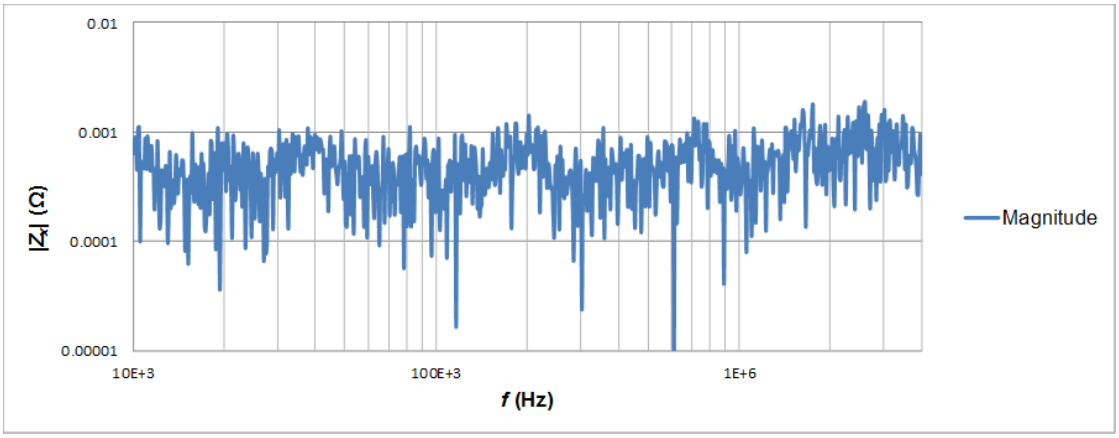

Figure 35: Magnitude of the measured impedance of the short circuiting piece.

seen in Figure 36 and the increase of the inductances, due to the resonance, do not lead to problems in the application. Instead, the mean values of mutual inductances, calculated for 5 samples at 100 kHz, scattering of the values and the differences to the calculated values of 3.4 are presented in Table 20.

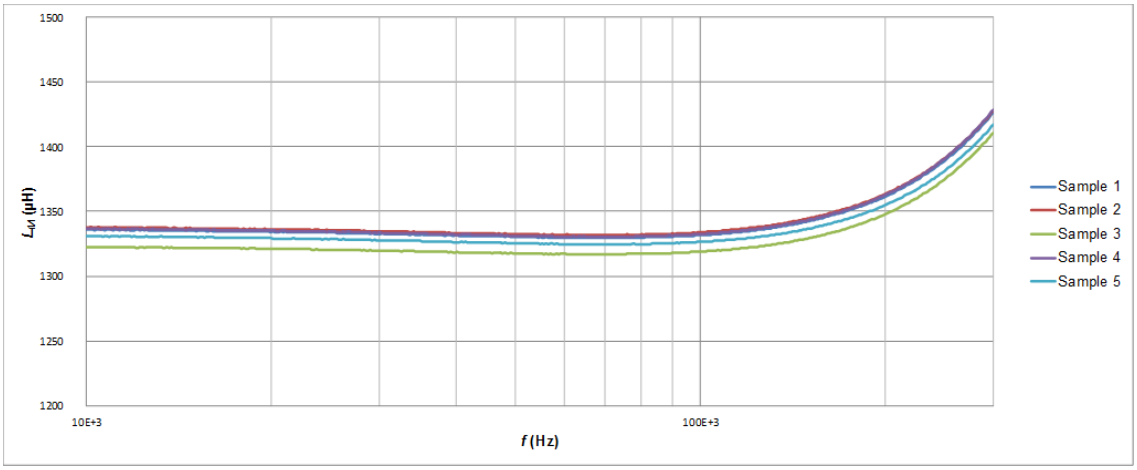

Figure 36: The magnetizing inductances of DCDC29 calculated from the measured impedances of 5 samples.

In Table 20, the highest difference to the calculated mutual inductances of 3.4 is 6 %, which means that the measured values are generally well in line with the calculated values. The differences may originate from differences in the actual lengths of air gaps or differences between calculated and actual complete numbers of turns. In addition, the maximum scattering between different samples is 2 %, which means that structural differences between the samples are small. Furthermore, if the cores come from the same production run, the differences in the dimensions and the properties of materials of the cores should be small between the samples.

Table 20: Measured mutual inductances at 100 kHz, scattering between different samples and differences to the calculated values of L_M of the previous chapter.

Design	L_M (mH)	Scattering (%)	Difference (%)
DCDC34	1.40	±1	+1
DCDC34_m	1.43	±1	+3
DCDC29	1.33	±1	-1
DCDC29_m	1.27	±2	-6
ACDC29	2.73	±1	+3
ACDC29_m	2.58	±1	-3

The leakage inductances of the primaries are measured only from a single sample to find out differences between designs. Moreover, the accuracy of the precision impedance analyzer is at least ±1 % of the measured values in the frequency range from 10 kHz to 1 MHz and with a 0.5 V rms signal of the oscillator [34].

The DCDC designs are compared to a flyback transformer, referred to DCDC39, which has the same number of turns in the primary and in the secondaries as in the designed components. Furthermore, the DCDC39 is constructed using ETD39 core size and the interleaved windings are all made of Litz type TIW. The measured leakage inductances of the DCDC designs are presented in Figure 37.

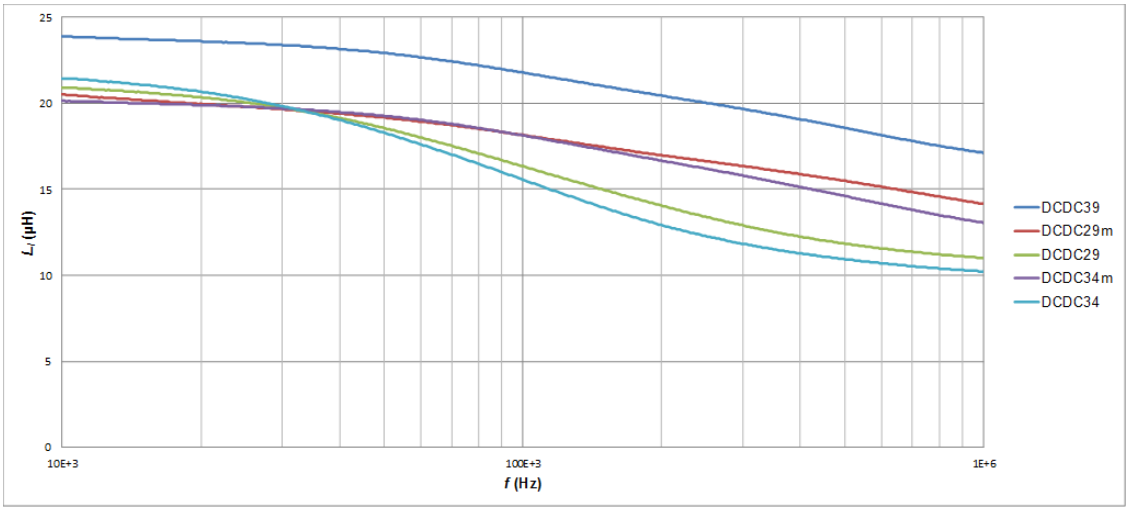

Figure 37: Measured leakage inductances of the DCDC designs.

The measured leakage inductances of all designs, excluding DCDC39, are below 2 % of the measured mutual inductances. In addition, the trend of the curves in Figure 37 are decreasing as the frequency increases, which is a consequence of proximity effect between the windings [33]. Furthermore, this is more pronounced in the DCDC34 and DCDC29 in which the windings are made of single conductors of larger diameter than in the other designs. Moreover, the leakage inductance is somewhat greater in the DCDC39 design, than in the others, because the distance between secondaries and the primary is larger due to the additional thickness of the

wire insulations. This leads to a worse coupling between the primary and the secondaries which can be noted as the higher leakage inductance in the measurements, as described in 2.3.3, if compared to other designs.

The leakage inductances of the ACDC designs are compared to a design which is constructed using ETD34 core size and in which the primary is made of six layers of Litz type enamelled wire. Furthermore, the windings are interleaved and the design is referred to ACDC34. The measured leakage inductances of the ACDC designs are presented in Figure 38.

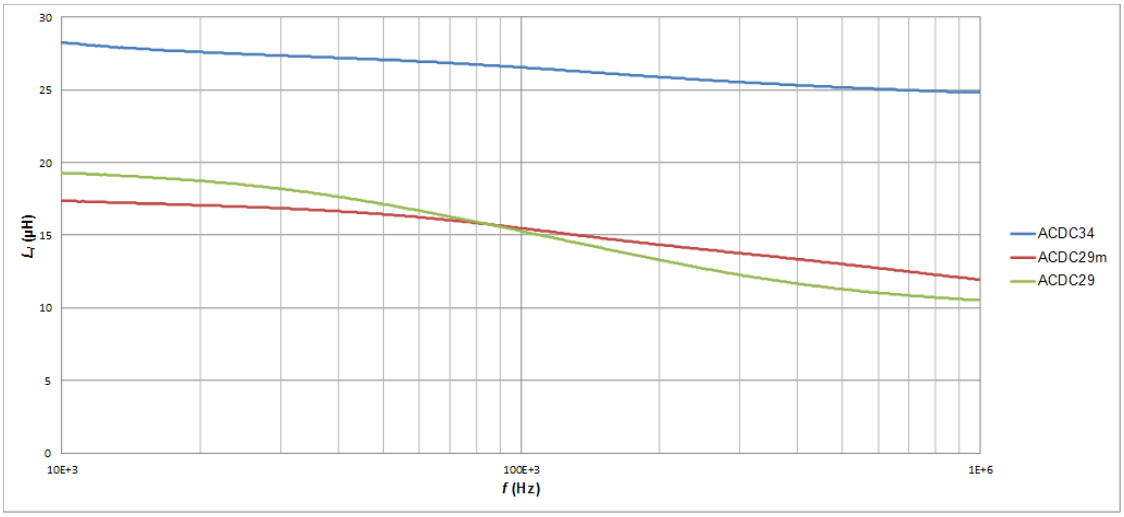

Figure 38: Measured leakage inductances of the ACDC designs.

In Figure 38, the leakage inductances of both ACDC29 designs are below 1 % of the measured mutual inductances. In addition, as with the DCDC designs, the proximity effect can be noted from results of ACDC designs. Furthermore, the measured leakage inductance of the ACDC34 is higher than that of other two designs. This is a consequence of the two additional layers in the primary which makes the overall thickness of the primary greater than in the two other designs. Moreover, the effect of the series resonance to the leakage inductances can not be seen from Figure 37 or from Figure 38 because the proximity effect covers the increase of the leakage inductance in the observed frequency range and the series resonances occur at higher freuquencies than with the mutual inductance.

4.2 Measurement of resistances

The resistances of the designs are measured with the same equipment as the inductances. Moreover, the resistances are calculated from the measured impedances by

$$R = \cos(\theta)|Z_x| \tag{71}$$

where $|Z_x|$ is the magnitude of the measured impedance.

Resistances of windings were measured only from a single sample because the structural differences were assumed to be small and their effect to the resistances is not relevant. The measurements were conducted on one winding at a time with other windings left open. Furthermore, approximately 7 cm long copper strips were soldered to the pins of the windings to ensure a good coupling between the component and the test fixture. Furthermore, the measurements were conducted in a typical room temperature.

Figure 39 shows the typical behaviour of the measured resistances as function of frequency.

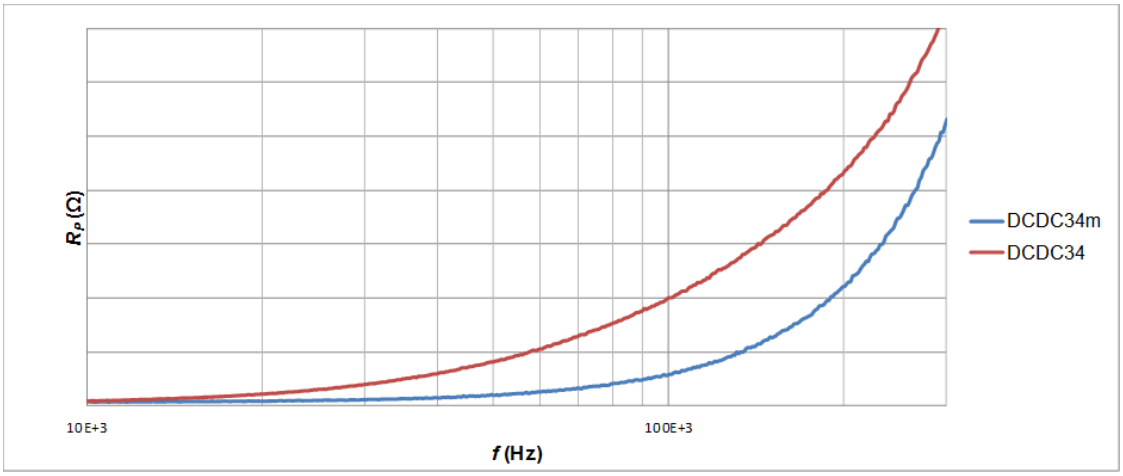

Figure 39: Measured trends of primary resistances of DCDC34 and DCDC34$_{\mathrm{m}}$

.

The increase of the resistance can be noted from Figure 39 as the frequency increases. This results mainly from skin effect, which was described in 2.3.6. Moreover, the effect is less pronounced in the winding of DCDC34$_{\mathrm{m}}$ because the windings of the design are made of Litz wire, which reduces the skin effect and the total AC resistance.

The trends of the resistance curves of primaries and secondaries are similar to the curves seen in Figure 39. Therefore, only the measured resistances and the accuracies, at 45 kHz, are presented in Table 21 and at 100 kHz in Table 22.

The accuracies in Table 21 and Table 22 are the accuracies of the precision impedance analyzer with a 0.5 V rms signal of the oscillator [34]. The measured resistances are generally higher than the calculated ohmic resistances in Table 16. This results from the effects of AC resistance, which are already visible in the values of Table 21. Moreover, the resistances of the windings, made of Litz wire, are approximately equally lower in Table 21 and in Table 22 than the resistances of the windings made of single conductors. In addition, the resistances in Table 21 are lower than the resistances in Table 22, which is a consequence of the higher effects of AC resistance with the increased frequency.

The higher resistance as the frequency increases refers to a higher thermal rise of the component due to the increased copper losses. Because the operating frequency

Table 21: Measured resistances of primaries and secondaries at 45 kHz.

Design	R_P (Ω)	Accuracy (Ω)	R_{S1} (Ω)	Accuracy (Ω)	R_{S2} (Ω)	Accuracy (Ω)
DCDC34	7.11	±0.32	0.136	±0.019	0.193	±0.023
DCDC34_m	1.71	±0.32	0.049	±0.023	0.064	±0.023
DCDC29	4.57	±0.30	0.089	±0.019	0.145	±0.020
DCDC29_m	1.52	±0.29	0.054	±0.019	0.067	±0.019
ACDC29	3.66	±0.62	0.080	±0.012	0.108	±0.012
ACDC29_m	1.85	±0.58	0.056	±0.011	0.061	±0.012

Table 22: Measured resistances of primaries and secondaries at 100 kHz.

Design	R_P (Ω)	Accuracy (Ω)	R_{S1} (Ω)	Accuracy (Ω)	R_{S2} (Ω)	Accuracy (Ω)
DCDC34	20.07	±0.71	0.371	±0.015	0.463	±0.015
DCDC34_m	5.85	±0.72	0.123	±0.015	0.168	±0.016
DCDC29	12.99	±0.67	0.234	±0.014	0.331	±0.014
DCDC29_m	3.77	±0.66	0.098	±0.014	0.131	±0.014
ACDC29	10.99	±1.40	0.199	±0.028	0.272	±0.028
ACDC29_m	4.83	±1.32	0.113	±0.026	0.134	±0.026

of the flyback transformers will increase as function of input voltage, as described in 2.2.6, the thermal rise of the component will be higher as the input voltage is increased.

The AC resistance of the windings, during the actual operation in the intended application, will be higher than what was measured. This results from the higher flux density in the core, which will increase the fringing flux and therefore the resistance in the windings close to the air gap. In addition, the proximity effect will increase the resistance as the conductors of different layers form higher surrounding magnetic field strengths around conductors than during the measurements.

4.3 Operation in different operating points

The operation of the components is verified by first measuring the saturation behaviour of the designs and then as part of the intended flyback converters, mounted on the PCB. Moreover, the tests in the intended application include verifying the operation with the lowest and highest specified input voltages of the converters. Furthermore, the operation of the components is verified with minimum and maximum load currents with the both input voltages. In addition, the voltage stress over the freewheeling diode, in the secondary S1, will be measured to verify that the rated voltage of the diodes is not exceeded.

The current saturating the components is measured with a power choke tester DPG-10-1500A from ed-k. Furthermore, the saturation behaviour was only measured from one sample of all designs. During the measurements, the DUT was

connected to the power choke tester with one meter long test leads. The connection to the copper strips, soldered to the pins of primaries, was made using alligator clips. This type of connection might add inductance to the measurements and because of that, these type of test leads are not recommended by the manufacturer for measuring inductances of less than 10 μH [35]. Moreover, the other windings were left open during the measurements.

DPG-10 measures voltage over the DUT and current flowing through the DUT. The device calculates the inductance of the DUT as function of current from the slew rate $\frac{di}{dt}$ of the measured current, according to the applied volt seconds. Before the measurements, the voltage of the measurement pulse is selected from the typical operational range of the converter and the maximum duration of the pulse is set high enough to let the rising current saturate the core. furthermore, the measurement was conducted on the components in a typical room temperature. The measured saturation curves of the components are presented in Figure 40.

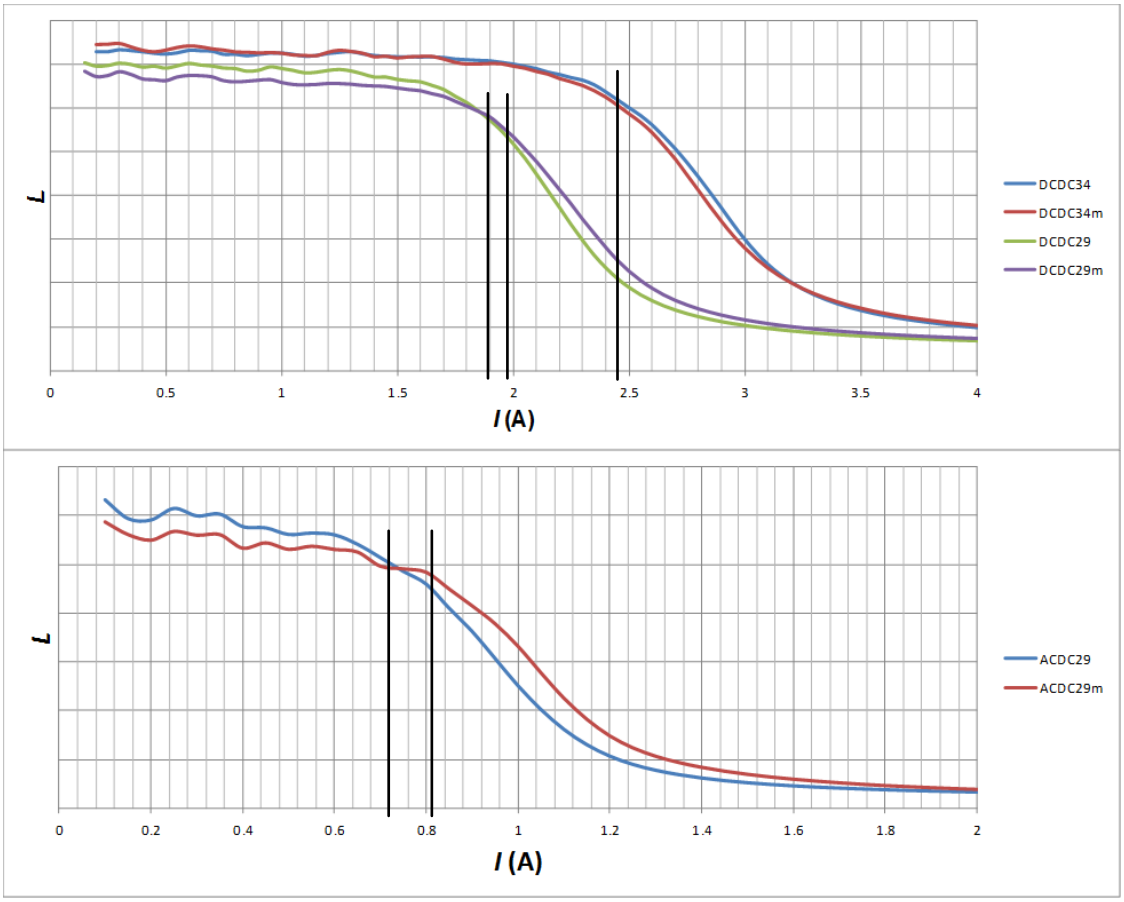

Figure 40: Measured saturation behaviour of the designs. The results of DCDC designs above and ACDC designs below.

In Figure 40, the cores begin to enter saturation with a value of the current at the beginning of the linearly decreasing part of the inductance curves. These points

are marked to the curves by black lines. Moreover, the accuracy of the current in Figure 40 is less than ±3 % of the values [35].

Because the measurement was conducted in a room temperature, the actual saturation behaviour may be different and the cores may enter saturation with a lower current than in the room temperature. This can be assumed by comparing the amplitude permeability curves of the materials in the room temperature and in the temperature of 100°C. For example, DMR40 material in Figure B2, which has similar characteristics than the TP4 material, will enter saturation with a lower current in the higher temperature.

The value of the voltage pulse, used in the measurements, was 240 V for DCDC designs and 390 V for ACDC designs. According to the measured curves in Figure 40, the current saturating the cores is higher than the calculated peak values of primary currents in 3.4. The peak values of calculated primary currents are 1.49 A for DCDC designs and 0.42 A for ACDC designs. This means that all the components should operate without problems at least in the room temperature.

The differences between the similar designs may result from differences in the grinding of the air gaps or in other dimensions of the cores. In addition, the actual number of complete turns has an effect on the saturation behaviour. Furthermore, the ripple in the inductance occurs from the quality of the generated pulse of the power choke tester with the chosen voltage.

The operation with minimum and maximum input voltages was tested on a PCB in a laboratory environment. The PCB was not mounted to the PV inverter due to practical reasons and therefore the verification was not done as part of the final actual application. Moreover, the temperature in the laboratory was the typical room temperature during the measurements. The vertical resolution of the oscilloscope is 8 bits which determines the accuracy of the results obtained from the screen captures of the oscilloscope [36]. The equipment, used in the measurements, are presented in Table 23.

Table 23: Equipment used for verifying the operation on PCB.

Manufacturer	**Type**	**Description**
Tektronix	DPO4034D	Oscilloscope
Fug	MCA 750 - 1500	DC power supply
EA	EL 3400-25	Electronic load
TTi	LD300	Electronic load
Trafox	3kLS-9.6k-400-0-400	Adjustable transformer
Testec	2.5kV x100	Passive voltage probe
Tektronix	N2890A	Passive voltage probe

The DC power supply provides the controllable input voltage and feeds the current demand for the DC-to-DC converter. Furthermore, the controllable electronic loads are connected to the outputs of the converters and the passive voltage probes are used to measure the v_{DS} of the MOSFET and value of the currents in the primaries. Moreover, the current is measured by measuring a voltage over a shunt resistor of known value.

Figure 41 presents the measured v_{DS} and i_P of the DCDC29$_{\mathrm{m}}$ operating with the minimum input voltage of 240 V and maximum output current of 3 A.

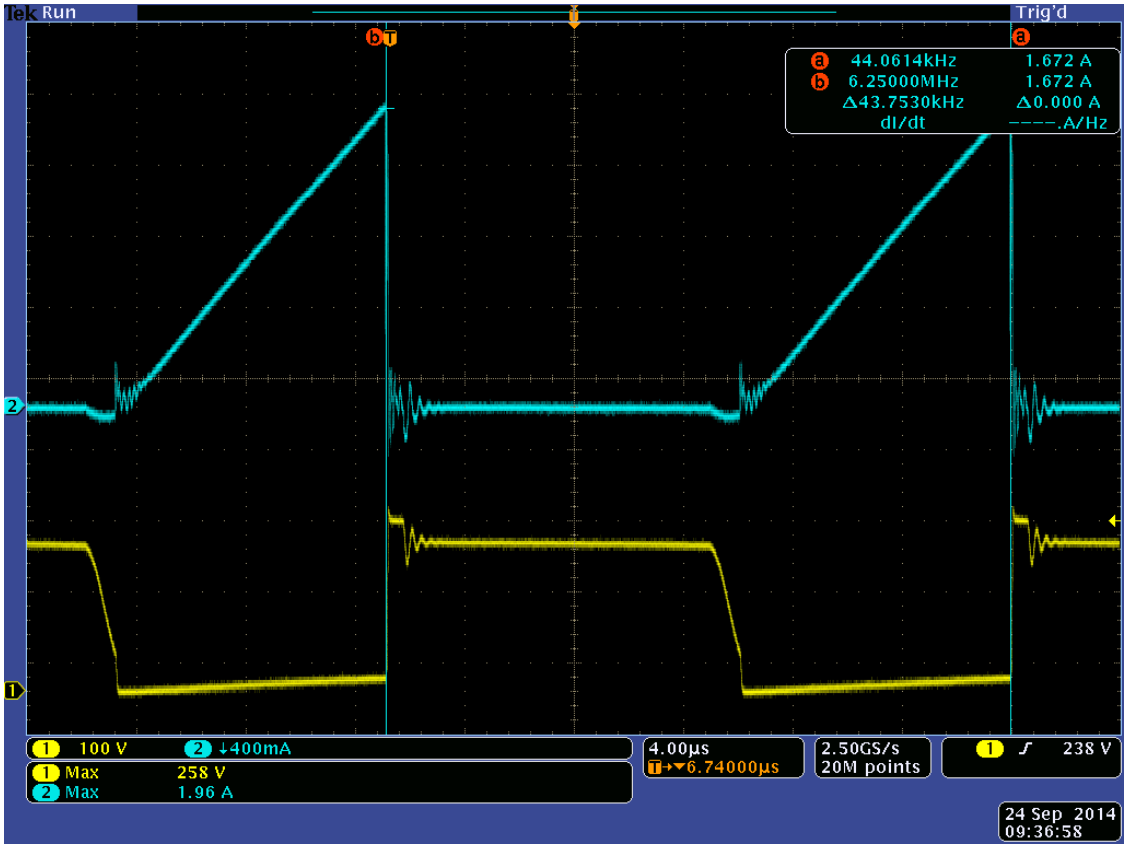

Figure 41: Measured waveforms of the DCDC29$_{\mathrm{m}}$ with minimum input voltage and maximum output current of 3 A. Yellow denotes v_{DS} and blue denotes i_P.

Typical characteristics of the double ended flyback converter circuit, described in 2.2.6, can be noted from the measured waveforms of Figure 41. The converter operates in the QR mode ensuring the highest duty ratio and switching in the first walley of the resonance that occurs between the primary inductance and parasitic c_{DS} capacitance of the MOSFET. The measured switching frequency of the converter is approximately 44 kHz, which is somewhat lower than the calculated 50 kHz in Appendix C. This might result from the fact that the operating modes were not accurately preprogrammed for these designs, as they should have been, according to the datasheet of the control circuit [15]. In addition, the peak value of current in Figure 41, 1.67 A ±1 %, is higher than the calculated 1.49 A. The measured value of peak current is limited to the measured value by the controller circuit, meaning that the current can't increase any higher, which means that the output power is decreased. This was observed as decreased output voltages in the volt meters of the electronic loads because the loads were set to current control mode.

The operation of the same design with maximum input voltage and 0.4 A load current is shown in Figure 42.

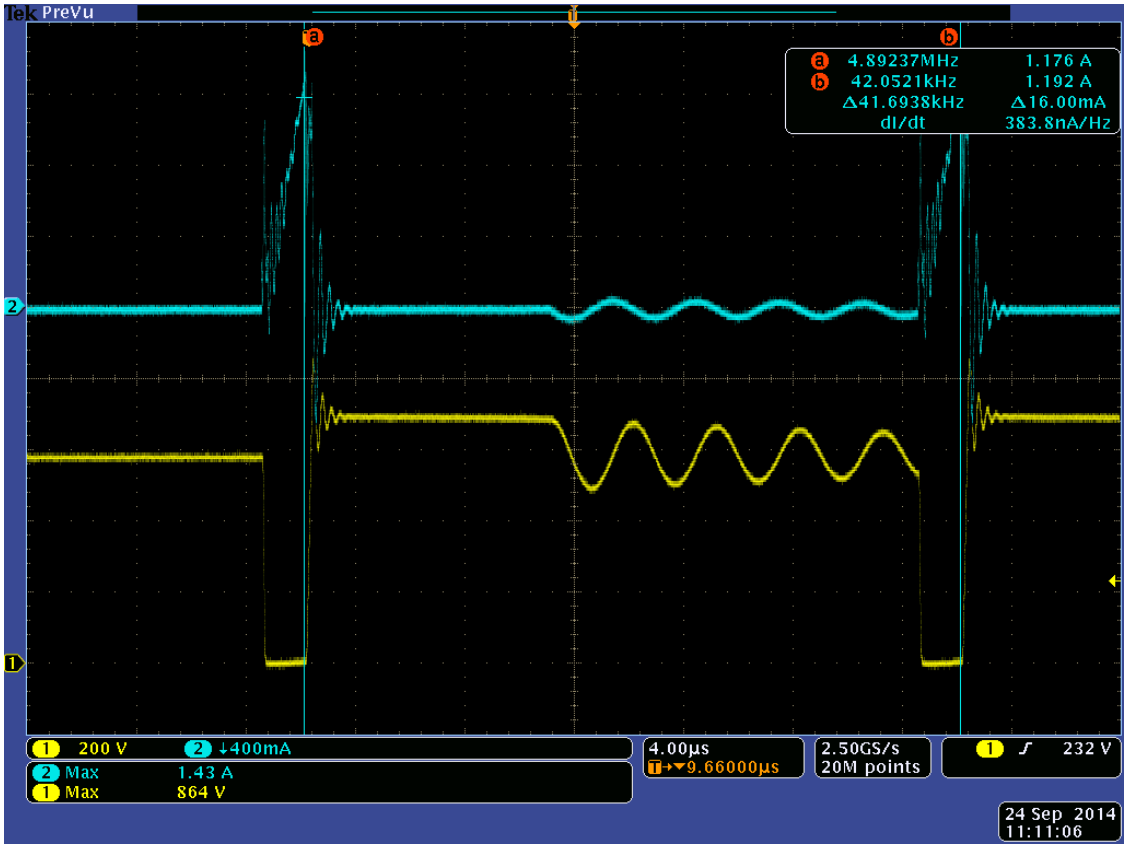

Figure 42: Measured waveforms of the DCDC29$_{\mathrm{m}}$ with the 1100 V input voltage and 0.4 A output current. Yellow denotes v_{DS} and blue denotes i_P.

The converter operates in the green mode with the waveforms of voltage and current shown in Figure 42. Moreover, the converter utilizes walley switching but the t_{res} is higher and duty ratio is smaller than in Figure 41. In the green mode, the converter generates bursts of switching periods with the minimum switching frequency as described in 2.2.6.

Contrary to the DC-to-DC converter, the measured v_{DS} of the AC-to-DC converter was higher than the input voltage as described in 2.2.4. Moreover, the maximum measured v_{DS} of ACDC designs was 1130 V ±1.7 % including the voltage spike with maximum input voltage of 750 V. The minimum voltage of the ac-to-dc converter was produced by connecting the input of the converter to the adjustable transformer that was connected to a three phase grid. The output voltage of the transformer was then adjusted to the minimum value of the converter. However, the maximum voltage for the same converter was provided by connecting the input to the DC power supply, because the maximum output voltage of the adjustable transformer was only 400 V.

Because the observed operation of all designs is comparable to that presented in Figure 41 and Figure 42, the results of the designs are presented in Table 24.
The accuracy of the measured peak currents is ±2 % of the value in Table 24. The

Table 24: The measured i_{Ppk} and f_{sw} with minimum and maximum input voltages and maximum load currents.

Design	V_{Dmin} (V)	i_{Ppk} (A)	f_{sw} (kHz)	V_{Dmax} (V)	i_{Ppk} (A)	f_{sw} (kHz)
DCDC34	240	1.67	42	1100	1.09	85
DCDC34_{m}	240	1.67	42	1100	1.07	84
DCDC29	240	1.67	42	1100	1.10	88
DCDC29_{m}	240	1.67	44	1100	1.10	91
ACDC29	410	0.44	94	750	0.35	100
ACDC29_{m}	410	0.44	98	750	0.40	102

operation mode of both converters was DCM with the maximum input voltages and with the minimum voltage, the converter operated in the QR mode as described in 2.2.6. In addition, the primary current of the dc-to-dc converters was limited by the control circuit which resulted in lower than 24 V output voltage with the minimum input voltage. However, increasing the input voltage to approximately 250 V, the peak value of the current was no longer limited by the controller and the output voltages appeared as the 24 V. This does not affect the operation of the PV inverter in the final application beacuse the initial specified input voltage range is slightly wider than the actual operational input voltage range in the final application.

All designs operated without problems in all verified operating points. Nevertheless, the measured switching frequencies of all DCDC designs in Table 24 are closer to the f_{min} of the controller than what was expected according to the calculations in Appendix C. This should be taken into account by increasing the length of air gap or decreasing the number of turns, if the designs are further developed in future. This decreases the primary inductance of the components and as a result, the converters should operate with a higher switching frequency. Moreover, the scattering between the samples will probably increase as the number of manufactured components increase because of the different production runs of the cores. As a result, a larger frequency margin should be designed to be sure that the operation at the minimum frequency clamp is avoided.

The voltage stress over the diode in the secondary S1 was measured separately with the passive probe from Agilent. The measured voltage stress with the maximum input voltages was more than 100 V less than the rated maximum voltage of the diodes with all designs. This safety margin is sufficient for the diodes used in the converters.

4.4 Thermal rise with minimum and maximum input voltages

The thermal rise of the designs was measured with an infrared thermal camera Flir S60 ThermaCAM. The image of the camera was observed in real time and the final image, after the temperatures were stabilized, was saved for determination of the final temperatures. Moreover, the accuracy of the thermal camera is ±2 °C and one celsius should be added to that value to obtain the accuracy of the measurements

because of the variations in the ambient temperature [37]. In addition, emissivities of different surfaces add uncertainty to the measurements. Other equipment, used in the measurement setup, are the presented in Table 23.

The measurement was conducted to the components in the ambient temperature of 23 °C. As a consequence, the results are not directly comparable to the final application because the ambient temperature inside the PV inverter is 65 °C.

The thermal rise of the component is measured using the same setup as for verifying the operation in different operating points without the forced convection of the final application. This results in a higher thermal rise, than in the final appliction, which should be taken into account when evaluating the results. Moreover, only the surface temperatures of the components can be observed with the thermal camera. The hot spot temperature of the windings is in the inner layers of the winding near the air gap.

The measurement was conducted to the components with the specified maximum load currents and with the same minimum and maximum voltages used for verifying the operation in different operating points in 4.3. After the temperature of the component had stabilized, additional 15 minutes were waited until the final images were saved to guarantee that the tempereatures did not increase any more. The images of the thermal camera, presenting the final temperatures of $DCDC34_m$, is shown in Figure 43.

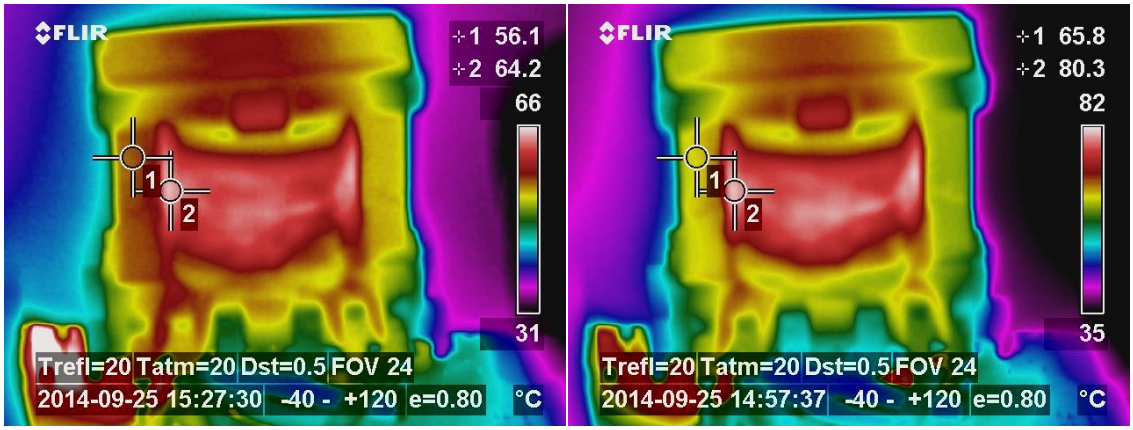

Figure 43: Final temperatures of $DCDC34_m$. Minimum input voltage 240 V on left and 1100 V on right.

The temperatures in the upper right cornes of the images in Figure 43 show the final temperatures of the core and the winding. Moreover, the point presenting where the value is measured is denoted over the component in the images. The number one denotes the temperature of the core and two denotes the winding. In addition, the point denoting the temperature of the winding was always placed on the hottest spot of the winding in all measurements.

The final temperatures of all designs are presented in Table 25.
Table 25 shows that the final temperatures of all designs are higher with the maximum input voltage. This results from the measured increase of the AC resistance,

Table 25: The final temperatures of the components with minimum and maximum input voltages.

Design	V_{Dmin} (V)	T_{Fe} (°C)	T_{Cu} (°C)	V_{Dmax} (V)	T_{Fe} (°C)	T_{Cu} (°C)
DCDC34	240	67	85	1100	85	113
DCDC34_m	240	56	64	1100	66	80
DCDC29	240	67	87	1100	83	111
DCDC29_m	240	68	79	1100	78	91
ACDC29	410	51	55	750	58	63
ACDC29_m	410	50	52	750	56	57

with the higher frequency, as the input voltage is increased. In addition, the losses in the cores increase if the operating frequency is increased, which can be noted from the datasheet of the ferrite material in Figure B3. Moreover, the thermal rise of the windings is higher than the thermal rise of the core in all designs. This results from the lower portion of the core losses if compared to the copper losses.

The effect of the wire type used in windings is clearly notable from the results. In addition, although larger component, the thermal rise of DCDC34 is equal to the smaller DCDC29, which is a result of the higher losses in DCDC34 due to the higher AC resistance. Moreover, the thermal rise of the windings, made of Litz wire, is lower than that of the windings made of single conductors. The difference is not as large between the ACDC designs as it is between the DCDC designs and the both ACDC designs are usable in the final application according to these measurements.

The absolute maximum temperature of the designs is the rated temperature, 130°C, of the insulation tape and insulation of the used TIW. In addition, some marginal should be left to the rated temperature. The thermal rise of the DCDC34_m is the least high of the DCDC designs. Although, if approximately 40°C is added to the saturated temperatures, the temperatures of the other DCDC designs will all exceed 130°C with maximum input voltage in the final application. Furthermore, according to the measured temperatures with the maximum input voltages, the use of single conductors in the windings of DCDC designs will lead to excessive thermal rise in the final application.

The measured thermal rise, of other designs than DCDC34_m, is more than 50°C that was used when calculating the allowed losses in 3.5. This means that the losses are higher in these components than what was calculated in 3.5. In order to lower the thermal rise, a method to reduce the resistance of the windings is to decrease the number of turns of windings. This increases the operating flux density and decreases the value of inductance. Furthermore, this would be more recommendable than decreasing the inductance by increasing the length of air gap, because increasing the air gap length will increase fringing flux and therefore increase losses and thermal rise near the air gap.

Based on the measured final temperatures of Table 25 and the cost breakdowns in 3.8, DCDC34_m and ACDC29 are chosen as the least expensive but usable components in the final application. Nevertheless, the cooling effect of the forced convection, in the final application, should be verified in the future, if the development

of the components should continue.

5 Summary and conclusions

The aim of this thesis was to design flyback transformers for two already existing flyback converters, emphasizing cost efficiency and reliable operation in the designed components. In addition, the operation and parameters of the components were to be verified by measurements in order to be convinced of the designed operation.

As a result, four different components were designed for the DC-to-DC converter and two for the AC-to-DC converter in the third chapter of the thesis. The designing process and calculations were based on the theory presented in the second chapter of the thesis. Furthermore, the differences of the designs were in the sizes of the selected ferrite cores and in the winding wires. Windings made of single conductors were used in half of the designs as the windings of the other half were made using Litz wire.

The costs of the different designs was found to depend on the size of the component and the $\mathrm{DCDC34_m}$ was the most expensive of the designs. Moreover, the difference in the cost to the DCDC34 resulted from the used Litz type TIW, which was found as the most expensive material among all designs, if the relative costs of different materials were compared to the costs of the complete components. On the other hand, Litz type enamelled wire was not more expensive than the enamelled wire of single conductor. In addition, the cost of the $\mathrm{DCDC34_m}$, using Litz type TIW in all windings, was calculated according to the relative costs of TIW. As a result, the relative cost of this component was approximately 292 % of the cost of $\mathrm{DCDC34_m}$.

The measured mutual inductances of the designs matched well the calculated values. The found small differences may result from tolerances originating from the production of the cores. In addition, the values of leakage inductances of the primaries were found to depend on the distance between primaries and secondaries and also on the overall thickness of the windings. Furthermore, the measured values of leakage inductances, in the designed components, were less than 2 % of the mutual inductances.

The results of the measured resistances showed that using Litz type wires in the windings decreases the effects of AC resistance and therefore the amount of copper losses in the components. Furthermore, this was also verified as the lower thermal rises of the components where Litz wire is used, if compared to the equivalent components using single conductors in the windings. In addition, the amount of copper losses was found to be higher than the core losses in the designed components.

All the designs were found to operate close to the designed operating points as part of the intended flyback converter circuits. However, the switching frequency of the DC-to-DC converter was closer to the minimum frequency clamp of the controller than what was expected according to the calculations. As a result, the mutual inductances of the DCDC designs should be decreased by choosing a lower number of turns or by increasing the lengths of air gaps. The former is more recommended over the latter because increasing the length of the air gap will result in higher AC losses and higher thermal rise in the windings near the air gap. In addition, the currents saturating the cores of the flyback transformers were found to be higher

than the measured values of the peak currents. However, the measurement was conducted to the components in a typical room temperature and the saturating currents in the higher operating temperatures should be somewhat lower than the measured values.

As a conclusion, based on the measured results, the designs selected for the auxiliary power supply of the PV inverter are $\mathrm{DCDC34_m}$ and ACDC29. Nonetheless, the testing of the components should be continued in the actual final application, in the PV inverter. Moreover, the properties of the selected components should be tuned in the next iteration round based on the results of this thesis.

References

[1] Dinwoodie, L. Exposing the inner behavior of a quasi-resonant flyback converter. *2012 Texas Instruments Power Supply Design seminar, SEM2000, Topic 3.* Dallas, Texas Instruments Incorporated, 2012. Network document. Cited 21.8.2014. Available: http://www.ti.com/lit/ml/slup302/slup302.pdf

[2] SMA Solar Technology. SMA solar inverters. Network document. Cited 22.7.2014. Available: http://www.sma.de/en/products/solarinverters.html

[3] Remmers, K. *Inverter, storage and PV system technology, Industry guide 2013.* Berlin, Solarpraxis AG, 2013, 93 p.

[4] IEC 61000-3-12. Limits - Limits for harmonic currents produced by equipment connected to public low-voltage systems with input current >16 A and ≤75 A per phase. First edition. Geneva, International Electrotechnical Commission. 2004. 53 p.

[5] BDEW. Technical Guideline, Generating plants connected to the medium-voltage network. Berlin, Bundesverband der Energie- und Wasserwirtschaft e. V. 2008. 130 p.

[6] Mohan, N., Undeland, T. M., Robbins, W. P. *Power electronics: Converters, Applications and Design.* First Edition. New York, John Wiley & Sons, Inc., 1989. 667 p.

[7] Erickson, R., W., Maksimović, D. *Fundamentals of Power Electronics.* Second Edition. New York, Springer Science+Business Media, 2001. 883 p.

[8] IEC 62109-1. Safety of power converters for use in photovoltaic power systems - Part 1: General requirements. First edition. Geneva, International Electrotechnical Commission. 2010. 150 p.

[9] Pressmann, A., I., Billings, K., Morey, T. *Switching power supply design.* Third edition. United States of America, The McGraw-Hill Companies, 2009. 841 p.

[10] Chryssis, G., C. *High-frequency switching power supplies. Theory and design.* Second edition. United States of America, The McGraw-Hill Inc., 1984. 287 p.

[11] Ćuk, S., M. Modelling, analysis, and design of switching converters. Doctoral thesis. Pasadena, California Institute of Technology, 1977. Network document. Cited 14.8.2014. Available: http://thesis.library.caltech.edu/1157/1/Cuk_sm_1977.pdf

[12] Himanshu, K., P. Voltage Transient Spikes Suppression in Flyback Converter using Dissipative Voltage Snubbers. *Industrial Electronics and Applications, 2008. ICIEA 2008. 3rd IEEE Conference on.* Singapore, 3.–5.6.2008. IEEE, 2008, pp. 897–901.

[13] Voncina, D., Petkovsek, M., Nastran, J., Zajec, P. Low power multiple output DC supply - Part I: flyback converter with wide input voltage range. *Power Electronics and Motion Control Conference, 2006. EPE-PEMC 2006. 12th International conference on.* Portoroz, 30.8.–1.9.2006, IEEE, pp. 668–671.

[14] Hu, J., He, Y., Jeoh, M., K., Luo, J., Y. *Application Note, AN-ICE2QS01, Converter design using the quasi-resonant PWM controller ICE2QS01 (ANPS0003).* Version 1.0. Singapore, Infineon Technologies Asia Pacific, 2006. 21 p.

[15] UCC28600 Quasi-resonant flyback controller (Rev. J). Dallas, Texas Instruments, Incorporated, 2011. 24 p. Network document. Cited 28.8.2014. Available: http://www.ti.com/lit/ds/symlink/ucc28600.pdf

[16] Van Den Bossche, A., Valchev, V. *Inductors and transformers for power electronics.* Florida, Taylor & Francis group, 2005. 447 p.

[17] McLyman, W., T. *Transformer and inductor design handbook.* Third Edition. New york, Marcel Dekker, Inc, 2004. 556 p.

[18] Texas instruments, Incorporated. Magnetics Design 5 - Inductor and Flyback Transformer Design. Network document. Cited 12.9.2014. Available: http://www.ti.com/lit/ml/slup127/slup127.pdf

[19] Ferroxcube. Soft ferrites and accessories. 2013 Data handbook. Ferroxcube, international holding B.V. 2013. 1107 p. Network document. Cited 1.9.2014. Available: http://www.ferroxcube.com/FerroxcubeCorporateReception/datasheet/FXC_HB2013.pdf

[20] Chalermyanont, K., Sangampai, P., Prasertsit, A., Theinmontri, S. High frequency transformer designs for improving cross regulation in multiple-output flyback converters. *Power electronics and drive systems, 2007. PEDS '07. 7th international conference on.* Bangkok, 27.–30.11.2007. IEEE, pp. 53–56.

[21] Prieto, R., Cobos, J., A., Garcia, O., Asensi, R., Uceda, J. Optimizing the winding strategy of the transformer in a flyback converter. *Power Electronics Specialists Conference, 1996. PESC '96 Record., 27th Annual IEEE (Volume 2).* Baveno, 23.–27.6.1996. IEEE, pp. 1456–1462.

[22] DMEGC. Material grades correspond. Network document. Cited 10.10.2014. Available: http://www.chinadmegc.com/en/pdf/guige.pdf

[23] DMEGC. DMR40 Material Datasheet. Network document. Cited 10.10.2014. Available: http://www.chinadmegc.com/en/material_download.php?6

[24] TDG Holding Co., Ltd. 2006 Mn-Zn soft ferrite cores. Network document. Cited 10.10.2014. Available: http://www.mhw-intl.com/assets/TDG/TDG%202006%20MnZn%20Catalog.pdf

[25] Roshen, W. Ferrite core loss for power magnetic components design. *IEEE transctions on magnetics.* 1991, vol. 27, issue 6, pp. 4407–4415.

[26] Murthy-Bellur, D., Kazimierczuk, M., K. Winding losses caused by harmonics in high-frequency flyback transformers for pulse-width modulated dc-dc converters in discontinuous conduction mode. *IET Power electronics.* 2010, vol. 3, issue 5, pp. 804–817.

[27] Vandelac, J., Ziogas, P., D. A novel approach for minimizing high-frequency transformer copper losses. *IEEE transactions on power electronics.* 1988, vol. 3, issue 3, pp. 266–277.

[28] Sullivan, C., R. Optimal choice for number of strands in a Litz-wire transformer winding. *IEEE transactions on power electronics.* 1999, vol. 14, issue 2, pp. 283–291.

[29] Choi, H., S. *AN-4140 Transformer design consideration for offline flyback converters using Fairchild power switch (FPS).* Version 1.0.0 Fairchield Semiconductor Corporation, 2003. 10 p. Network document. Cited 21.10.2014. Available: Network document. Cited 21.10.2014. Available: http://www.fairchildsemi.com/application-notes/AN/AN-4140.pdf

[30] Adams, J. *Application note AN-1024 Flyback transformer design for the IRIS40xx series.* International rectifier, 2001. 18 p. Network document. Cited 21.10.2014. Available: http://www.irf.com/technical-info/appnotes/an-1024.pdf

[31] STMicroelectronics. STFW3N150, STH3N150-2, STP3N150, STW3N150 N-channel 1500 V, 2.5 A, 6 Ω typ., PowerMESHTM Power MOSFETs in TO-3PF, H^2PAK-2, TO-220 and TO247 packages. STMicroelectronics. 2014. 23 p. Network document. Cited 24.10.2014. Available: http://www.st.com/web/en/resource/technical/document/datasheet/CD00149569.pdf

[32] Agilent Technologies, Inc. Agilent impedance measurement handbook. A guide to measurement technology and techniques. 4th Edition. Network document. Cited 10.11.2014 Available: http://cp.literature.agilent.com/litweb/pdf/5950-3000.pdf

[33] Ridley, R. Frequency response measurements for switching power supplies. Texas Instruments Inc. 2001. 13 p. Network document. Cited 10.11.2014. Available: http://www.ti.com/lit/ml/slup121/slup121.pdf

[34] Agilent Technologies, Inc. Agilent 4294A Precision Impedance Analyzer Data Sheet. Network document. Cited 11.11.2014 Available: http://literature.cdn.keysight.com/litweb/pdf/5968-3809E.pdf

[35] e-dk electronics development. Power choke tester DPG-10 series Description and technical specifications. 2014. Network document. Cited 13.11.2014. Available: http://www.powerchoketester.com/media/Dokumente/Inductance_measurement_instrument_DPG10-series_1401.pdf

[36] Tektronix, Inc. Mixed Signal Oscilloscopes MSO4000B, DPO4000B Series Datasheet. 2014. Network document. Cited 14.11.2014. Available: http://www.tek.com/datasheet/mso4000-dpo4000/mso4000b-dpo4000b-series-datasheet-0

[37] ThermaCAM S60 käyttäjän käsikirja. Revision a35. Flir Systems. 2004. 176 p.

A Appendix

In appendix A, tables from [8] are shown for determining DVC, temporary overvoltages and clearance and creepage distances.

The table for determining DVCs is presented in the figure A1.

Decisive voltage Classification (DVC)	Limits of working voltage V		
	a.c. voltage r.m.s. U_{ACL}	a.c. voltage peak U_{ACPL}	d.c. voltage mean U_{DCL}
A*	≤25 (16)	≤35,4 (22,6)	≤60 (35)
B	50 (33)	71 (46,7)	120 (70)
C	>50 (>33)	>71 (>46,7)	>120 (>70)

Figure A1: Table for determining DVC [8, p. 49].

The table for determining insulation voltages is presented in the figure A2.

Column 1	2	3	4	5	6
System voltage (7.3.7.2) V	Impulse withstand voltage V				Mains circuit Temporary overvoltage (peak / r.m.s.) (see note 5) V
	Overvoltage category				
	I	II	III	IV	
50 V rms or 71 V dc	330	500	800	1 500	1 770 / 1 250
100 V rms or 141 V dc	500	800	1 500	2 500	1 840 / 1 300
150 V rms or 213 V dc	800	1 500	2 500	4 000	1 910 / 1 350
300 V rms or 424 V dc	1 500	2 500	4 000	6 000	2 120 / 1 500
600 V rms or 849 V dc	2 500	4 000	6 000	8 000	2 550 / 1 800
1 000 V rms or 1 500 V dc	4 000	6 000	8 000	12 000	3 110 / 2 200

Figure A2: Table for determining impulse withstand voltage and temporary overvoltage [8, p. 71].

In the figure A2, linear interpolation between rows is forbidden for circuits connected to grid but is permitted for PV circuits.

Tables for designing clearance and creepage distances are presented in the figures A3 and A4.

Column 1	2	3	4	5	6
Impulse voltage (Table 12 and 7.3.7.1.4)	Temporary overvoltage (peak value) for determining insulation between circuits and their surroundings or Working voltage (recurring peak) for determining functional insulation	Working voltage (recurring peak) for determining insulation between circuits and their surroundings	Minimum clearance mm		
			Pollution degree		
V	V	V	1	2	3
500	530	330	0,04	0,20	0,80
800	700	440	0,10	0,20	0,80
1 500	960	600	0,50	0,50	0,80
2 500	1 600	1 000	1,5		
4 000	2 600	1 600	3,0		
6 000	3 700	2 300	5,5		
8 000	4 800	3 000	8,0		
12 000	7 400	4 600	14,0		

Figure A3: Table for designing clearances [8, p. 73].

In the figure A3, linear interpolation is permitted between rows.

Column 1	2	3	4	5	6	7	8	9	10	11	12
RMS Working Voltage (7.3.7.5.2)	PWBs [a] Pollution degree		Other insulators Pollution degree								
	1	2	1	2				3			
				Insulating material group				Insulating material group			
V	[b]	[c]	[b]	I	II	IIIa	IIIb	I	II	IIIa	IIIb
400	1,0	2,0	1,0	2,0	2,8	4,0		5,0	5,6	6,3	
500	1,3	2,5	1,3	2,5	3,6	5,0		6,3	7,1	8,0	
630	1,8	3,2	1,8	3,2	4,5	6,3		8,0	9,0	10,0	
800	2,4	4,0	2,4	4,0	5,6	8,0		10,0	11	12,5	[d]
1 000	3,2	5,0	3,2	5,0	7,1	10,0		12,5	14	16	
1 250	4,2	6,3	4,2	6,3	9	12,5		16	18	20	
1 600	[e]	[e]	5,6	8,0	11	16		20	22	25	
2 000			7,5	10,0	14	20		25	28	32	
2 500			10,0	12,5	18	25		32	36	40	
3 200			12,5	16	22	32		40	45	50	
4 000			16	20	28	40		50	56	63	
5 000			20	25	36	50		63	71	80	
6 300			25	32	45	63		80	90	100	
8 000			32	40	56	81		100	110	125	
10 000			40	50	71	100		125	140	160	

Figure A4: Table for designing creepage distances [8, p. 75].

In the figure A4, linear interpolation is permitted between rows.

B Appendix

The datasheets of ferrite materials 3C30 from Ferroxcube, DMR40 from DMEGC and TP4 from TDG are presented in Appendix B. The datasheets are provided by the manufacturers of cores.

SYMBOL	CONDITIONS	VALUE	UNIT
μ_i	25 °C; ≤10 kHz; 0.25 mT	2100 ±20%	
μ_a	100 °C; 25 kHz; 200 mT	5000 ±25%	
B	25 °C; 10 kHz; 1200 A/m	≈ 500	mT
	100 °C; 10 kHz; 1200 A/m	≈ 440	
P_V	100 °C; 25 kHz; 200 mT	≤ 80	kW/m^3
	100 °C; 100 kHz; 100 mT	≤ 80	
	100 °C; 100 kHz; 200 mT	≈ 450	
ρ	DC; 25 °C	≈ 2	Ωm
T_C		≥ 240	°C
density		≈ 4800	kg/m^3

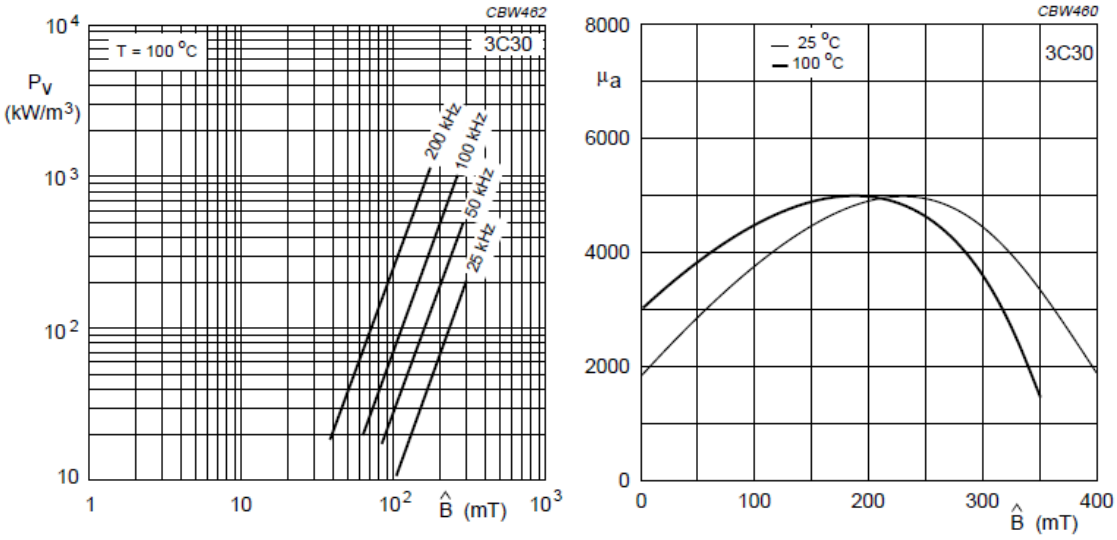

Figure B1: Ferroxcube 3C30 Mn-Zn ferrite material. [19, p. 78-79.]

特性 SYMBOL	测试条件 CONDITIONS		典型值 VALUE
初始磁导率 μ_i Initial permeability	10kHz,B<0.25mT	25℃	2300 ± 25%
饱和磁通密度Bs (mT) Saturation flux density	50Hz, 1194A/m	25℃	510
		100℃	390
剩磁 Br(mT) Residual magnetic flux density		25℃	95
		100℃	55
矫顽力Hc （A/m） Coercive force		25℃	14
		100℃	9
功耗pv(mw/cm^3) Power loss	100kHz, 200mT	25℃	600
		60℃	450
		100℃	410
		120℃	500
居里温度Tc (℃) Curie temperature	10kHz,B<0.25mT		> 215
电阻率 ρ (Ω・m) Resistivity		25℃	6.5
密度d(g/cm^3) Density		25℃	4.8

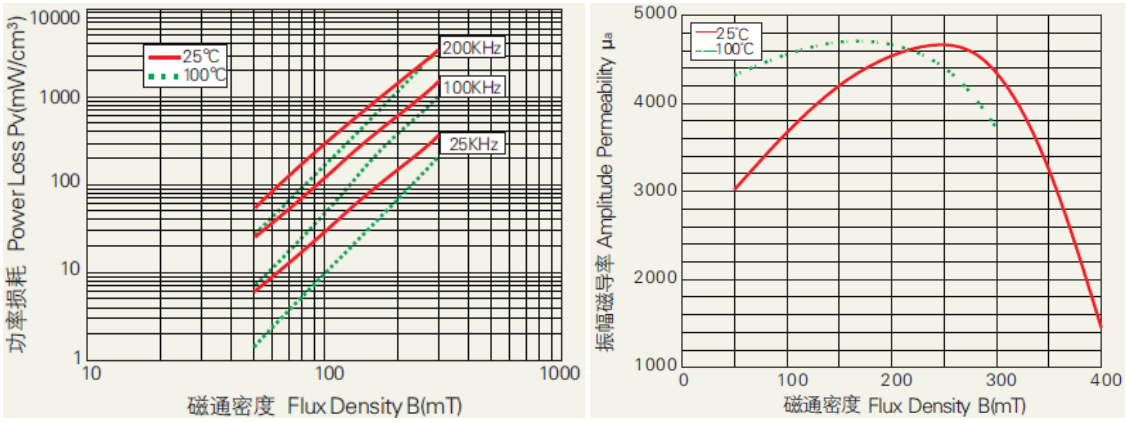

Figure B2: DMEGC DMR40 Mn-Zn ferrite material. [23]

Initial permeability	μ_i	25℃	2300±25%
Saturation magnetic flux density	Bs(mT)	25℃	510
	1194A/m	100℃	390
Remanence	Br(mT)	25℃	100
		100℃	55
Coercivity	Hc(A/m)	25℃	14
		100℃	9
Core loss	Pcv(kW/m^3)	25℃	650
	100kHz 200mT	100℃	410
		120℃	500
Curie temperature	Tc(℃)		≥220
Electrial resistivity	ρ (Ω • m)		6.5
Density	d(kg/m^3)		4.8×10^3

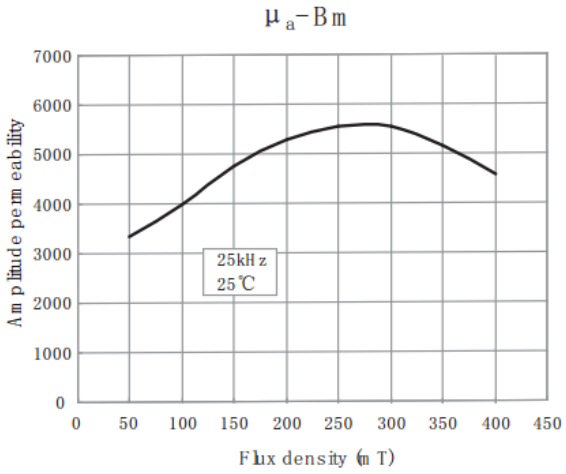

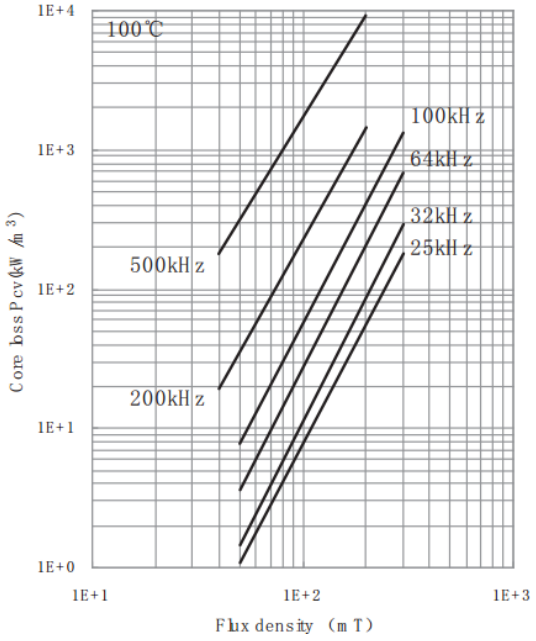

Figure B3: TDG TP4 Mn-Zn ferrite material. [24, p. 24-25.]

C Appendix

Calculations of the designs, using initial and chosen values, are presented in Appendix C.

Turns ratios and inductances

DCDC:

First iteration

$$\begin{aligned}
t_{on} &= \frac{D_{max}}{f_{sw}} = \frac{0.44}{45\text{kHz}} = 9.78\ \mu\text{s} \\
L &= \frac{V_D^2 t_{on}^2 f_{sw}}{2(V_O + v_F) I_O} = \frac{240^2\text{V}(9.78\mu\text{s})^2\ 45\text{kHz}}{2(24\text{V} + 1\text{V})3\text{A}} \\
L &\approx 1.65\text{mH} \\
i_{Ppk} &= \frac{V_D t_{on}}{L} = \frac{240\text{V} * 9.78\mu\text{s}}{1.65\text{mH}} \approx 1.42\ \text{A} \\
i_{P,rms} &= i_{Ppk}\sqrt{\frac{D_{max}}{3}} = 1.42\text{A}\sqrt{\frac{0.44}{3}} = 0.54\ \text{A}
\end{aligned}$$

Second iteration

$$\begin{aligned}
t_{res} &= \pi\sqrt{LC_{DS}} = \pi\sqrt{1.65\text{mH} * 100\text{pF}} \approx 1.28\ \mu\text{s} \\
D_{res} &= t_{res} f_{sw} = 1.28\mu\text{s} * 45\text{kHz} \approx 0.06 \\
v_{drop} &\approx (2 * R_{DS,on} + R) * i_{P,rms} = (2 * 6\Omega + 1\ \Omega) * 0.54\text{A} \approx 7\ \text{V} \\
N_{PS} &= \frac{D_{max}}{1 - D_{max} - D_{res}} \frac{V_D - v_{drop}}{V_O + v_F} = \frac{0.43}{1 - 0.43 - 0.06} * \frac{240\text{V} - 7\text{V}}{24\ \text{V} + 1\text{V}} \\
N_{PS} &\approx 7.86 \\
t_{on} &= \frac{N_{PS}(V_O + v_F)(T_S - t_{res})}{V_D - v_{drop} + N_{PS}(V_O + v_F)} = \frac{7.86(24\text{V} + 1\ \text{V})(\frac{1}{45\text{kHz}} - 1.28\mu\text{s})}{240\text{V} - 7\text{V} + 7.86(24\text{V} + 1\text{V})} \\
t_{on} &\approx 9.58\ \mu\text{s} \\
D_{on} &= t_{on} * f_{sw} = 9.58\mu\text{s} * 45\text{kHz} \approx 0.43 \\
L &= \frac{(V_D - v_{drop})^2 t_{on}^2 f_{sw}}{2(V_O + v_F) I_O} = \frac{(240\text{V} - 7\text{V})^2(9.58\mu\text{s})^2\ 45\text{kHz}}{2(24\text{V} + 1\ \text{V})3\ \text{A}} \\
L &\approx 1.49\ \text{mH} \\
i_{Ppk} &= \frac{(V_D - v_{drop}) t_{on}}{L} = \frac{(240\text{V} - 7\text{V}) * 9.58\mu\text{s}}{1.49\text{mH}} \approx 1.50\ \text{A} \\
i_{P,rms} &= i_{Ppk}\sqrt{\frac{D_{max}}{3}} = 1.50\text{A}\sqrt{\frac{0.43}{3}} \approx 0.57\ \text{A}
\end{aligned}$$

ACDC:

First iteration

$$\begin{aligned}
v_{rating} &= V_D + v_r + v_{spike} + 0.3 * V_D = V_D + N_{PS}(V_O + v_F) + 0.6 * V_D \\
N_{PS} &= \frac{v_{rating} - V_D - 0.6 * V_D}{V_O + v_F} = \frac{1500\ \text{V} - 390\text{V} - 0.6 * 806\text{V}}{24\text{V} + 1\text{V}} \\
N_{PS} &\approx 8.42
\end{aligned}$$

$$
\begin{aligned}
t_{on} &= \frac{N_{PS}(V_O + v_F)(T_S - t_{res})}{V_D + N_{PS}(V_O + v_F)} = \frac{8.42(24\text{V} + 1\text{ V})(\frac{1}{100\text{kHz}} - 500\text{ns})}{390\text{V} + 8.42(24\text{V} + 1\text{V})} \\
t_{on} &\approx 3.33\ \mu\text{s} \\
L &= \frac{V_D^2 t_{on}^2 f_{sw}}{2(V_O + v_F)I_O} = \frac{(390\text{V})^2(3.33\mu\text{s})^2 100\text{kHz}}{2(24\text{V} + 1\text{V})0.86\text{A}} \\
L &\approx 3.92\text{ mH}
\end{aligned}
$$

Second iteration

$$
\begin{aligned}
t_{res} &= \pi\sqrt{LC_{DS}} = \pi\sqrt{3.92\text{mH} * 100\text{pF}} \approx 1.97\ \mu\text{s} \\
t_{on} &= \frac{N_{PS}(V_O + v_F)(T_S - D_{res})}{V_D + N_{PS}(V_O + v_F)} = \frac{8.42(24\text{V} + 1\text{ V})(\frac{1}{100\text{kHz}} - 1.97\mu\text{s})}{390\text{V} + 8.42(24\text{V} + 1\text{V})} \\
t_{on} &\approx 2.81\ \mu\text{s} \\
D_{on} &= t_{on} * f_{sw} = 2.81\mu\text{s} * 100\text{kHz} \approx 0.28 \\
L &= \frac{V_D^2 t_{on}^2 f_{sw}}{2(V_O + v_F)I_O} = \frac{(390\text{V})^2(2.81\mu\text{s})^2 100\text{kHz}}{2(24\text{ V} + 1\text{ V})0.86\text{A}} \approx 2.79\text{ mH} \\
i_{Ppk} &= \frac{V_D t_{on}}{L} = \frac{390\text{V} * 2.81\mu\text{s}}{2.79\text{mH}} \approx 0.39\text{ A} \\
i_{P,rms} &= i_{Ppk}\sqrt{\frac{t_{on} f_{sw}}{3}} = 0.39\text{A}\sqrt{\frac{2.81\mu\text{s } 100\text{kHz}}{3}} = 0.12\text{ A} \\
v_{drop} &\approx (R_{DS,on} + R) * i_{P,rms} = (6\Omega + 1\Omega) * 0.12\text{A} = 0.84\text{ V}
\end{aligned}
$$

Initial energy throughput of the flyback transformers
DCDC:

$$E = i_{Ppk}^2 L = (1.50\text{A})^2 * 1.49\text{mH} \approx 3.35\text{ mJ}$$

ACDC:

$$E = i_{Ppk}^2 L = (0.39\text{A})^2 * 2.79\text{mH} = \approx 0.42\text{ mJ}$$

Number of turns, air gap length and actual mutual inductance
DCDC34:

$$
\begin{aligned}
N &= \frac{(V_D - v_{drop})t_{on}}{\Delta B * A_c} = \frac{(240\text{V} - 7\text{V})9.58\mu\text{s}}{0.25\text{T} * 0.971\text{cm}^2} \approx 91.6 \\
N_{AUX} &= \frac{N_P}{N} = \frac{v_r}{v_{AUX}} = \frac{7.67 * 25\text{V}}{19\text{V}} \approx 10.1 \\
N &= \frac{N_P}{N_{AUX}} = \frac{92}{10.1} \approx 9.1 \\
N_{AUX} &= \frac{92}{9} \approx 10.2 \\
L_M &= FL = \left(1 + \frac{l_g}{\sqrt{A_c}}\ln\frac{2G}{l_g}\right)\frac{\mu_0 N^2 A_c * 10^{-2}}{l_g + \frac{l_c}{\mu_i}} \\
L_M &= \left(1 + \frac{0.1\text{cm}}{\sqrt{0.971\text{cm}^2}}\ln\frac{2 * 2.36\text{cm}}{0.1\text{cm}}\right)\frac{1.26\text{H/m} * 92^2 * 0.971\text{cm}^2 * 10^{-8}}{0.1\text{cm} + \frac{7.86\text{cm}}{2300}}
\end{aligned}
$$

$$
\begin{aligned}
L_M &\approx 1.39 \text{ mH} \\
f_{sw} &= \frac{(V_D - v_{drop})^2 D_{on}^2}{2 * (V_O + v_F) * I_O * L} = \frac{(240\text{V} - 7\text{V})^2 * 0.43^2}{2 * (24\text{V} + 1\text{V}) * 3\text{A} * 1.39\text{mH}} \approx 48 \text{ kHz} \\
t_{res} &= \pi\sqrt{LC_{DS}} = \pi\sqrt{1.39\text{mH} * 100\text{pF}} \approx 1.17 \ \mu\text{s} \\
D_{res} &= t_{res} f_{sw} = 1.17\mu\text{s} * 48\text{kHz} \approx 0.06 \\
t_{on} &= \frac{N_{PS}(V_O + v_F)(T_S - D_{res})}{V_D - v_{drop} + N_{PS}(V_O + v_F)} = \frac{7.67(24\text{V} + 1 \text{ V})(\frac{1}{48\text{kHz}} - 1.17\mu\text{s})}{240\text{V} - 7\text{V} + 7.86(24\text{V} + 1\text{V})} \\
t_{on} &\approx 8.88 \ \mu\text{s} \\
D_{on} &= t_{on} * f_{sw} = 8.88\mu\text{s} * 48\text{kHz} \approx 0.43 \\
i_{Ppk} &= \frac{(V_D - v_{drop}) t_{on}}{L} = \frac{(240\text{V} - 7\text{V}) * 8.88\mu\text{s}}{1.39\text{mH}} \approx 1.49 \text{ A} \\
i_{P,rms} &= i_{Ppk}\sqrt{\frac{D_{on}}{3}} = 1.49\text{A}\sqrt{\frac{0.43}{3}} = 0.56 \text{ A} \\
\Delta B &= \frac{(V_D - v_{drop}) t_{on}}{N_P * A_c} = \frac{(240\text{V} - 7\text{V}) 8.88\mu\text{s}}{92 * 0.971\text{cm}^2} \approx 0.23 \text{ T}
\end{aligned}
$$

DCDC29:

$$
\begin{aligned}
N &= \frac{(V_D - v_{drop}) t_{on}}{\Delta B * A_c} = \frac{(240\text{V} - 7\text{V}) 9.58\mu\text{s}}{0.25\text{T} * 0.768\text{cm}^2} \approx 116.2 \\
L_M &= FL = \left(1 + \frac{l_g}{\sqrt{A_c}} \ln \frac{2G}{l_g}\right) \frac{\mu_0 N^2 A_c * 10^{-2}}{l_g + \frac{l_c}{\mu_i}} \\
L_M &= \left(1 + \frac{0.08\text{cm}}{\sqrt{0.768\text{cm}^2}} \ln \frac{2 * 2.2\text{cm}}{0.08\text{cm}}\right) \frac{1.26\text{H/m} * 92^2 * 0.768\text{cm}^2 * 10^{-8}}{0.08\text{cm} + \frac{7.2\text{cm}}{2300}} \\
L_M &\approx 1.39 \text{ mH} \\
f_{sw} &= \frac{(V_D - v_{drop})^2 D_{on}^2}{2 * (V_O + v_F) * I_O * L} = \frac{(240\text{V} - 7\text{V})^2 * 0.43^2}{2 * (24\text{V} + 1\text{V}) * 3\text{A} * 1.35\text{mH}} \approx 50 \text{ kHz} \\
t_{res} &= \pi\sqrt{LC_{DS}} = \pi\sqrt{1.35\text{mH} * 100\text{pF}} \approx 1.15 \ \mu\text{s} \\
D_{res} &= t_{res} f_{sw} = 1.15\mu\text{s} * 50\text{kHz} \approx 0.06 \\
t_{on} &= \frac{N_{PS}(V_O + v_F)(T_S - D_{res})}{V_D - v_{drop} + N_{PS}(V_O + v_F)} = \frac{7.67(24\text{V} + 1 \text{ V})(\frac{1}{50\text{kHz}} - 1.15\mu\text{s})}{240\text{V} - 7\text{V} + 7.67(24\text{V} + 1\text{V})} \\
t_{on} &\approx 8.51 \ \mu\text{s} \\
D_{on} &= t_{on} * f_{sw} = 8.51\mu\text{s} * 50\text{kHz} \approx 0.43 \\
i_{Ppk} &= \frac{(V_D - v_{drop}) t_{on}}{L} = \frac{(240\text{V} - 7\text{V}) * 8.51\mu\text{s}}{1.35\text{mH}} \approx 1.47 \text{ A} \\
i_{P,rms} &= i_{Ppk}\sqrt{\frac{D_{on}}{3}} = 1.47\text{A}\sqrt{\frac{0.43}{3}} = 0.56 \text{ A} \\
\Delta B &= \frac{(V_D - v_{drop}) t_{on}}{N_P * A_c} = \frac{(240\text{V} - 7\text{V}) 8.51\mu\text{s}}{92 * 0.768\text{cm}^2} \approx 0.28 \text{ T}
\end{aligned}
$$

ACDC:

$$
N = \frac{V_D t_{on}}{\Delta B * A_c} = \frac{390\text{V} * 2.81\mu\text{s}}{0.25\text{T} * 0.768\text{cm}^2} \approx 57.1
$$

$$
\begin{aligned}
L_M &= FL = \left(1 + \frac{l_g}{\sqrt{A_c}} \ln \frac{2G}{l_g}\right) \frac{\mu_0 N^2 A_c * 10^{-2}}{l_g + \frac{l_c}{\mu_i}} \\
L_M &= \left(1 + \frac{0.03\text{cm}}{\sqrt{0.768\text{cm}^2}} \ln \frac{2 * 2.2\text{cm}}{0.03\text{cm}}\right) \frac{1.26\text{H/m} * 57^2 * 0.768\text{cm}^2 * 10^{-8}}{0.03\text{cm} + \frac{7.2\text{cm}}{2300}} \\
L_M &\approx 1.11 \text{ mH} \\
L_M &= \left(1 + \frac{0.03\text{cm}}{\sqrt{0.768\text{cm}^2}} \ln \frac{2 * 2.2\text{cm}}{0.03\text{cm}}\right) \frac{1.26\text{H/m} * 88^2 * 0.768\text{cm}^2 * 10^{-8}}{0.03\text{cm} + \frac{7.2\text{cm}}{2300}} \\
L_M &\approx 2.65 \text{ mH} \\
N_{AUX} &= \frac{N_P}{N} = \frac{v_r}{v_{AUX}} = \frac{8 * 25\text{V}}{19\text{V}} \approx 10.5 \\
N &= \frac{N_P}{N_{AUX}} = \frac{88}{10.5} \approx 8.4 \\
N_{AUX} &= \frac{88}{8} = 11 \\
V_{AUX} &\approx \frac{v_r}{N_{AUX}} = \frac{8 * 25\text{V}}{11} \approx 18.2 \text{ V} \\
t_{res} &= \pi \sqrt{LC_{DS}} = \pi \sqrt{2.65\text{mH} * 100\text{pF}} \approx 1.62 \ \mu\text{s} \\
t_{on} &= \frac{N_{PS}(V_O + v_F)(T_S - D_{res})}{V_D + N_{PS}(V_O + v_F)} = \frac{8(24\text{V} + 1 \text{ V})(\frac{1}{100\text{kHz}} - 1.62\mu\text{s})}{390\text{V} + 8(24\text{V} + 1\text{V})} \\
t_{on} &\approx 2.84 \ \mu\text{s} \\
D_{on} &= t_{on} * f_{sw} = 2.84\mu\text{s} * 100\text{kHz} \approx 0.29 \\
i_{Ppk} &= \frac{V_D t_{on}}{L} = \frac{390\text{V} * 2.84\mu\text{s}}{2.65\text{mH}} \approx 0.42 \text{ A} \\
i_{P,rms} &= i_{Ppk} \sqrt{\frac{D_{on}}{3}} = 0.42\text{A} \sqrt{\frac{0.29}{3}} = 0.13 \text{ A} \\
\Delta B &= \frac{(V_D - v_{drop}) t_{on}}{N_P * A_c} = \frac{390\text{V} 2.84\mu\text{s}}{88 * 0.768\text{cm}^2} \approx 0.16 \text{ T}
\end{aligned}
$$

Cooling surface area and allowed losses
ETD34:

$$
\begin{aligned}
A_1 &\approx 2X(W + Z) = 2 * 1.1\text{cm} * (3.5\text{cm} + 3.46\text{cm}) \approx 15.3 \text{ cm}^2 \\
A_2 &\approx 4YW = 4 * 0.55\text{cm} * 3.5\text{cm} \approx 7.7 \text{ cm}^2 \\
A_3 &\approx 4Y(Z - 2Y) = 4 * 0.55\text{cm}(3.46\text{cm} - 2 * 0.55\text{cm}) \approx 5.2 \text{ cm}^2 \\
A_4 &\approx 2\pi \left(\frac{W - 2Y}{2}\right)(Z - 2Y) - 2X(Z - 2Y) \\
A_4 &\approx 2\pi \left(\frac{3.5\text{cm} - 2 * 0.55\text{cm}}{2}\right)(3.46\text{cm} - 2 * 0.55\text{cm}) - \\
&\quad 2 * 1.1\text{cm}(3.46\text{cm} - 2 * 0.55\text{cm}) \approx 12.6 \text{ cm}^2 \\
A_5 &\approx 2\pi \left(\frac{W - 2Y}{2}\right)^2 - 2X(W - 2Y)
\end{aligned}
$$

$$
\begin{aligned}
A_5 &\approx 2\pi\left(\frac{3.5\text{cm}-2*0.55\text{cm}}{2}\right)^2 - 2*1.1\text{cm}(3.5\text{cm}-2*0.55\text{cm}) \approx 3.8\ \text{cm}^2\\
A &= A_1+A_2+A_3+A_4+A_5\\
A &\approx 15.3\text{cm}^2+7.7\text{cm}^2+5.2\text{cm}^2+12.6\text{cm}^2+3.8\text{cm}^2 = 44.6\ \text{cm}^2\\
P_{loss} &= \Delta T^{1.1}A = 50^\circ\text{C}^{1.1}44.6\text{cm}^2 \approx 3298\ \text{mW}
\end{aligned}
$$

ETD29:

$$
\begin{aligned}
A_1 &\approx 2X(W+Z) = 2*0.98\text{cm}*(3.06\text{cm}+3.16\text{cm}) \approx 12.2\ \text{cm}^2\\
A_2 &\approx 4YW = 4*0.50\text{cm}*3.06\text{cm} \approx 6.1\ \text{cm}^2\\
A_3 &\approx 4Y(Z-2Y) = 4*0.50\text{cm}(3.16\text{cm}-2*0.50\text{cm}) \approx 4.3\text{cm}^2\\
A_4 &\approx 2\pi\left(\frac{W-2Y}{2}\right)(Z-2Y) - 2X(Z-2Y)\\
A_4 &\approx 2\pi\left(\frac{3.06\text{cm}-2*0.50\text{cm}}{2}\right)(3.16\text{cm}-2*0.50\text{cm}) -\\
&\quad 2*0.98\text{cm}(3.16\text{cm}-2*0.50\text{cm}) \approx 9.77\ \text{cm}^2\\
A_5 &\approx 2\pi\left(\frac{W-2Y}{2}\right)^2 - 2X(W-2Y)\\
A_5 &\approx 2\pi\left(\frac{3.06\text{cm}-2*0.50\text{cm}}{2}\right)^2 - 2*0.98\text{cm}(3.06\text{cm}-2*0.50\text{cm}) \approx 2.6\ \text{cm}^2\\
A &= A_1+A_2+A_3+A_4+A_5\\
A &\approx 12.2\text{cm}^2+6.1\text{cm}^2+4.3\text{cm}^2+9.77\text{cm}^2+2.6\text{cm}^2 = 35.0\ \text{cm}^2\\
P_{loss} &= \Delta T^{1.1}A = 50^\circ\text{C}^{1.1}35.0\text{cm}^2 \approx 2588\ \text{mW}
\end{aligned}
$$

Calculated flux densities, core losses and copper losses

DCDC34:

$$
\begin{aligned}
\Delta B &= \frac{(V_D-v_{drop})t_{on}}{N_P A_c} = \frac{(240\text{V}-7\text{V})8.88\mu\text{s}}{92*0.971\text{cm}^2} \approx 0.23\ \text{T}\\
V_e &= L_c*A_c = 7.86\text{cm}*0.971\text{cm}^2 \approx 7.63\ \text{cm}^3\\
P_{Fe} &= \rho_{Fe}*V_e = 24\text{W/cm}^3*7.63\text{cm}^3 \approx 180\ \text{mW}\\
P_{Cu} &= P_{loss}-P_{Fe} = 3298\text{mW}-180\text{mW} \approx 3.1\ \text{W}
\end{aligned}
$$

DCDC29:

$$
\begin{aligned}
\Delta B &= \frac{(V_D-v_{drop})t_{on}}{N_P A_c} = \frac{(240\text{V}-7\text{V})8.51\mu\text{s}}{92*0.768\text{cm}^2} \approx 0.28\ \text{T}\\
V_e &= L_c*A_c = 7.20\text{cm}*0.768\text{cm}^2 \approx 5.53\ \text{cm}^3\\
P_{Fe} &= \rho_{Fe}*V_e = 24\text{W/cm}^3*5.53\text{cm}^3 \approx 240\ \text{mW}\\
P_{Cu} &= P_{loss}-P_{Fe} = 2588\text{mW}-240\text{mW} \approx 2.3\ \text{W}
\end{aligned}
$$

ACDC29:

$$
\Delta B = \frac{V_D t_{on}}{N_P A_c} = \frac{390\text{V}*8.51\mu\text{s}}{88*0.768\text{cm}^2} \approx 0.16\ \text{T}
$$

$$
\begin{aligned}
V_e &= L_c * A_c = 7.20\text{cm} * 0.768\text{cm}^2 \approx 5.53\ \text{cm}^3 \\
P_{Fe} &= \rho_{Fe} * V_e = 32\text{W/cm}^3 * 5.53\text{cm}^3 \approx 180\ \text{mW} \\
P_{Cu} &= P_{loss} - P_{Fe} = 2588\text{mW} - 180\text{mW} \approx 2.4\ \text{W}
\end{aligned}
$$

Clearance and creepage distances
Interpolation of the impulse withstand voltage:
From figure A2

$$\begin{aligned}
\tan(\theta) &= \frac{6000\text{V} - 4000\text{V}}{1500\text{V} - 849\text{V}} \\
v_{impulse} &= 4000\text{V} + (1100\text{V} - 849\text{V})\tan(\theta) \\
&= 4000\text{V} + (1100\text{V} - 849\text{V})\frac{6000\text{V} - 4000\text{V}}{1500\text{V} - 849\text{V}} \\
&\approx 4771\text{ V}
\end{aligned}$$

Interpolation of the clearance:
From figure A3

$$\begin{aligned}
\tan(\theta) &= \frac{5.5\text{mm} - 3\text{mm}}{6000\text{V} - 4000\text{V}} \\
Clearance &= 3\text{mm} + (4771\text{V} - 4000\text{V})\tan(\theta) \\
&= 3\text{mm} + 771\text{V}\frac{5.5\text{mm} - 3\text{mm}}{6000\text{V} - 4000\text{V}} \\
&\approx 4\text{ mm}
\end{aligned}$$

Interpolation of the creepage:
From figure A4

$$\begin{aligned}
\tan\theta &= \frac{6.3\text{mm} - 5.0\text{mm}}{1250\text{V} - 1000\text{V}} \\
Creepage &= 5.0\text{mm} + (1100\text{V} - 1000\text{V})\tan(\theta) \\
&= 5\text{mm} + 100\text{V}\frac{6.3\text{mm} - 5.0\text{mm}}{1250\text{V} - 1000\text{V}} \\
&\approx 5.5\text{ mm}
\end{aligned}$$

Rms values of currents
DCDC34:

$$\begin{aligned}
i_{P,rms} &= i_{Ppk}\sqrt{\frac{D_{on}}{3}} = 1.49\text{A}\sqrt{\frac{8.88\mu\text{s} * 48\text{kHz}}{3}} = 0.57\text{ A} \\
t_{off} &= \frac{1}{48\text{kHz}} - 8.88\mu\text{s} - 1.17\mu\text{s} \approx 10.8\ \mu\text{s} \\
i_{Spk} &= N_{PS}^2\frac{(V_O + v_F)t_{off}}{L} = 7.67^2\frac{(24\text{V} + 1\text{V})10.8\mu\text{s}}{1.39\text{mH}} \approx 11.4\text{ A} \\
i_{S,rms} &= i_{Spk}\sqrt{\frac{D_{off}}{3}} = 11.4\text{A}\sqrt{\frac{10.8\mu\text{s} * 48\text{kHz}}{3}} \approx 4.7\text{ A} \\
i_{S1,rms} &= \frac{I_{O1}}{I_{O1} + I_{O2}}i_{S,rms} = \frac{1.8\text{A}}{1.8\text{A} + 1.2\text{A}}4.7\text{A} \approx 2.8\text{ A} \\
i_{S2,rms} &= i_{S,rms} - i_{S1,rms} = 4.7\text{A} - 2.8\text{A} \approx 1.9\text{ A} \\
i_{tot} &= i_{P,rms} + \frac{N_S}{N_P}i_{S,rms} = 0.57\text{A} + \frac{12}{92}4.7\text{A} \approx 1.18\text{ A}
\end{aligned}$$

DCDC29:

$$
\begin{aligned}
i_{P,rms} &= i_{Ppk}\sqrt{\frac{D_{on}}{3}} = 1.49\text{A}\sqrt{\frac{8.51\mu\text{s} * 50\text{kHz}}{3}} = 0.57 \text{ A} \\
t_{off} &= \frac{1}{50\text{kHz}} - 8.51\mu\text{s} - 1.15\mu\text{s} \approx 10.3 \ \mu\text{s} \\
i_{Spk} &= N_{PS}^2\frac{(V_O + v_F)t_{off}}{L} = 7.67^2\frac{(24\text{V} + 1\text{V})10.3\mu\text{s}}{1.35\text{mH}} \approx 11.2 \text{ A} \\
i_{S,rms} &= i_{Spk}\sqrt{\frac{D_{off}}{3}} = 11.2\text{A}\sqrt{\frac{10.3\mu\text{s} * 50\text{kHz}}{3}} \approx 4.6 \text{ A} \\
i_{S1,rms} &= \frac{I_{O1}}{I_{O1} + I_{O2}}i_{S,rms} = \frac{1.8\text{A}}{1.8\text{A} + 1.2\text{A}}4.6\text{A} \approx 2.8 \text{ A} \\
i_{S2,rms} &= i_{S,rms} - i_{S1,rms} = 4.6\text{A} - 2.8\text{A} \approx 1.8 \text{ A} \\
i_{tot} &= i_{P,rms} + \frac{N_S}{N_P}i_{S,rms} = 0.56\text{A} + \frac{12}{92}4.6\text{A} \approx 1.16 \text{ A}
\end{aligned}
$$

ACDC29:

$$
\begin{aligned}
i_{P,rms} &= i_{Ppk}\sqrt{\frac{D_{on}}{3}} = 0.42\text{A}\sqrt{\frac{2.84\mu\text{s} * 100\text{kHz}}{3}} = 0.13 \text{ A} \\
t_{off} &= \frac{1}{100\text{kHz}} - 2.84\mu\text{s} - 1.62\mu\text{s} \approx 5.54 \ \mu\text{s} \\
i_{Spk} &= N_{PS}^2\frac{(V_O + v_F)t_{off}}{L} = 8^2\frac{(24\text{V} + 1\text{V})5.54\mu\text{s}}{2.65\text{mH}} \approx 3.34 \text{ A} \\
i_{S,rms} &= i_{Spk}\sqrt{\frac{D_{off}}{3}} = 3.34\text{A}\sqrt{\frac{5.54\mu\text{s} * 100\text{kHz}}{3}} \approx 1.44 \text{ A} \\
i_{S1,rms} &= \frac{I_{O1}}{I_{O1} + I_{O2}}i_{S,rms} = \frac{0.41\text{A}}{0.41\text{A} + 0.45\text{A}}1.44\text{A} \approx 0.69 \text{ A} \\
i_{S2,rms} &= i_{S,rms} - i_{S1,rms} = 1.44\text{A} - 0.69\text{A} \approx 0.75 \text{ A} \\
i_{tot} &= i_{P,rms} + \frac{N_S}{N_P}i_{S,rms} = 0.13\text{A} + \frac{11}{88}1.44\text{A} \approx 0.31 \text{ A}
\end{aligned}
$$

Cross sectional areas and maximum diameters of winding wires
DCDC34:

$$
\begin{aligned}
\alpha_P &= \frac{N_P i_{P,rms}}{N_P i_{tot}} = \frac{0.57\text{A}}{1.2\text{A}} \approx 0.5 \\
\alpha_{S1} &= \frac{N_S i_{S1,rms}}{N_P i_{tot}} = \frac{12 * 2.8\text{A}}{92 * 1.2\text{A}} \approx 0.3 \\
\alpha_{S2} &= \frac{N_S i_{S2,rms}}{N_P i_{tot}} = \frac{12 * 1.9\text{A}}{92 * 1.2\text{A}} \approx 0.2 \\
A_{wP} &\leq \frac{\alpha_P K_u W_A}{N_P} = \frac{0.5 * 0.33 * 123\text{mm}^2}{92} \approx 0.22 \text{ mm}^2 \\
d_{wP} &\leq 2\sqrt{\frac{A_{wP}}{\pi}} = 2\sqrt{\frac{0.22\text{mm}^2}{\pi}} \approx 0.53 \text{ mm}
\end{aligned}
$$

$$
\begin{aligned}
A_{wS1} &\leq \frac{\alpha_{S1} K_u W_A}{N_S} = \frac{0.3 * 0.33 * 123\text{mm}^2}{12} \approx 1.0 \text{ mm}^2 \\
d_{wS1} &\leq 2\sqrt{\frac{A_{wS1}}{\pi}} = 2\sqrt{\frac{1.0\text{mm}^2}{\pi}} \approx 1.13 \text{ mm} \\
A_{wS2} &\leq \frac{\alpha_{S2} K_u W_A}{N_S} = \frac{0.2 * 0.33 * 123\text{mm}^2}{12} \approx 0.68 \text{ mm}^2 \\
d_{wS2} &\leq 2\sqrt{\frac{A_{wS2}}{\pi}} = 2\sqrt{\frac{0.68\text{mm}^2}{\pi}} \approx 0.93 \text{ mm}
\end{aligned}
$$

DCDC29:

$$
\begin{aligned}
\alpha_P &= \frac{N_P i_{P,rms}}{N_P i_{tot}} = \frac{0.57\text{A}}{1.2\text{A}} \approx 0.48 \\
\alpha_{S1} &= \frac{N_S i_{S1,rms}}{N_P i_{tot}} = \frac{12 * 2.8\text{A}}{92 * 1.2\text{A}} \approx 0.3 \\
\alpha_{S2} &= \frac{N_S i_{S2,rms}}{N_P i_{tot}} = \frac{12 * 1.9\text{A}}{92 * 1.2\text{A}} \approx 0.2 \\
A_{wP} &\leq \frac{\alpha_P K_u W_A}{N_P} = \frac{0.48 * 0.33 * 90\text{mm}^2}{92} \approx 0.15 \text{ mm}^2 \\
d_{wP} &\leq 2\sqrt{\frac{A_{wP}}{\pi}} = 2\sqrt{\frac{0.15\text{mm}^2}{\pi}} \approx 0.44 \text{ mm} \\
A_{wS1} &\leq \frac{\alpha_{S1} K_u W_A}{N_S} = \frac{0.3 * 0.33 * 90\text{mm}^2}{12} \approx 0.74 \text{ mm}^2 \\
d_{wS1} &\leq 2\sqrt{\frac{A_{wS1}}{\pi}} = 2\sqrt{\frac{0.74\text{mm}^2}{\pi}} \approx 0.97 \text{ mm} \\
A_{wS2} &\leq \frac{\alpha_{S2} K_u W_A}{N_S} = \frac{0.2 * 0.33 * 90\text{mm}^2}{12} \approx 0.49 \text{ mm}^2 \\
d_{wS2} &\leq 2\sqrt{\frac{A_{wS2}}{\pi}} = 2\sqrt{\frac{0.49\text{mm}^2}{\pi}} \approx 0.79 \text{ mm}
\end{aligned}
$$

ACDC29:

$$
\begin{aligned}
\alpha_P &= \frac{N_P i_{P,rms}}{N_P i_{tot}} = \frac{0.13\text{A}}{0.31\text{A}} \approx 0.42 \\
\alpha_{S1} &= \frac{N_S i_{S1,rms}}{N_P i_{tot}} = \frac{11 * 0.69\text{A}}{88 * 0.31\text{A}} \approx 0.28 \\
\alpha_{S2} &= \frac{N_S i_{S2,rms}}{N_P i_{tot}} = \frac{11 * 0.75\text{A}}{88 * 0.31\text{A}} \approx 0.30 \\
A_{wP} &\leq \frac{\alpha_P K_u W_A}{N_P} = \frac{0.42 * 0.33 * 90\text{mm}^2}{88} \approx 0.14 \text{ mm}^2 \\
d_{wP} &\leq 2\sqrt{\frac{A_{wP}}{\pi}} = 2\sqrt{\frac{0.14\text{mm}^2}{\pi}} \approx 0.42 \text{ mm} \\
A_{wS1} &\leq \frac{\alpha_{S1} K_u W_A}{N_S} = \frac{0.28 * 0.33 * 90\text{mm}^2}{11} \approx 0.76 \text{ mm}^2
\end{aligned}
$$

$$
\begin{aligned}
d_{wS1} &\leq 2\sqrt{\frac{A_{wS1}}{\pi}} = 2\sqrt{\frac{0.76\text{mm}^2}{\pi}} \approx 0.98 \text{ mm} \\
A_{wS2} &\leq \frac{\alpha_{S2} K_u W_A}{N_S} = \frac{0.3 * 0.33 * 90\text{mm}^2}{11} \approx 0.81 \text{ mm}^2 \\
d_{wS2} &\leq 2\sqrt{\frac{A_{wS2}}{\pi}} = 2\sqrt{\frac{0.81\text{mm}^2}{\pi}} \approx 1.0 \text{ mm}
\end{aligned}
$$

Skin depth and numbers of strands
Skin depth:

$$
\begin{aligned}
\delta &= \sqrt{\frac{\rho_c}{\pi f \mu_0}} = \sqrt{\frac{2.3 * 10^{-8}\Omega\text{m}}{\pi * 160\text{kHz} * 1.26 * 10^{-6}}} \approx 0.19 \text{ mm} \\
d_{wP} &= 2 * \delta = 2 * 0.19\text{mm} = 0.38 \text{ mm}
\end{aligned}
$$

DCDC34$_\text{m}$:

$$
\begin{aligned}
d_{wi,p} &= \frac{d_{wi}}{\sqrt{p}} \\
p &= \frac{d_{wP}^2}{d_{wP,p}^2} = \frac{(0.53\text{mm})^2}{(0.25\text{mm})^2} \approx 4 \\
p &= \frac{d_{wS1}^2}{d_{wS1,p}^2} = \frac{(1.13\text{mm})^2}{(0.3\text{mm})^2} \approx 14 \\
p &= \frac{d_{wS2}^2}{d_{wS2,p}^2} = \frac{(0.93\text{mm})^2}{(0.3\text{mm})^2} \approx 10
\end{aligned}
$$

DCDC29$_\text{m}$:

$$
\begin{aligned}
p &= \frac{d_{wP}^2}{d_{wP,p}^2} = \frac{(0.44\text{mm})^2}{(0.2\text{mm})^2} \approx 5 \\
p &= \frac{d_{wS1}^2}{d_{wS1,p}^2} = \frac{(0.97\text{mm})^2}{(0.28\text{mm})^2} \approx 12 \\
p &= \frac{d_{wS2}^2}{d_{wS2,p}^2} = \frac{(0.79\text{mm})^2}{(0.23\text{mm})^2} \approx 12
\end{aligned}
$$

ACDC29$_\text{m}$:

$$
\begin{aligned}
p &= \frac{d_{wP}^2}{d_{wP,p}^2} = \frac{(0.42\text{mm})^2}{(0.2\text{mm})^2} \approx 4 \\
p &= \frac{d_{wS1}^2}{d_{wS1,p}^2} = \frac{(0.98\text{mm})^2}{(0.28\text{mm})^2} \approx 12 \\
p &= \frac{d_{wS2}^2}{d_{wS2,p}^2} = \frac{(1.0\text{mm})^2}{(0.27\text{mm})^2} \approx 14
\end{aligned}
$$

Ohmic resistances and losses

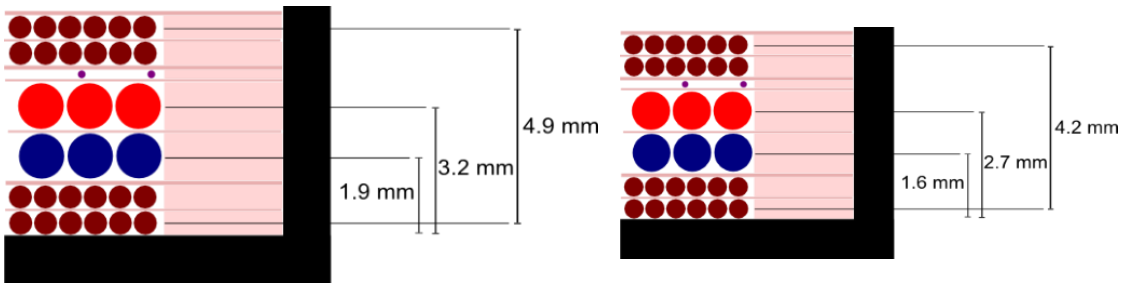

Figure C1: Distances for determining radius r to calculate mean lengths per turn. DCDC34 on the left and DCDC29 on the right.

Distances from Figure C1.
DCDC34:

$$\begin{aligned}
r_P &= \frac{d_c}{2} + \frac{d_{wP,p}}{2} + \frac{4.9\text{mm}}{2} = \frac{13.6\text{mm}}{2} + \frac{0.55}{2} + \frac{4.9\text{mm}}{2} \approx 9.5 \text{ mm} \\
r_{S1} &= \frac{d_c}{2} + 1.9\text{mm} = \frac{13.6\text{mm}}{2} + 1.9\text{mm} \approx 8.7 \text{ mm} \\
r_{S2} &= \frac{d_c}{2} + 3.2\text{mm} = \frac{13.6\text{mm}}{2} + 3.2\text{mm} \approx 10 \text{ mm} \\
MLT_P &= 2\pi r_P = 2 * \pi * 9.5\text{mm} \approx 59.7 \text{ mm} \\
MLT_{S1} &= 2\pi r_{S1} = 2 * \pi * 8.7\text{mm} \approx 54.7 \text{ mm} \\
MLT_{S2} &= 2\pi r_{S2} = 2 * \pi * 10\text{mm} \approx 62.6 \text{ mm}
\end{aligned}$$

DCDC29 and ACDC29:

$$\begin{aligned}
r_P &= \frac{d_c}{2} + \frac{d_{wP,p}}{2} + \frac{4.2\text{mm}}{2} = \frac{12.2\text{mm}}{2} + \frac{0.4}{2} + \frac{4.2\text{mm}}{2} \approx 8.4 \text{ mm} \\
r_{S1} &= \frac{d_c}{2} + 1.6\text{mm} = \frac{12.2\text{mm}}{2} + 1.6\text{mm} \approx 7.7 \text{ mm} \\
r_{S2} &= \frac{d_c}{2} + 2.7\text{mm} = \frac{12.2\text{mm}}{2} + 2.7\text{mm} \approx 8.8 \text{ mm} \\
MLT_P &= 2\pi r_P = 2 * \pi * 8.4\text{mm} \approx 52.8 \text{ mm} \\
MLT_{S1} &= 2\pi r_{S1} = 2 * \pi * 7.7\text{mm} \approx 48.4 \text{ mm} \\
MLT_{S2} &= 2\pi r_{S2} = 2 * \pi * 8.8\text{mm} \approx 55.3 \text{ mm}
\end{aligned}$$

Resistances and losses
DCDC34:

$$\begin{aligned}
R_{0P} &= \rho_c \frac{4MLT_P N_P}{\pi d_{wP,p}^2} = 2.3 * 10^{-8}\Omega\text{m} \frac{4 * 59.7 * 10^{-3}\text{m} * 92}{\pi * (0.55 * 10^{-3}\text{m})^2} \approx 0.53 \ \Omega \\
R_{0S1} &= \rho_c \frac{4MLT_{S1} N_S}{\pi d_{wS1,p}^2} = 2.3 * 10^{-8}\Omega\text{m} \frac{4 * 54.7 * 10^{-3}\text{m} * 12}{\pi * (1 * 10^{-3}\text{m})^2} \approx 0.019 \ \Omega
\end{aligned}$$

$$
\begin{aligned}
R_{0S2} &= \rho_c \frac{4MLT_{S2}N_S}{\pi d_{wS2,p}^2} = 2.3*10^{-8}\Omega\mathrm{m}\frac{4*62.6*10^{-3}\mathrm{m}*12}{\pi*(0.9*10^{-3}\mathrm{m})^2} \approx 0.027\ \Omega \\
J_P &= \frac{i_{P,rms}}{p_P*\pi\frac{d_{wP,p}}{2}^2} = \frac{0.57\mathrm{A}}{\pi\frac{0.055\mathrm{cm}}{2}^2} \approx 240\ \mathrm{A/cm^2} \\
J_{S1} &= \frac{i_{S1,rms}}{p_{S1}*\pi\frac{d_{wS1,p}}{2}^2} = \frac{2.8\mathrm{A}}{\pi\frac{0.1\mathrm{cm}}{2}^2} \approx 357\ \mathrm{A/cm^2} \\
J_{S2} &= \frac{i_{S2,rms}}{p_{S2}*\pi\frac{d_{wS2,p}}{2}^2} = \frac{1.9\mathrm{A}}{\pi\frac{0.09\mathrm{cm}}{2}^2} \approx 299\ \mathrm{A/cm^2} \\
P_{Cu0} &= R_{0P}*i_{P,rms}^2 + R_{0S1}*i_{S1,rms}^2 + R_{0S2}*i_{S2,rms}^2 \\
P_{Cu0} &= 0.53\Omega*(0.57\mathrm{A})^2 + 0.019\Omega*(2.8\mathrm{A})^2 + 0.027\Omega*(1.9\mathrm{A})^2 \approx 0.42\ \mathrm{W}
\end{aligned}
$$

DCDC34$_\mathrm{m}$:

$$
\begin{aligned}
R_{0P} &= \rho_c \frac{4MLT_PN_P}{\pi d_{wP,p}^2} = 2.3*10^{-8}\Omega\mathrm{m}\frac{4*59.7*10^{-3}\mathrm{m}*92}{\pi*(\sqrt{3}*0.25*10^{-3}\mathrm{m})^2} \approx 0.86\ \Omega \\
R_{0S1} &= \rho_c \frac{4MLT_{S1}N_S}{\pi d_{wS1,p}^2} = 2.3*10^{-8}\Omega\mathrm{m}\frac{4*54.7*10^{-3}\mathrm{m}*12}{\pi*(\sqrt{8}*0.30*10^{-3}\mathrm{m})^2} \approx 0.027\ \Omega \\
R_{0S2} &= \rho_c \frac{4MLT_{S2}N_S}{\pi d_{wS2,p}^2} = 2.3*10^{-8}\Omega\mathrm{m}\frac{4*62.6*10^{-3}\mathrm{m}*12}{\pi*(\sqrt{7}*0.3*10^{-3}\mathrm{m})^2} \approx 0.035\ \Omega \\
J_P &= \frac{i_{P,rms}}{p_P*\pi\frac{d_{wP,p}}{2}^2} = \frac{0.57\mathrm{A}}{3*\pi\frac{0.025\mathrm{cm}}{2}^2} \approx 387\ \mathrm{A/cm^2} \\
J_{S1} &= \frac{i_{S1,rms}}{p_{S1}*\pi\frac{d_{wS1,p}}{2}^2} = \frac{2.8\mathrm{A}}{8*\pi\frac{0.03\mathrm{cm}}{2}^2} \approx 495\ \mathrm{A/cm^2} \\
J_{S2} &= \frac{i_{S2,rms}}{p_{S2}*\pi\frac{d_{wS2,p}}{2}^2} = \frac{1.9\mathrm{A}}{7*\pi\frac{0.03\mathrm{cm}}{2}^2} \approx 384\ \mathrm{A/cm^2} \\
P_{Cu0} &= R_{0P}*i_{P,rms}^2 + R_{0S1}*i_{S1,rms}^2 + R_{0S2}*i_{S2,rms}^2 \\
P_{Cu0} &= 0.86\Omega*(0.57\mathrm{A})^2 + 0.027\Omega*(2.8\mathrm{A})^2 + 0.035\Omega*(1.9\mathrm{A})^2 \approx 0.62\ \mathrm{W}
\end{aligned}
$$

DCDC29:

$$
\begin{aligned}
R_{0P} &= \rho_c \frac{4MLT_PN_P}{\pi d_{wP,p}^2} = 2.3*10^{-8}\Omega\mathrm{m}\frac{4*52.8*10^{-3}\mathrm{m}*92}{\pi*(0.4*10^{-3}\mathrm{m})^2} \approx 0.89\ \Omega \\
R_{0S1} &= \rho_c \frac{4MLT_{S1}N_S}{\pi d_{wS1,p}^2} = 2.3*10^{-8}\Omega\mathrm{m}\frac{4*48.4*10^{-3}\mathrm{m}*12}{\pi*(0.9*10^{-3}\mathrm{m})^2} \approx 0.021\ \Omega \\
R_{0S2} &= \rho_c \frac{4MLT_{S2}N_S}{\pi d_{wS2,p}^2} = 2.3*10^{-8}\Omega\mathrm{m}\frac{4*55.3*10^{-3}\mathrm{m}*12}{\pi*(0.7*10^{-3}\mathrm{m})^2} \approx 0.040\ \Omega \\
J_P &= \frac{i_{P,rms}}{p_P*\pi\frac{d_{wP,p}}{2}^2} = \frac{0.57\mathrm{A}}{\pi\frac{0.04\mathrm{cm}}{2}^2} \approx 454\ \mathrm{A/cm^2} \\
J_{S1} &= \frac{i_{S1,rms}}{p_{S1}*\pi\frac{d_{wS1,p}}{2}^2} = \frac{2.8\mathrm{A}}{\pi\frac{0.09\mathrm{cm}}{2}^2} \approx 440\ \mathrm{A/cm^2}
\end{aligned}
$$

$$
\begin{aligned}
J_{S2} &= \frac{i_{S2,rms}}{p_{S2} * \pi \frac{d_{wS2,p}}{2}^2} = \frac{1.8\text{A}}{\pi \frac{0.07\text{cm}}{2}^2} \approx 468 \text{ A/cm}^2 \\
P_{Cu0} &= R_{0P} * i_{P,rms}^2 + R_{0S1} * i_{S1,rms}^2 + R_{0S2} * i_{S2,rms}^2 \\
P_{Cu0} &= 0.89\Omega * (0.57\text{A})^2 + 0.021\Omega * (2.8\text{A})^2 + 0.040\Omega * (1.8\text{A})^2 \approx 0.58 \text{ W}
\end{aligned}
$$

DCDC29$_\text{m}$:

$$
\begin{aligned}
R_{0P} &= \rho_c \frac{4MLT_P N_P}{\pi d_{wP,p}^2} = 2.3 * 10^{-8}\Omega\text{m} \frac{4 * 52.8 * 10^{-3}\text{m} * 92}{\pi * (\sqrt{3} * 0.20 * 10^{-3}\text{m})^2} \approx 1.19 \ \Omega \\
R_{0S1} &= \rho_c \frac{4MLT_{S1} N_S}{\pi d_{wS1,p}^2} = 2.3 * 10^{-8}\Omega\text{m} \frac{4 * 48.4 * 10^{-3}\text{m} * 12}{\pi * (\sqrt{7} * 0.28 * 10^{-3}\text{m})^2} \approx 0.031 \ \Omega \\
R_{0S2} &= \rho_c \frac{4MLT_{S2} N_S}{\pi d_{wS2,p}^2} = 2.3 * 10^{-8}\Omega\text{m} \frac{4 * 55.3 * 10^{-3}\text{m} * 12}{\pi * (\sqrt{7} * 0.23 * 10^{-3}\text{m})^2} \approx 0.052 \ \Omega \\
J_P &= \frac{i_{P,rms}}{p_P * \pi \frac{d_{wP,p}}{2}^2} = \frac{0.57\text{A}}{3 * \pi \frac{0.02\text{cm}}{2}^2} \approx 605 \text{ A/cm}^2 \\
J_{S1} &= \frac{i_{S1,rms}}{p_{S1} * \pi \frac{d_{wS1,p}}{2}^2} = \frac{2.8\text{A}}{7 * \pi \frac{0.028\text{cm}}{2}^2} \approx 650 \text{ A/cm}^2 \\
J_{S2} &= \frac{i_{S2,rms}}{p_{S2} * \pi \frac{d_{wS2,p}}{2}^2} = \frac{1.8\text{A}}{7 * \pi \frac{0.023\text{cm}}{2}^2} \approx 619 \text{ A/cm}^2 \\
P_{Cu0} &= R_{0P} * i_{P,rms}^2 + R_{0S1} * i_{S1,rms}^2 + R_{0S2} * i_{S2,rms}^2 \\
P_{Cu0} &= 1.19\Omega * (0.57\text{A})^2 + 0.031\Omega * (2.8\text{A})^2 + 0.052\Omega * (1.8\text{A})^2 \approx 0.80 \text{ W}
\end{aligned}
$$

ACDC29:

$$
\begin{aligned}
R_{0P} &= \rho_c \frac{4MLT_P N_P}{\pi d_{wP,p}^2} = 2.3 * 10^{-8}\Omega\text{m} \frac{4 * 52.8 * 10^{-3}\text{m} * 88}{\pi * (0.4 * 10^{-3}\text{m})^2} \approx 0.85 \ \Omega \\
R_{0S1} &= \rho_c \frac{4MLT_{S1} N_S}{\pi d_{wS1,p}^2} = 2.3 * 10^{-8}\Omega\text{m} \frac{4 * 48.4 * 10^{-3}\text{m} * 11}{\pi * (0.8 * 10^{-3}\text{m})^2} \approx 0.024 \ \Omega \\
R_{0S2} &= \rho_c \frac{4MLT_{S2} N_S}{\pi d_{wS2,p}^2} = 2.3 * 10^{-8}\Omega\text{m} \frac{4 * 55.3 * 10^{-3}\text{m} * 11}{\pi * (0.9 * 10^{-3}\text{m})^2} \approx 0.022 \ \Omega \\
J_P &= \frac{i_{P,rms}}{p_P * \pi \frac{d_{wP,p}}{2}^2} = \frac{0.13\text{A}}{\pi \frac{0.04\text{cm}}{2}^2} \approx 103 \text{ A/cm}^2 \\
J_{S1} &= \frac{i_{S1,rms}}{p_{S1} * \pi \frac{d_{wS1,p}}{2}^2} = \frac{0.69\text{A}}{\pi \frac{0.08\text{cm}}{2}^2} \approx 137 \text{ A/cm}^2 \\
J_{S2} &= \frac{i_{S2,rms}}{p_{S2} * \pi \frac{d_{wS2,p}}{2}^2} = \frac{0.75\text{A}}{\pi \frac{0.09\text{cm}}{2}^2} \approx 118 \text{ A/cm}^2 \\
P_{Cu0} &= R_{0P} * i_{P,rms}^2 + R_{0S1} * i_{S1,rms}^2 + R_{0S2} * i_{S2,rms}^2 \\
P_{Cu0} &= 0.85\Omega * (0.13\text{A})^2 + 0.024\Omega * (0.69\text{A})^2 + 0.022\Omega * (0.75\text{A})^2 \approx 0.04 \text{ W}
\end{aligned}
$$

ACDC29$_{\mathrm{m}}$:

$$
\begin{aligned}
R_{0P} &= \rho_c \frac{4MLT_P N_P}{\pi d_{wP,p}^2} = 2.3 * 10^{-8}\Omega\mathrm{m} \frac{4 * 52.8 * 10^{-3}\mathrm{m} * 88}{\pi * (\sqrt{3} * 0.20 * 10^{-3}\mathrm{m})^2} \approx 1.13\ \Omega \\
R_{0S1} &= \rho_c \frac{4MLT_{S1} N_S}{\pi d_{wS1,p}^2} = 2.3 * 10^{-8}\Omega\mathrm{m} \frac{4 * 48.4 * 10^{-3}\mathrm{m} * 11}{\pi * (\sqrt{6} * 0.28 * 10^{-3}\mathrm{m})^2} \approx 0.033\ \Omega \\
R_{0S2} &= \rho_c \frac{4MLT_{S2} N_S}{\pi d_{wS2,p}^2} = 2.3 * 10^{-8}\Omega\mathrm{m} \frac{4 * 55.3 * 10^{-3}\mathrm{m} * 11}{\pi * (\sqrt{7} * 0.27 * 10^{-3}\mathrm{m})^2} \approx 0.035\ \Omega \\
J_P &= \frac{i_{P,rms}}{p_P * \pi \frac{d_{wP,p}}{2}^2} = \frac{0.13\mathrm{A}}{3 * \pi \frac{0.02\mathrm{cm}}{2}^2} \approx 138\ \mathrm{A/cm^2} \\
J_{S1} &= \frac{i_{S1,rms}}{p_{S1} * \pi \frac{d_{wS1,p}}{2}^2} = \frac{0.69\mathrm{A}}{6 * \pi \frac{0.028\mathrm{cm}}{2}^2} \approx 187\ \mathrm{A/cm^2} \\
J_{S2} &= \frac{i_{S2,rms}}{p_{S2} * \pi \frac{d_{wS2,p}}{2}^2} = \frac{0.75\mathrm{A}}{7 * \pi \frac{0.027\mathrm{cm}}{2}^2} \approx 187\ \mathrm{A/cm^2} \\
P_{Cu0} &= R_{0P} * i_{P,rms}^2 + R_{0S1} * i_{S1,rms}^2 + R_{0S2} * i_{S2,rms}^2 \\
P_{Cu0} &= 1.13\Omega * (0.13\mathrm{A})^2 + 0.033\Omega * (0.69\mathrm{A})^2 + 0.035\Omega * (0.75\mathrm{A})^2 \approx 0.05\ \mathrm{W}
\end{aligned}
$$

Costs of DCDC34m using TIW in all windings.

$$
\begin{aligned}
Primary &= 0.77\% * 28.7\% * \frac{59.7\mathrm{mm}}{55.3\mathrm{mm}} * 7.67 \approx 183\ \% \\
Secondaries &= 32.4\% + 32.4\% * \frac{54.7\mathrm{mm}}{62.6\mathrm{mm}} \approx 60.7\ \% \\
Labor &= \frac{2}{3} * 19.9\% \approx 13.3\ \% \\
Other &= \frac{9}{10} * 8.2\% \approx 7.4\ \% \\
Complete &= Core + Coilformer + Primary + Secondaries + Labor + \\
&\quad Other \\
Complete &= 19.0\% + 8.2\% + 183\% + 60.7\% + 13.3\% + 7.4\% \approx 292\ \%
\end{aligned}
$$